

**Study of aerosol distribution and associated meteorology
over the central Himalayas**

**A Thesis
Submitted to the University of Delhi
For the award of the Degree of
DOCTOR OF PHILOSOPHY
in
PHYSICS**

By

Raman Solanki

**Department of Physics & Astrophysics
University of Delhi, Delhi- 110 007
and**

**Aryabhata Research Institute of Observational Sciences (ARIES)
Manora Peak, Nainital-263002**

**Under the joint supervision of
Dr. Narendra Singh and Dr S. K. Dhaka**



**DEPARTMENT OF PHYSICS & ASTROPHYSICS
UNIVERSITY OF DELHI
DELHI- 110 007
INDIA**

September, 2016

Study of aerosol distribution and associated meteorology over the central Himalayas

**A Thesis
Submitted to the University of Delhi
For the award of the Degree of
DOCTOR OF PHILOSOPHY
in
PHYSICS**

By

Raman Solanki

Department of Physics & Astrophysics
University of Delhi, Delhi- 110 007
and

Aryabhata Research Institute of Observational Sciences (ARIES)
Manora Peak, Nainital-263002

Under the joint supervision of

Dr. Narendra Singh and Dr S. K. Dhaka



**DEPARTMENT OF PHYSICS & ASTROPHYSICS
UNIVERSITY OF DELHI
DELHI- 110 007
INDIA**

September, 2016

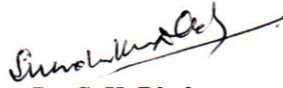
DECLARATION

I Raman Solanki, hereby declare that the thesis entitled “**Study of aerosol distribution and associated meteorology over the central Himalayas**” is an authentic record of the research carried out by me under the joint supervision of Dr. Narendra Singh, ARIES, Nainital and Dr. S. K. Dhaka, Department of Physics and Electronics, Rajdhani College, University of Delhi. This work is original and has not been submitted for the award of any other degree in this university or any other university. The assistance received from various sources during the course of study has been duly acknowledged.



Dr. Narendra Singh
(Supervisor)

निदेशिका - १०
एरीस, रात सीड
नंतीलास.



Dr. S. K. Dhaka
(Supervisor)



Raman Solanki
(Candidate)



Prof. Amitabha Mukherjee
(Head)

Department of Physics & Astrophysics
University of Delhi
Delhi - 110007

प्रो. अमिताभ मुखर्जी / Prof. A. Mukherjee
विभागाध्यक्ष / Head
भौतिकी और खगोलभौतिकी विभाग
Department of Physics & Astrophysics
विश्वविद्यालय, दिल्ली
University of Delhi, Delhi-110007



Department of Physics & Astrophysics

University of Delhi
Delhi-110007, India

Date : 22-09-2016

Certificate of Originality

The research work embodied in this thesis entitled
" study of aerosol distribution and associated meteorology over the
central Himalayas " has been carried out by me at the Department of
Physics &
Astrophysics, University of Delhi, Delhi, India. The manuscript has been
subjected to plagiarism check by Turnitin software. The work
submitted for consideration of award of Ph.D is original.

Raman Solanki
RAMAN SOLANKI

Name and Signature of the Candidate

Student Approval Form

Name of the Author	Raman Solanki
Department	Physics & Astrophysics
Degree	Doctor of Philosophy
University	University of Delhi
Guide	Dr. Narendra Singh and Dr. S.K. Dhaka
Thesis Title	study of aerosol distribution and associated meteorology over the central Himalayas
Year of Award	

Agreement

1. I hereby certify that, if appropriate, I have obtained and attached hereto a written permission/statement from the owner(s) of each third party copyrighted matter to be included in my thesis/dissertation, allowing distribution as specified below.
2. I hereby grant to the university and its agents the non-exclusive license to archive and make accessible, under the conditions specified below, my thesis/dissertation, in whole or in part in all forms of media, now or hereafter known. I retain all other ownership rights to the copyright of the thesis/dissertation. I also retain the right to use in future works (such as articles or books) all or part of this thesis, dissertation, or project report.

Conditions :

1. Release the entire work for access worldwide	
2. Release the entire work for 'My University' only for 1 Year ✓ 2 Year 3 Year and after this time release the work for access worldwide.	
3. Release the entire work for 'My University' only while at the same time releasing the	

<p>following parts of the work (e.g. because other parts relate to publications) for worldwide access.</p> <p>a) Bibliographic details and Synopsis only.</p> <p>b) Bibliographic details, synopsis and the following chapters only.</p> <p>c) Preview/Table of Contents/24 page only.</p>	
<p>4. View Only (No Downloads) (worldwide)</p>	

Ramon Laksh

Signature of the Scholar

Shree Kishore

Signature and seal of the Guide

UNIVERSITY OF DELHI
 Teacher-in-Charge
 Department of Physics & Electronics
 Rajdhani College Raja Garden,
 New Delhi-110015

Place : University of Delhi

Date : 22-09-2016

***Dedicated to the Love of my Parents,
Teachers and Nature***

Acknowledgements

In this journey of last five years, I was accompanied by many individuals who provided advice, guidance, encouragement and friendship, and helped me to overcome all the difficulties and obstacles I came across. I would like to begin this thesis by expressing my sincerest thanks to all these people.

First of all, I would like to acknowledge my supervisor, Dr. Narendra Singh, Scientist ARIES. Should I ever be asked to define the perfect advisor, unhesitatingly I would give his name as definition. While granting all the freedoms I wanted he also continuously provided all the guidance, support and encouragement I needed. I particularly enjoyed all those long and inspiring discussions we had, be it at the institute, be it during pleasant dinners at his home. When frustrations were large he somehow always managed to transform them back into fresh enthusiasm, optimism and motivation. This not only refers to my scientific work, but also to other aspects of life. Thank you for everything!

I am equally indebted to Dr. S. K. Dhaka, my doctoral supervisor at the University of Delhi, for integrating me into his research group. By his immense range of interests and knowledge, he helped me to see research in a wider context. I particularly thank him for providing enthusiasm and direction to my research work. I deeply thank you sir for your support and guidance.

I sincerely thank Director, ARIES for his constant support, encouragement for carrying out my scientific research and establishing the observational facilities.

I am highly grateful to Dr. K Rajeev, Head, IGBP-NOBLE, for his time and sharing his research expertise which provided many helpful ideas. Also, I am grateful to Dr. N. V. P. Kiran Kumar for the discussions on numerous aspects of time-series analysis, especially at the initial stages of my work, our joint efforts to identify systematic measurement errors were crucial to the progress of my research work.

During my scientific visits to Space Physics Laboratory, VSSC, I found two great friends Sagarika and Arun. I am truly thankful to both of them for always believing in me and making research enjoyable.

Being at ARIES was a true delight with the ever changing scenery of the sky from sunrise to sunset, the singing birds and playful monkeys. Some days were truly well directed by nature with intense lightning and thunders, extreme wind speeds, heavy downpours for entire night and few but memorable events of snowfall. This highly rich spectrum of nature in the Himalayas always powered my thoughts in a true sense, making every moment of research memorable. Special thanks to Nibedita for her constant support as a best friend in sharing evening discussions on myriad of thoughts, for regularly taking me on fantastic hikes; I gained plenty of energy from these activities, which also helped me to develop my own understanding of mountain meteorology.

I sincerely acknowledge Late Dr. P Pant for his support and guidance during the initial period of my research work at ARIES. I am thankful to the Academic Committee, all the faculty members and staff of ARIES for their help and support during the course of this work. I am also thankful to Computer section and KRC Library staff of ARIES for their support.

I express my sincere thanks to Director, NARL for development and installation of LAMP at ARIES, Nainital.

I thankfully acknowledge NASA for providing CALIPSO and MISR data; NOAA/ ARL for the HYSPLIT transport and dispersion model.

I am thankful to N. Ojha, A. Pozzer and R. H. H. Jansen from Max Planck Institute for Chemistry, Mainz, Germany for providing the model results and inputs used in the Chapter 5. WRF simulations were performed on the Dresden cluster at the MPI-C. I thank Martin Körfer for his help with computing and data storage.

I am also thankful to the administrative staff of Department of Physics & Astrophysics, and Faculty of Sciences, at the University of Delhi.

All these people are acknowledged, together with Narendra Ojha, Tapaswini Sarangi, Prashant kumar, Ramkesh Yadav, Brajesh Kumar, Akash Priya, Pawan Tiwari and many others, for their support and friendship as well as friendly and harmonic environment I needed. I am also thankful to my school-day friends (Puneet, Tann, Rahul and Naveen) for keeping me in touch with my hometown.

Acknowledgments are made to the ABLN & C project at ARIES, funded under ISRO-GBP. I am also thankful to COSPAR for providing the grant to present and discuss my research work during COSPAR, 2014, Moscow Russia.

My deepest thanks, however, go to my family and teachers for their constant love and support: to my sisters and brother (Rajani, Renuka and Ravish), close family member Mr. Dinesh, my English teacher Mrs. Alini, Mrs. M. B. Sampson, and most importantly to my mummy and papa. They provided encouragement, helpful advice and comfort when I needed it most. It is to them that I dedicate this work.

Raman Solanki

Preface

Air pollution has escalated to a major concern in recent years over the Northern India, particularly due to the drastic increase in anthropogenic emissions as well as the changes in the seasonal cycle of temperature and rains. This change can be better quantified through measurements over a site which is free from local emissions and can thus act as a regional representative. This thesis presents vertical profile measurements of aerosol distribution over a mountain peak in the central Himalayas, taking into account the impact of meteorological conditions on the measurements and also providing the first-cut results on surface layer characteristics and local boundary layer evolution over the site.

The objective of this thesis is based primarily on ground based observation comprising firstly of the boundary layer LiDAR, installed under a joint scientific collaborative program between ARIES, Nainital and NARL, Gadanki. Secondly, observations of surface layer characteristics are made with a pair of sonic anemometers installed under the NOBLE project of ISRO-GBP; thirdly the radar wind profiler measurements of local boundary layer evolution, carried during the GVAX campaign at ARIES forms the last part of this thesis work. The research work for this thesis got initiated through the intermittent LiDAR observations of aerosol vertical profiles. During the spring of 2012, elevated aerosol layers were detected through the LiDAR measurements, these observations were carefully analyzed for the source of these aerosol layers. This case study initiated intensive measurements of aerosol vertical distribution over the site for the entire seasonal cycle, which revealed highly contrasting features in day-to-day and seasonally averaged aerosol vertical profiles, with prominent fluctuations up to 4 km AMSL.

In order to utilize satellite measurements of aerosol vertical distribution over the Himalayas, comparison with ground based measurements is essential. Thus, a detailed and precise comparison ground based LiDAR and CALIPSO satellite measurements was made for the seasonal cycle, estimating the mean percent bias in CALIPSO satellite measurements over the central Himalayas. Through this study on aerosol vertical profile and comparison with satellite retrievals, the spring and winter season were found to have

contrasting features of aerosol distribution especially up to 1 km from ground surface, thus highlighting the need for detailed understanding of the boundary layer dynamics.

For the first time surface layer characteristics are analyzed and presented in this thesis with data obtained from fast-response two-level ultrasonic anemometer measurements. The surface layer fluxes of momentum and sensible heat flux, along with turbulent kinetic energy has been quantified for the spring and winter season. The analysis revealed remarkable features of surface layer characteristics over a mountain ridge, providing insight into the surface layer process and their influence on aerosol distribution over the site.

In order to truly understand the boundary layer evolution over mountainous terrain radar wind profiler (RWP) is an extremely suitable instrument. The limited RWP measurements taken as a part of GVAX campaign provided detailed insight into the local boundary layer evolution over the site during winter season and early spring season. In the spring impact of mountainous topography (under strong synoptic wind conditions) on boundary layer height variations provided intricate details on local boundary layer evolution (LBL) over the site. The LBL height measurements are compared with model simulated boundary layer height, estimating the bias between instrument and model simulations, as well as the implications of these biases in context with trace species model simulations.

List of Publications

1. Narendra Singh, **Raman Solanki**, Narendra Ojha, Ruud H. H. Janssen, Andrea Pozzer, and Surendra K. Dhaka (2016): Boundary layer evolution over the central Himalayas from radio wind profiler and model simulations, *Atmospheric Chemistry and Physics*, 16, 10559-10572, doi:10.5194/acp-16-10559-2016.
2. Narendra Singh, **Raman Solanki**, N. Ojha, M. Naja, U. C. Dumka, D. V. Phanikumar, Ram Sagar, P. Pant, S. K. Satheesh, K. Krishna Moorthy, V. R. Kotamarthi, and S. K. Dhaka (2016): Variations in the cloud-base height over the central Himalayas during Ganges Valley Aerosol experiment: association with the monsoon rainfall. *Current Science*, ISSN: 0011-3891, Vol. 111, No. 1, 10 July 2016, pp 109 – 116.
3. **Raman Solanki**, Narendra Singh, N.V.P. Kiran Kumar, K. Rajeev and S. K. Dhaka (2015): Time variability of surface layer characteristics derived from fast-response micrometeorological observations over a mountain ridge in the central Himalayas during spring season. *Boundary Layer Meteorology*, ISSN: 0006-8314, March 2016, Volume 158, Issue 3, Pages 453-471, Published online: 28 October 2015.
4. **Raman Solanki**, Narendra Singh (2014): LiDAR observations of the vertical distribution of aerosols in free troposphere: Comparison with CALIPSO level-2 data over the central Himalayas. *Atmospheric Environment*, ISSN: 1352-2310, Volume 99, December 2014, Pages 227–238.
5. **Raman Solanki**, Narendra Singh, P Pant, U C Dumka, Y Bhavani Kumar, A K Srivastava, Sanjay Bhist, H C Chandola (2013): Detection of long range transport of aerosols with elevated layers over high altitude station in the central Himalayas: A case study on 22 and 24 March 2012 at ARIES, Nainital. *Indian Journal of Radio and Space Physics*, ISSN: 0367-8393, (Oct. 2013) Vol. 42, Pages 332-339.

6. **Raman Solanki**, Narendra Singh (2012): Study of surface winds and momentum flux using ultrasonic anemometer over Manora Peak, Nainital. *Vayu Mandal Journal*, ISSN: 0970-1397, Vol. 38 No 1-4, Pages 18-25.
-

Manuscripts: under review/ submitted/ to be submitted

1. **Raman Solanki**, Narendra Singh, N.V.P. Kiran Kumar, K. Rajeev and S. K. Dhaka. Impact of mountainous topography on surface layer parameters during weak mean flow conditions. **Boundary layer meteorology**, under review, 2016.
 2. **Raman Solanki**, K. Rajeev, Narendra Singh, S. K. Dhaka and N. V. P. Kiran Kumar. Wind gust and turbulence characteristics over a mountain ridge during spring season. To be submitted to **Journal of Geophysical Research**.
-

Conferences and Symposium

- 1) **Raman Solanki**, Narendra Singh, N. V. P. Kiran Kumar, K. Rajeev and S. K. Dhaka. Impact of mountainous topography on surface layer parameters during weak mean flow conditions. **National Space Science Symposium -2016**, SPL, Trivandrum, (Abstract ID: 893), **ORAL presentation**.
- 2) **Raman Solanki**, K. Rajeev, Narendra Singh, S. K. Dhaka and N. V. P. Kiran Kumar. Wind gust and turbulence characteristics over a mountain ridge during spring season. **National Space Science Symposium -2016**, SPL, Trivandrum, (PS1B-018), **POSTER presentation**.
- 3) Narendra Singh, **Raman Solanki**, K. Rajeev, S. K. Dhaka and N. V. P. Kiran Kumar. Experimental evidence for the applicability of Monin-Obukhov similarity relationships over complex terrain. **National Space Science Symposium -2016**, SPL, Trivandrum, (PS1B-019), **POSTER presentation**.

- 4) **Raman Solanki**, Narendra Singh, Surendra Kumar Dhaka and Narendra Ojha. An integrated study on association between aerosol vertical distribution and boundary layer dynamics over the central Himalayas in conjunction with numerical modeling. **Joint Assembly**, 3-7 May 2015, Montreal, Canada. **POSTER presentation.**
- 5) Narendra Singh, **Raman Solanki** and S. K. Dhaka. Weather front observations over a high altitude station on the boundary of tropics, **National Seminar on ‘New Horizons in Theoretical and Experimental Physics**, Govt. PG College, Gopeshwar, Chamoli, India, Feb 19-20, 2015.
- 6) Narendra Singh, **Raman Solanki**, and H. Nandan. Atmospheric observations over a high altitude station in the central Himalayan region, **Bharatiya Vigyan Sammelan-2015**, Goa, India, Feb, 05-08, 2015. **POSTER presentation.**
- 7) **Raman Solanki**. Micrometeorological observations at ARIES, Nainital. **International conference on Remote Sensing of Earth’s Atmosphere**. University of Delhi, Delhi. 5 September 2014. **Invited talk.**
- 8) **Raman Solanki**, Narendra Singh, N.V.P. Kiran Kumar, K. Rajeev and S. K. Dhaka. Surface layer characteristics derived from fast-response micrometeorological observations over a mountain peak in the central Himalayas. **COSPAR-2014**, 2-10 August 2014, Moscow, Russia. **Oral presentation.**
- 9) Narendra Singh, **Raman Solanki** and S. K. Dhaka. Estimation of turbulence and dispersion parameters over mountainous terrain with sonic anemometer measurements at two levels. **COSPAR-2014**, 2-10 August 2014, Moscow, Russia. **Oral presentation.**
- 10) **Raman Solanki**. Study of Aerosol Vertical Distribution Over the Central Himalayas with LIDAR Observations. **National Workshop on Recent Trends in Atmospheric and Environmental Sciences**. 4-5 April 2014. Gurukula Kangri Vishwavidyalya, Haridwar. **Invited Talk.**
- 11) Narendra Singh, **Raman Solanki**, N.V.P. Kirankumar and K. Rajeev, “Assessment of Surface layer micrometeorological parameters over the complex terrain in the Central Himalayas”, Proceedings of the ARFI, ICARB, RAWEX and **NOBLE project review meeting**, 8-9 January 2014, 263-265.

- 12) **Raman Solanki** and Narendra Singh. Nocturnal observations of aerosol backscatter profiles using LiDAR over the central Himalayas and validation of CALIPSO data. **International workshop on Changing Chemistry in Changing Climate: Monsoon** 1-3 May, 2013, **POSTER presentation.**
 - 13) **Raman Solanki** and Narendra Singh. Study of surface winds and momentum flux using ultrasonic anemometer, over Manora Peak, Nainital. **TROPMET-2012, ORAL presentation.**
 - 14) **Raman Solanki**, P. Pant, U.C. Dumka, H. Joshi, Variation of aerosol properties over Nainital: A high altitude station in central Himalayas. **National Space Science Symposium -2012**, S V University, Tirupati, (PS2:119), **POSTER presentation.**
-

School and seminar

1. **School on radar probing of the Atmosphere**, 08 - 22 November 2011. ARIES, Nainital, India.
 2. Course work on **Atmospheric Boundary Layer Dynamics**, 15-23 October 2012. SPL, VSSC, Trivandrum, India.
 3. National Seminar on **Earth's Atmospheric processes and their link with Climate Change**, 8 July 2013. Rajdhani College, University of Delhi, Delhi, India.
-

List of symbols

T_s	Acoustic temperature
β	Backscatter coefficient
u_*	Friction velocity
g	Acceleration due to gravity
τ	Momentum flux
L	Obukhov length
z_i	Mixed layer depth
H	Sensible heat flux
$S\downarrow$	Shortwave flux
z/L	Stability parameter
e	Turbulent kinetic energy
T_v	Virtual temperature
θ_v	Virtual potential temperature
k	von Karman constant

List of acronyms and abbreviations

ABL	Atmospheric boundary layer
AGL	Above ground level
AMSL	Above mean sea level
AOD	Aerosol optical depth
AWS	Automatic weather station
CAD	Cloud-aerosol discrimination algorithm
CALIPSO	Aerosol Lidar and Infrared Pathfinder Satellite Observations
GBP	Geosphere Biosphere Program
GVAX	Ganges Valley Aerosol Experiment
HYSPLIT	Hybrid Single Particle Integrated Trajectory Model
IGP	Indo-Gangetic Plain
IPCC	Intergovernmental Panel on Climate Change
IMD	Indian Meteorological Department
ISRO	Indian Space Research Organization
LAMP	LiDAR for atmospheric measurements and probing
LR	LiDAR ratio
LBL	Local boundary layer
LiDAR	Light detection and ranging
MXL/MESSy	Mixed Layer model
ML	Mixed layer
MODIS	Moderate-resolution Imaging Spectroradiometer

MOST	Monin-Obukhov similarity theory
MPIC	Max Planck Institute for Chemistry
NBL	Nocturnal boundary layer
NCEP	National centre for environmental prediction
NOAA	National Oceanic and Atmospheric Administration
PBL	Planetary boundary layer
PFM	Planar fit method
RH	Relative humidity
RWP	Radar wind profiler
SPF	Sector-wise planar fit
SNR	Signal to noise ratio
WRF	Weather Research and Forecast

Table of Contents

Declaration	i
Dedication	iii
Acknowledgement	v
Preface	ix
List of publications	xi
List of symbols	xv
List of acronyms	xvii

Chapter 1 Introduction 1-20

1.1 The atmosphere and its constituents	1
1.2 Air pollution and its distribution	4
1.3 Mountain meteorology	7
1.4 Micrometeorology	9
1.4(a) Atmospheric boundary layer	10
1.4(b) The surface layer	13
1.5 Association between air pollution and meteorology	14
1.6 Objective and outline of the thesis	18

Chapter 2 Observational site, Instrumentation and methodology 21-54

2.1 Strategic location of the site	21
2.2 LiDAR	26
2.2(a) LAMP	27
2.2(b) LiDAR ratio approximation	31

2.3 Ultrasonic anemometer	33
2.3(a) Planar fit method	37
2.3(b) Eddy covariance technique	42
2.4 Radar wind profiler	46
2.4(a) Mixed layer determination technique	48
Chapter 3	Variations in aerosol distribution 55-80
3.1 Aerosol vertical distribution	56
3.1 (a) Inter- day variability	56
3.1 (b) Back air trajectory analysis	58
3.1 (c) Seasonal variations	61
3.2 Comparison of LiDAR measurements with CALIPSO satellite retrievals.....	65
3.2 (a) CALIPSO data processing	65
3.2 (b) CALIPSO versus LiDAR	68
3.3 Elevated aerosol layer: A case study	71
3.4 Summary and conclusions	79
Chapter 4	Surface layer characteristics over a mountain ridge in different synoptic conditions 81-108
4.1 Background meteorological conditions during spring and winter season.....	82
4.2 Diurnal cycle of meteorological parameters	84
4.2 (a) Shortwave flux.....	84
4.2 (b) Wind speed, wind direction and wind shear	85
4.2 (b) Mixing ratio	89
4.3 Applicability of Monin-Obukhov similarity theory	92
4.4 Time variability of surface layer fluxes	98
4.4 (a) Sensible heat flux	98

4.4 (b) Momentum flux and turbulent kinetic energy	99
4.5 Time variability in vertical winds	101
4.6 Stability parameter	103
4.7 Impact of wind speed on surface layer fluxes	104
4.8 Summary and conclusions	105
Chapter 5 Local boundary layer evolution and model validation	109-132
5.1 Mixing layer height variations over the site	110
5.1 (a) Comparison between simultaneous measurements	110
5.2 (b) Diurnal variations	114
5.3 (c) Impact of mountainous topography	115
5.2 Model simulations	117
5.2 (a) Weather Research and Forecasting (WRF) model	117
5.2 (b) MiXed Layer model (MXL/MESSy)	119
5.3 Comparison with model simulations	119
5.4 Effects of boundary layer height overestimation on air quality simulations	124
5.5 Summary and conclusions	130
Chapter 6 Conclusions and future scope	133-142
6.1 Aerosol distribution	133
6.2 Surface layer characteristics	135
6.3 Local boundary layer evolution	138
6.4 Achievements and Future scope	139
References	143-164

Blank page

Chapter # 1

Introduction

This chapter deals with the necessity to study vertical distribution of air pollutants and the role of meteorology in transporting and mixing them up into the atmosphere; along with the emphasis on the role of the mountain meteorology and micrometeorology. Air pollution is intrinsically linked with meteorology and this linkage further strengthens over complex mountainous terrain; an attempt towards understanding this association is being made through vertical profile measurements of aerosol and surface layer measurements of wind components, temperature and humidity. This introductory chapter provides an overview of the fundamental concepts of Earth's atmosphere, atmospheric pollution and meteorology in context of this thesis.

1.1 The Earth's atmosphere and its constituents

The atmosphere as we call it is the envelope of gases around the Earth confined through the force of gravity, providing the breaths of life for every living organism on the planet. About 75 % of the mass of atmosphere is confined within first 11 km above mean sea level and when this height is compared with the radius of the Earth (6371 km), it becomes clear how thin this layer of the atmosphere actually is; thus being prone to the changes in composition through human activities across the globe. These changes in air composition have largest amplitudes within first few kilometers from surface of the Earth, implying a consistent need of detailed understanding of the processes taking place close to the ground surface, and thus improving the quality of weather forecasts.

The primary gases in Earth's atmosphere are Nitrogen and Oxygen making up for 99 % of the total volume of dry air, the remaining 1 % comprising of Argon, Neon, Helium, Hydrogen and Xenon, all of these gases are also called permanent gases as their composition remains approximately constant. The global concern is however towards the trace constituents (gases or particles) in the atmosphere, due to their ever changing concentrations and effect on the atmospheric processes. One of the most variable gases is water vapor (variations of 0 to 4 %); in order of abundance the other gases or particles in atmosphere are Carbon dioxide, Methane, Nitrous oxide, Ozone, Particulate matter and Chlorofluorocarbons.

Particulate matter is added to the atmosphere in variable concentrations from a variety of natural sources and human activity (anthropogenic) across the planet. Dust storm, forest fires, sea salt from oceans, biological (pollen, spores, bacteria, etc) and volcanic eruptions are the natural sources of particulate matter. The anthropogenic sources comprise of 20 % (by mass) of the global input of particles into the atmosphere [Wallace and Hobbs, 1977], with main contributions from road dust, wind erosion from tilled land, biomass burning, fuel combustion and industrial processes. The particulate matter affects atmospheric processes through scattering and absorption of radiation (direct effect), acting as cloud condensation nuclei (indirect effect) and also play important role in tropospheric chemistry; therefore, understanding of aerosol distribution is an essential part of understanding the atmosphere.

Radiative forcing (RF) estimates of change in energy flux calculated at the tropopause or at the top of the atmosphere for varying concentration of individual trace constituents is a quantitative method of calculating their impact on the atmosphere [IPCC, 2013]. The estimated RF for various trace gases and aerosol as quantified in the *IPCC, 2013 summary for policy makers* are presented in Figure 1.1.

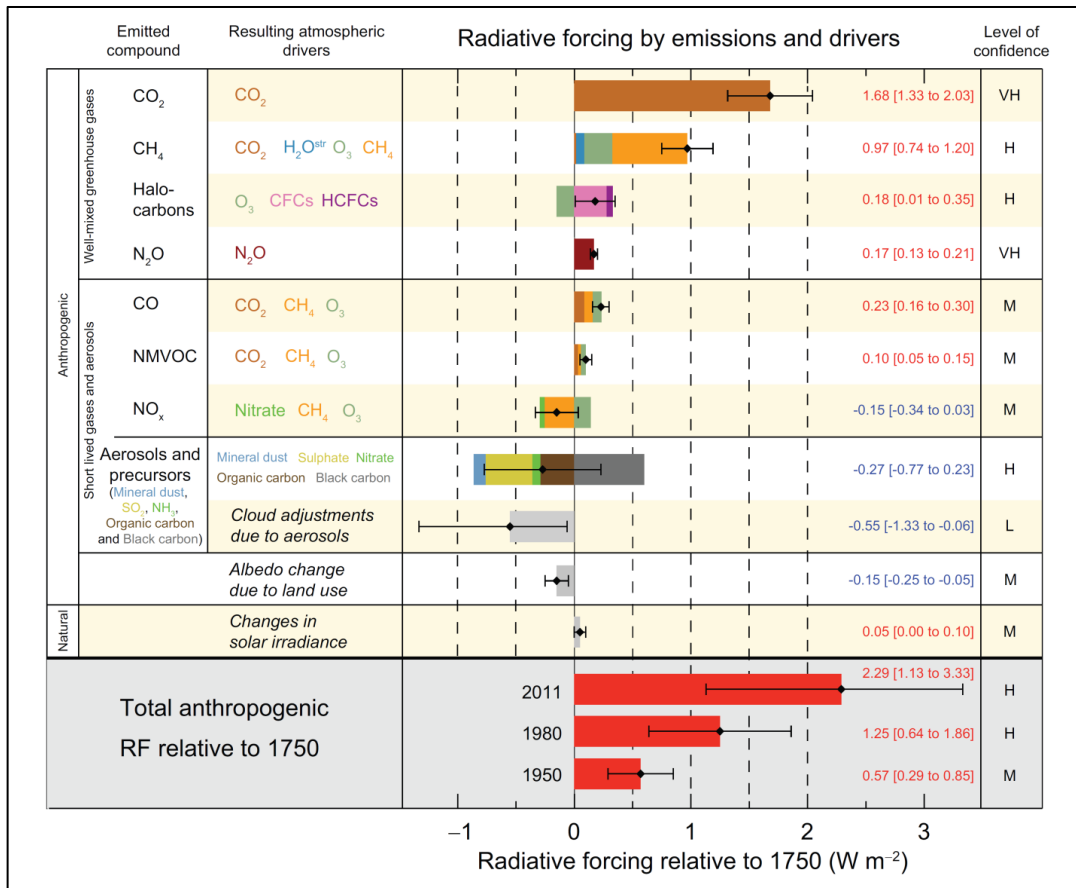


Figure 1.1: Radiative forcing (RF) estimates in 2011 relative to 1750 and aggregated uncertainties for the main drivers of climate change. Values are global average RF partitioned according to the emitted compounds or processes that result in a combination of drivers. The best estimates of the net RF are shown as black diamonds with corresponding uncertainty intervals; the numerical values are provided on the right of the figure, together with the confidence level in the net forcing (VH: very high, H: high, M: medium, L: low, VL: very low). Total anthropogenic RF is provided for three different years relative to 1750. Total anthropogenic radiative forcing is provided for three different years relative to 1750. Adapted from *IPCC, 2013: Summary for Policymakers*.

The two major points to be noted from Figure 1.1 are as follows: firstly, the greenhouse gases hold maximum contribution in terms of warming, whereas aerosols (particularly Sulphate) indicate highest contribution in cooling of atmosphere through aerosol radiation interaction (direct effect). Secondly, the direct and indirect effect of aerosol radiative forcing still remains a significant uncertainty (more than

0.50 W m⁻²) for climate studies due to the large heterogeneity in aerosol properties and inadequate data information particularly in the vertical distribution, thus highlighting the need for intensive studies on aerosol dynamics and their interaction with the atmosphere. The individual contributions to aerosol direct effect of -0.27 W m⁻² on radiation budget (Figure 1.1) are as follows nitrate (-0.07); Sulphate (-0.41) Black carbon (aerosol radiation interaction $+0.60$, snow ice $+0.04$); organic carbon (-0.29); mineral dust (-0.1). It is noteworthy to mention from these numbers, that cooling of the planet through sulfate aerosols (emitted as a result coal burning) is anticipated as counteracting the warming (in part) caused by increased greenhouse gases for the 20th century.

In the next section details on the air pollution and its distribution (with emphasis on vertical distribution) are provided particularly in context with the central Himalayas.

1.2 Air pollution and its distribution

Air pollution is defined as the addition of harmful and toxic substances to the atmosphere which have the potential of causing harm to human life and vegetation. Air pollutants get added to the atmosphere from both natural and human activities, however, due to intense human activities major cities (in developing countries) emerge as prime centers of severely degraded air quality. Currently ground level ozone and particulate matter (aerosol) pose the greatest air quality threats across major urban locations on the globe. In this thesis we will focus on a subset of air pollutants termed as aerosol, however physical transport and mixing processes are the same as for other air pollutants [*De Wekker and Kossmann, 2015*].

Aerosol is the suspension system in gaseous medium consisting of small particles (0.01 to 100 μm) in solid or liquid state, having negligible terminal fall speed. Particulate matter pollution is most noticeable of all pollutants, since one of the direct impacts of higher aerosol loading is visibility reduction as shown in the Figure 1.2; these pictures has been taken from ARIES, Manora peak, providing a

distinguished comparison of clear and hazy conditions during morning and evening hours. One particular point to be noticed from Figure 1.2 is the visible haze layer which is generally confined in vertical below a particular altitude; it is this altitude and its association with weather conditions which play major role in transportation and penetration of haze (air pollution) deeper into the mountain valleys, otherwise being confined to the adjoining plains only. Along with the effects on atmosphere, particulate matter pollution is also known to have adverse effects on human health, such as respiratory problems and heart disease, high levels of particulate matter in megacities are major health issue for people with chronic lungs diseases.

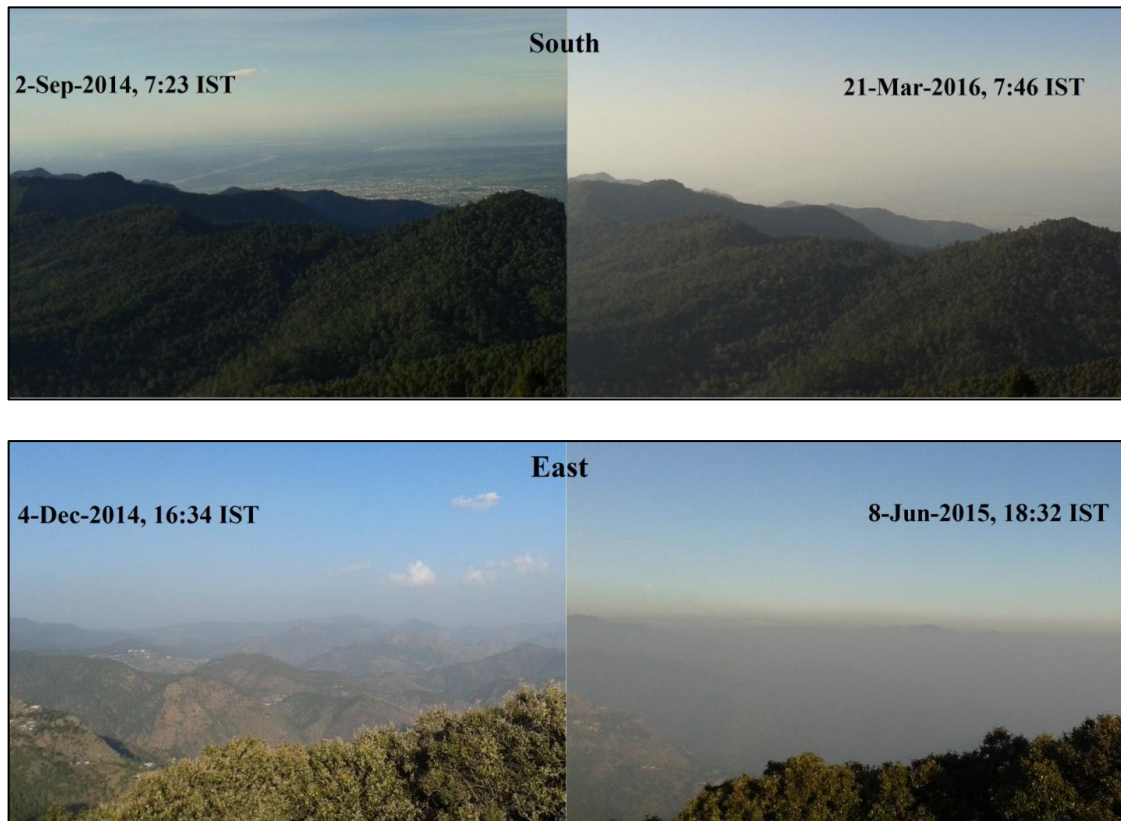


Figure 1.2: Images of visibility reduction taken from Manora Peak, during morning and evening time. The images have been taken for equal zenith angle of sun on clear and hazy days along the south and east direction of ARIES.

Aerosols play a vital role in the Earth atmosphere radiation budget directly by scattering and absorbing the incoming solar radiation; and indirectly by modifying the cloud radiative properties through altering the microphysical properties of clouds; thus adding up to climate change on global scales. The magnitude and sign of aerosol radiative impact depends on physical, chemical as well as radiative properties of the aerosols. Due to the short residence time of aerosols in atmosphere (from few days to a week), washout by rains, diversity in aerosol types and sources; the direct and indirect affect of aerosols exhibit large spatio-temporal variations and their cooling effect does not accumulate like that of greenhouse gases, being controlled only by their present emissions.

In order to assess the radiative forcing of aerosols, the knowledge of vertical distribution of aerosols in the Earth's atmosphere is very important. The measurements of vertical distribution of aerosol are critical to assess the radiative impact of aerosol on the surface and atmosphere [Liu *et al.*, 2012; Kaufman *et al.*, 1997; Pelon *et al.*, 2008]. In addition, aerosols influence the lifetime and microphysical properties of clouds, precipitation rates, and tropospheric photochemistry [Towmey, 1977; IPCC 2001]. Due to the presence of distinct aerosol layers, the columnar properties can be entirely different from the surface properties of aerosol [Ramanathan *et al.*, 2001b]. Considering such an importance, numerous efforts were made from ground based and space borne observations to study aerosol distribution and properties, along with model simulations around the globe, but such studies are very limited over the Indian region particularly those having the information on the vertical distribution of aerosol. Over the Indian regions, satellite based observations have demonstrated very high pollution loadings in terms of aerosol optical depth (AOD), particularly over the Indo-Gangetic Plain (IGP) region. Although integrated columnar properties of aerosols over the central Himalayas have been studied extensively [Sagar *et al.*, 2004; Guleria *et al.*, 2012] but a very limited study on vertical profile exists over Himalayan region [Ramana *et al.*, 2004; Hegde *et al.*, 2009; Srivastava *et al.*, 2011a]. Moreover, our site being located at the

foothills of the Himalayas is vulnerable to the transport of pollutants from nearby IGP. The study of aerosol vertical distribution is essential in many aspects such as radiative transfer calculations, vertical mixing in the lower troposphere in order to understand aerosol variability and aerosol-cloud interaction. Two recent studies on vertical distribution of aerosol have been reported in the adjoining IGP region by *Komppula et al.* [2012] and *Misra et al.* [2012], but results of these studies cannot be implemented over complex terrains such as the Himalayas.

The mountainous terrain exerts its impact on the atmosphere above in an entirely different way as compared to interaction of atmosphere with the underlying ground surface over flat terrain; this difference demands a distinct approach towards understanding of atmospheric processes and pollution dispersion over complex topography. The subsequent section elaborates on the interaction between atmosphere and mountainous terrain.

1.3 Mountain meteorology

Mountains present a wide range of atmospheric phenomena, spectacular views of valleys, ridges and peaks, along with the ever changing patterns of clouds in the sky, especially during sunrise and sunset. The variations in temperature, wind speed and direction, along with the variations in rainfall pattern on a rainy day are always felt extensively while travelling in mountains and also during the course of a day. It is thus evident that understanding of kaleidoscopic mountain weather demands a different approach to meteorology to be specifically termed as mountain meteorology. With a coverage of almost 50 % of Earth's land surface by hilly and mountainous terrain [*Meybeck et al.*, 2001] the importance of in-depth understanding already established interaction between Earth's atmosphere and mountains is highly relevant.

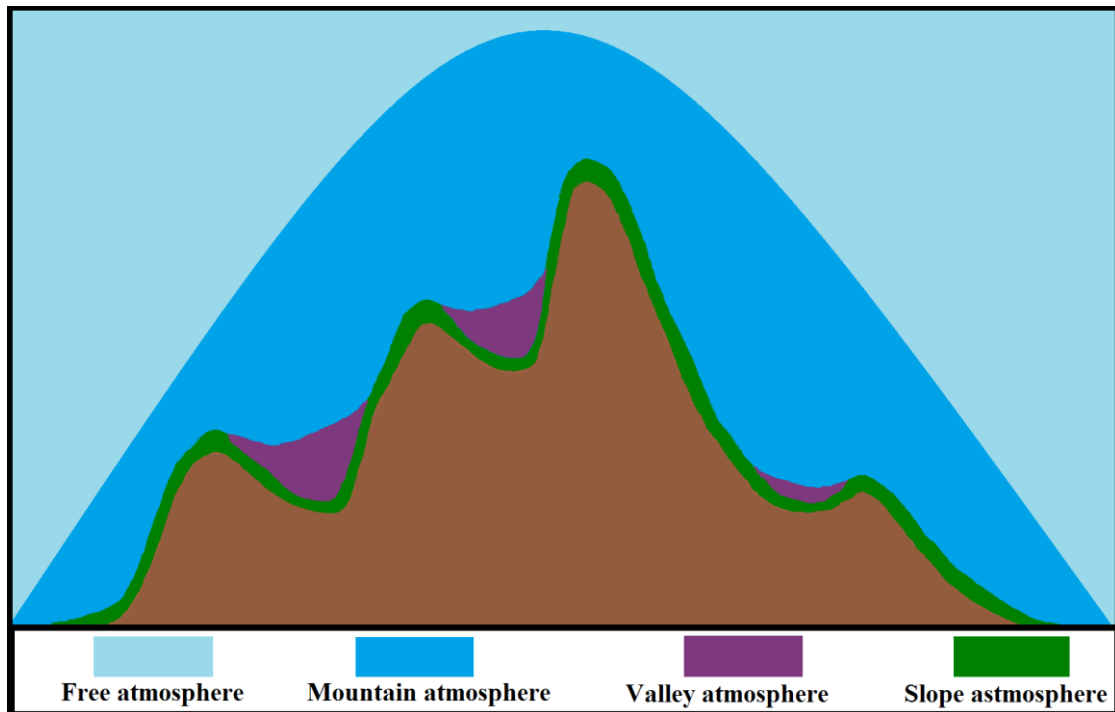


Figure 1.3: Structure of the atmosphere over mountains (adapted from Ekhat, 1948).

The structure of atmosphere over mountainous terrain is much more complicated, as depicted in Figure 1.3, comprising of four different categories. The slope atmosphere, which is a thin layer (at the most 100 m in depth) following the topographical variations; the valley atmosphere, forming in depressions guarded by mountain slopes and extending up to the peak of lowermost ridge, mountain atmosphere is the region influenced by the thermal and dynamical effects of the entire mountain range and the free atmosphere, which remains largely unaffected by diurnal variations in mountain atmosphere.

The key to understand all types of mountain weather [Whiteman, 2000] is the wind systems which develop in mountains. There are four main types of mountain wind systems: (i) slope winds, (ii) along valley winds, (iii) cross valley winds, and (iv) mountain plain winds. Diurnal temperature variations on inclined surfaces produce lateral density gradients that drive the slope winds (katabatic and anabatic winds) along with the drainage circulation, development of which strongly depends

upon the topography, surface type, background winds, and the characteristics of boundary-layer turbulence [Barr and Orgill, 1989; Li and Atkinson, 1999; Papadopoulos and Helmis, 1999; Hughes et al., 2007]. Higher air temperature over steeper slopes results in stronger drainage flows and greater downward mixing of heat towards the surface [Mahrt and Heald, 1983]. In general, the downslope flows persist only for less than an hour after sunrise. Strong regional circulation (either as part of synoptic or mesoscale circulation) might hamper this normal development of local slope circulation and strong nocturnal surface inversion [Whiteman et al., 2000; Stewart et al., 2002]. However, over mountainous terrain, the above mentioned local circulations may be more dominant near the surface, while the effect of regional circulation may be significant at higher levels [Mahrt et al., 2001].

Variations in pollutant concentrations are highly variable in first couple of kilometers from the ground surface, with interaction between ground surface and atmosphere resulting in strongest variations in meteorological parameters. The next section describes the characteristics the process controlling the atmosphere close to the ground surface.

1.4 Micrometeorology

The atmospheric scales of motion are mainly characterized as micro, meso and macro; thus covering a wide range from millimeter to few thousand kilometers in spatial dimensions and from fraction of second to months or year on the temporal scale. In this wide spectrum of scales, the study of micro scale processes is termed as micrometeorology, primarily dealing with the exchange of heat, momentum and mass between the atmosphere and the earth's surface. Although, in general being confined with processes close to the earth's surface, importance of micrometeorological studies are immense, since almost entire human activities are confined near surface of the earth. To name a few of the many, important applications of micrometeorology are air-pollution meteorology, agricultural and forest meteorology, etc. The turbulent motions (an integral part of

micrometeorology) are sub-synoptic phenomena for larger-scale numerical forecast models; adequate turbulence parameterization schemes are essential for making quality weather forecasts beyond few days [Stull, 1988]. Undergoing largest diurnal variations in meteorological parameters and having distinct characteristics, this near surface region of the atmosphere is known as atmospheric boundary layer.

1.4(a) Atmospheric boundary layer

The Atmospheric boundary layer (ABL) is the lowermost part of the atmosphere interacting directly with the Earth's surface, thereby getting modulated on a time scales of few hours or less [Stull, 1988]. The mean thickness of this layer normally varies from 1 to 2 km, however it can be as thick as 4 km or more over hot arid regions, and as thin as few tens of meters over cold snow covered terrain. It is in this layer that most of the air pollutants are confined thereby controlling their concentration through the diurnal variations in ABL height. To emphasize the importance of ABL it is worth mentioning that this layer is the source of nearly all the energy water vapor and trace chemical species that are transported higher up in the atmosphere, thus making it's the most intensely studied part of the atmosphere [Kovalev and Eichenger, 2004].

The vertical structure of the ABL (with thickness Z_i) consists of three different layers is illustrated in Figure 1.4. The first layer is the surface layer starting from ground to $0.1(Z_i)$, the second layer is the convective mixed layer (ML) extending from $0.1Z_i$ to $0.8Z_i$, the ML gets transformed into residual layer (RL) after sunset with the lowermost portion transforming into stable boundary layer (SBL) as a result of interaction between RL and ground surface, one of the features of SBL is horizontal stratification forming bands of different wind speed, temperature and pollutant concentration. The topmost layer is the entrainment zone (or capping inversion during nighttime) from $0.8(Z_i)$ to $1.2(Z_i)$, above the ABL is the free atmosphere since the air flow here is not affected by earth's surface directly.

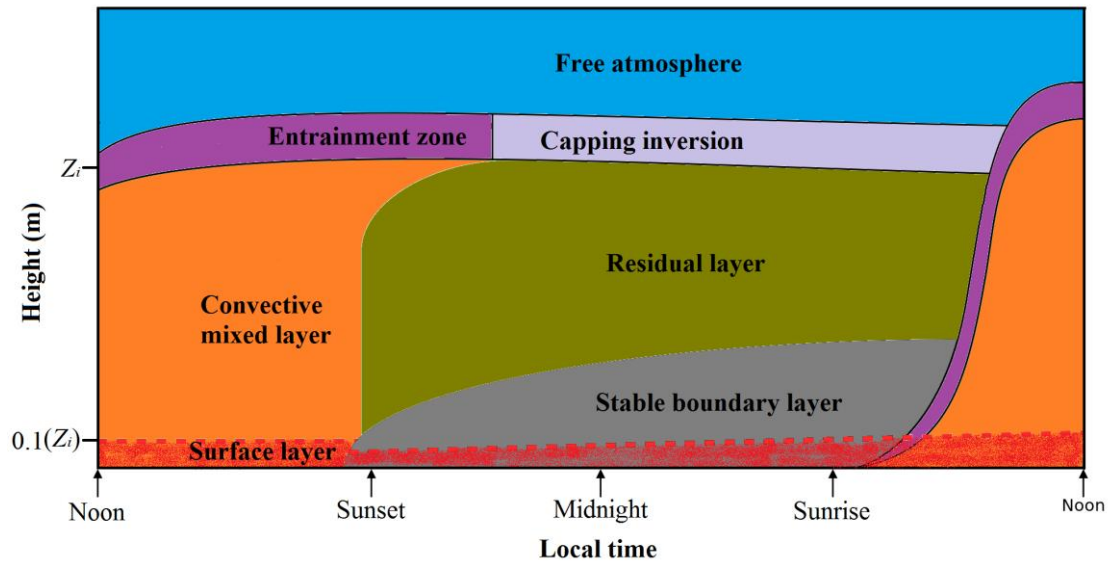


Figure 1.4: Diurnal evolution of atmospheric boundary layer and its vertical structure over flat and homogeneous terrain. Adapted from Stull, 1988.

Over homogeneous flat surfaces, diurnal evolution of Atmospheric Boundary Layer (ABL) is primarily controlled by the variations in net radiation balance, energy fluxes, surface characteristics (including vegetation and soil moisture), and the background meteorological conditions [Stull, 1988]. In contrast, the diurnal evolution of ABL meteorological parameters, energy and momentum fluxes and circulation over mountainous region are further substantially modulated by topography and the associated land cover heterogeneities [Whiteman, 1990; Moraes et al., 2005; Vickers and Mahrt, 2006b; Rotach and Zardi, 2007; Bianco et al., 2011]. Strength of the large-scale prevailing wind and its orientation with the orography as well as the sheltering effects produced by the mountain and trees further add to the complexities in evolution of ABL over mountainous terrain [e.g., Mahrt, 2006; Helgason and Pomeroy, 2012].

Measurements on the diurnal evolution of the planetary boundary layer (PBL), the marine boundary layer (MBL), and in particular over high-altitude complex terrains the local boundary layer (LBL), are essential to understand the

vertical transfer of momentum, energy and the mixing of pollutants in the lower troposphere. The depth or height of the PBL is a fundamental parameter in numerical simulations of regional meteorology and air quality. The height of the mixed layer (ML) is a measure of the effectiveness of the energy transfer from the sun to the earth's surface and thereby to the lower atmosphere and is therefore important for understanding various atmospheric processes [Stull, 1989; Garratt, 1993]. Despite being simple to understand conceptually, the measurement of ML height is rather difficult [Coulter and Holdridge, 1998]. The most traditional method is the analysis of potential temperature and specific humidity profiles, which are obtained from radiosonde ascents [Hooper and Eloranta, 1986]. However, in the past three decades several remote sensing devices such as the Light Detection and Ranging (LiDAR), Sound Detection and Ranging (SoDAR), Radio Acoustic Sounding System (RASS), GPS occultation measurements [Basha and Ratnam, 2009; Xie *et al.*, 2012] and Radio Wind Profilers (RWP) have become indispensable tools to probe the atmospheric boundary layer and the troposphere within first few kilometers above the ground. A review and detailed studies carried out earlier on PBL evolution over various locations are given elsewhere [Friehe, 1987; Garratt and Taylor, 1996].

It is essential to mention that most of the studies cited here and the references therein, are confined to mid and high-latitude regions, and that very few efforts have been made to characterize the PBL evolution over the Indian subcontinent and the complex terrain of the Himalayan region. The available studies using satellite and ground-based measurements over the Indian region have shown influences of the boundary layer evolution and associated mixing on the trapping, dispersion, and transport of pollutants upwards to the pristine high-altitude locations. Some of these studies are connoted subsequently.

The variations in boundary layer height are suggested to influence the dispersion of air pollutants near the earth surface [Guatam *et al.*, 2007]. Deeper boundary layers could also mix residual layer air with higher ozone

concentrations with the air mass near the surface [Reddy *et al.*, 2012]. The investigation of local boundary layer evolution and associated mixing is additionally important over the pristine Himalayas located just north to the densely populated and polluted IGP in order to understand the role of regional pollution on the air quality above Himalayas [Sarangi *et al.*, 2014]. In previous studies, the convective mixing of photochemical pollution [Ojha *et al.*, 2012] and the potential influence of distantly transported and IGP aerosol emissions, on air quality in the central Himalayas has been demonstrated [Solanki *et al.*, 2013; Solanki and Singh, 2014] with the measurements over the region. Continuous measurements of LBL evolution and mixing have not been available until a recent intensive field campaign “Ganges Valley Aerosol Experiment (GVAX)” [Kotamarthi, 2010; Kotamarthi and Satheesh, 2011; Manohanam *et al.*, 2014]. However, systematic and high resolution measurements of the PBL evolution over the IGP region and the LBL evolution over the Himalayan region for a complete seasonal cycle are still missing. In this thesis an effort has been made to characterize LBL and the effect of errors (in model simulated LBL height) on pollutants species concentration estimations through modeling.

1.4(b) The surface layer

The lowermost part (one-tenth) of the ABL, closest to surface of Earth is termed as surface layer. It is in this layer that most significant exchange of heat, mass and momentum takes place, which can be studied through micrometeorological tower observations [Arya, 2001]. Although ABL top is well defined through various techniques, the top of surface layer is not physically well defined. The surface layer is also known as constant flux layer, implying variations of less than 10 % in magnitude vertical turbulent flux with altitude.

Knowledge of the diurnal variations of meteorological parameters and surface-layer characteristics is essential for improving the understanding of

mountain meteorology, assessment of the impact of topography in regulating ABL processes, as well as the accurate parameterization of the ABL processes, in order to improve the performance of atmospheric circulation models (e.g., *Helgason and Pomeroy* [2012]). Though, the knowledge of the basic circulation features over mountain terrain has been reasonably established (e.g., *Whiteman* [2000]), the measurements and in-depth understanding of the ABL processes over such terrain are rather poor as compared to flat homogeneous surfaces (e.g., *Moraes et al.* [2005]; *Nadeau et al.* [2013]). This is primarily because accurate observations of surface-layer characteristics over mountain terrain are difficult to make (e.g., *Wilczak et al.* [2001]; *Yuan et al.* [2011]), as these observations require a sufficiently large uniform fetch, especially in the upwind direction [*Stull*, 1988; *Arya*, 2001; *Moraes et al.*, 2005; *Rotach and Zardi*, 2007]. Though a few studies on the ABL circulation over the northern Himalayas have been carried out in the past [*Sun et al.*, 2007; *Chen et al.*, 2013], observations of the surface layer characteristics and their diurnal evolution are non-existent in the southern Himalayas. Such observations would be of paramount importance in quantifying the mountain circulation and providing insight into the transport of aerosol and trace species to the Himalayas from the adjoining plains, which are being utilized here by making use of ultrasonic anemometers installed at Manora Peak.

Based on the concepts stated in the previous sections on air pollution and mountain meteorology, the subsequent section describes the processes through which air pollution is linked with meteorology in context with mountainous terrain.

1.5 Association between air pollution and meteorology

The linkage between air pollution and meteorology is very much evident from previous subsections; however in context with complex mountainous terrain this association is still limited and incomprehensible. The primary meteorological factors

influencing air pollution are wind speed, ambient stability of the atmosphere and formation of inversions (radiation or subsidence). Along with the meteorological parameters, ABL depth diurnal variations control the concentration of pollutants to a large extent. Due to interplay between topographic variations and meteorological parameters some regions can have higher potential of trapping pollutants, in comparison to other regions.

For flat homogeneous terrain ABL depth is constant in space, with temporal variations induced due to thermal or mechanical processes, about which considerable understanding has been developed. However, for topographically complex terrain boundary layer depth varies actively with location and time, this complexity arises as a result of interaction between mountain and valley wind systems with the atmosphere. Over flat terrain agreement in turbulence profiles, temperature profile and aerosol vertical profile methods of daytime convective boundary layer (CBL) depth determination is quite good [Coulter, 1979; Hemmnemuth and Lammert, 2006], whereas this agreement fluctuates over mountainous terrain. LiDAR measurements are dependent on presence of air pollution for determination of the aerosol layer (AL) height, which can be considered as proxy for CBL height over flat terrain only. Over complex terrain CBL height are considerably lower than AL height, with CBL height following the underlying terrain more closely, with varying degrees during course of the day [De Wekker *et al.*, 2004]. This disagreement arises as a result of the profound influences which mountainous terrain exert on the mixing and transport processes in the atmosphere above, thus having the potential of transporting aerosols and humidity above the CBL. Formation of elevated aerosol layer [Wakimoto and McElroy, 1986; Neyki *et al.*, 2002; Solanki *et al.*, 2013] and deepening of surface-based aerosol layer, transforming into a residual layer after sunset [De Wekker *et al.*, 2004] are strong evidences of mountain topography influence on transport of air pollutants in free troposphere. Figure 1.5 provides a conceptual summary of various mechanisms of air pollution transport over mountainous terrain; the major processes

resulting in AL and CBL height differences are advective venting (AV) and mountain venting (MV).

MV also named as “chimney effect” [Lu and Turco, 1994], is the outcome of slope flows, with its strength depending on the synoptic winds and strength of slope flow convergence [Kossmann et al., 1999], MV initiated by moist convection is called as mountain cloud venting (MCV), generally resulting in formation of cumulus clouds over mountain peaks under low synoptic wind conditions. Both MV and MCV are particularly effective in transporting pollutants above the CBL and also lead to undulations in CBL top over mountainous terrain. AV on the other hand is involved with the leveling of CBL top undulations created by MV and MCV; AV take place as result of interaction between the undulations in CBL top and in regional winds or mountain wind system [Kossmann et al., 1999]. Thus, MV is involved with the vertical transport whereas AV leads to horizontal transport of pollutants over mountains.

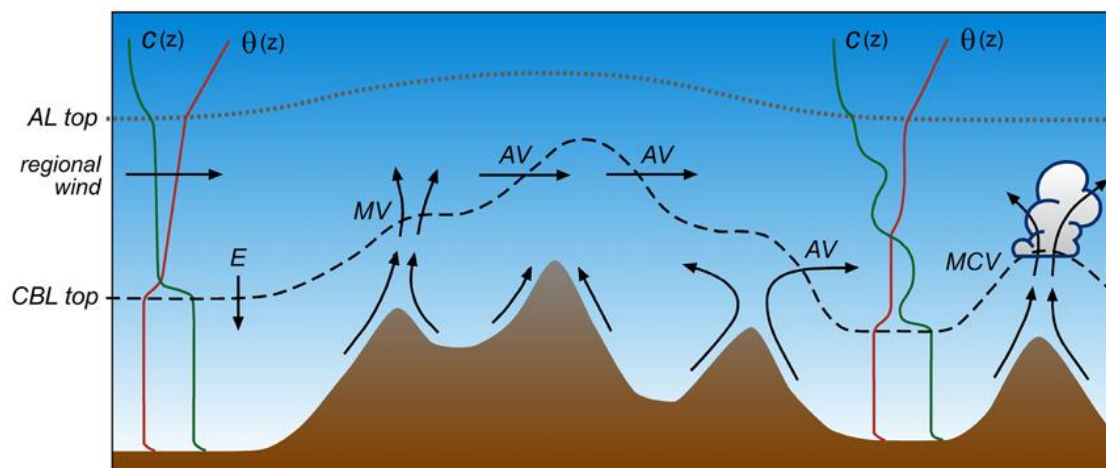


Figure 1.5: Schematic illustration of mountain induced exchange processes between the convective boundary layer and the overlying atmosphere (entrainment (E); mountain venting (MV); advective venting (AV) and mountain-cloud venting (MCV). Vectors indicate air flow while $c(z)$ and $\theta(z)$ indicate vertical profiles of pollutant concentration and potential temperature, respectively. The dotted and dashed lines indicate the top of the AL and the CBL, respectively (after Kossmann et al. [1999]; De Wekker [2002]; De Wekker et al. [2004]).

Due to hazardous accumulation of pollutants, the air-pollution meteorology for valleys and basins is rather well known as compared to slopes, ridges or mountain peaks. However, in order to develop a complete picture of air pollution interaction with mountain meteorology, studies over slope, ridges and mountain peaks are also important, especially over mountain peaks where atmospheric observatories are located in order to make regional representative measurements. The spatio-temporal variability in trace gas and aerosol measurement is significantly modulated by mountain meteorology, rendering variability in the scale (local or regional) which these measurements represent.

The Hindu Kush -Himalayan region forms the largest mountain range in the world with an area of 4.3 million square kilometers, influencing the weather and climate of India. The region that encompasses the Hindu Kush - Himalayan mountain range and the Tibetan Plateau is widely known as the “Third Pole” since it contains the largest reserve of ice fields (fresh water) outside the Polar Regions [Ye and Yu, 1998], thus affecting the radiation budget and climate of the globe. On the southern side of the Himalayas lies the IGP (Figure 1.6) infamous for its Atmospheric Brown Cloud (ABC) [Ramanathan et. al., 2007b], a huge blanket of brown haze composed primarily of sub-micron size aerosol particles (sulphate, nitrate and black carbon). By absorbing and scattering solar radiation, the ABC over IGP has implication for regional weather and climate; along with its impact on the global climate and climate change [Bonasoni et al, 2012] aided through the strong convection over North-east India and foothills of the Himalayas.

This thesis presents measurements of air pollution over a regional representative site in foothills of the central Himalayas, taking precise account of the meteorological process especially close to the ground surface. Figure 1.6 provides an overview of the problem being addressed, the Himalayas lies adjacent to the thick haze layer over IGP, transport of these pollutants in the deeper Himalayas is of profound importance in terms of their impact on the pristine atmosphere of the Himalayas, the fragile mountain ecosystem and the glaciers which feed rivers.

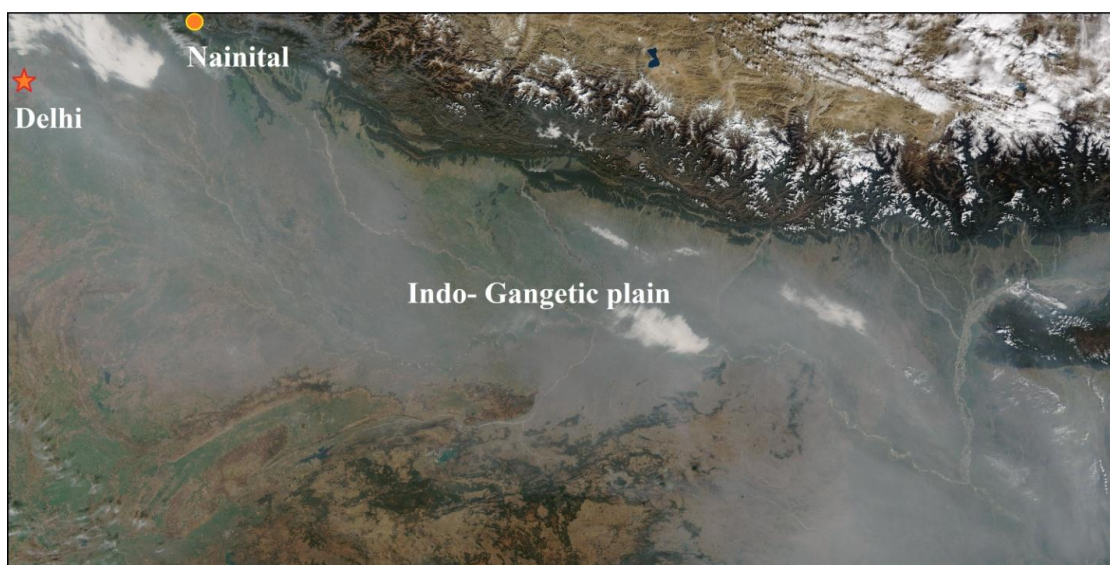


Figure 1.6: Satellite image of thick haze layer over the Indo-Gangetic Plains, hugging the Himalayas and spilling out toward the Bay of Bengal. The location of mega city Delhi and observational site (Nainital) for this thesis is illustrated with a star and circle respectively. The image has been taken by the Moderate Resolution Imaging Spectroradiometer (MODIS) on NASA's Terra satellite.

1.6 Objective and outline of the thesis

This thesis provides insight into the association between aerosol distribution and meteorology over a mountain ridge in the central Himalayas, taking into account a variety of temporal and spatial scales. This association is investigated through vertical profile measurements of aerosol, two-level fast-response surface measurements of wind components and temperature, along with the profiling of lower atmosphere through Radar. These three measurements form a formidable tool in understanding the mountain induced exchange process over the site. Through LiDAR measurements, inter-day and seasonal variations in aerosol vertical distribution over a mountain peak in the central Himalayas are investigated. For the first time over the Himalayas, the surface layer characteristics over a mountain ridge have been studied. Radar Wind Profiler (RWP) measurements provide insight into

the complete diurnal variations in mixing layer height over the site, along with the comparison of these measurements with model simulations.

Chapter 2 brings out the importance of the observational site. The instruments used for measurements for this study are discussed, providing the physical mechanism involved in the LiDAR and Ultrasonic anemometer measurements. The details of the data analysis carried on the raw measurements of aerosol profile through LiDAR, and two level wind components and temperature measurements in order to make them suitable for measurements are discussed. A new methodology of quantifying local boundary layer evolution over mountainous terrains is also presented.

Chapter 3 is about the inter-day and seasonal variations in aerosol vertical distribution over the site, identifying the possible sources through back-air trajectory analysis and discussion on processes involved in order to understand the observed variations. A comparison of the ground based LiDAR measurements with CALIPSO satellite retrievals is also made quantifying the bias in satellite measurements. A case study of elevated aerosol layer over the site is also presented.

Chapter 4 elaborates on the surface layer characteristics over the site during the spring and winter season, these measurements are first of its kind in the central Himalayas. Since the measurements are taken over a mountain ridge the applicability of Monin-Obukhov similarity theory (MOST) is also investigated. The spring and winter season represent strong and weak synoptic flow conditions respectively, thus providing an insight into the interaction between regional circulation and mountain wind systems.

Chapter 5 is on the Local boundary layer (LBL) dynamics over the site, presenting RWP measurements of mixing layer height during November 2011 to March 2012. The chapter reveals the peculiar characteristics of LBL over mountainous terrain, as well as the role of topography in transforming surface layer into residual layer after sunset hours during strong wind conditions. The mixing layer height measurements were also simulated through WRF model and a

comparison between ground based and model simulations is investigated, along with the implication of difference between model simulations and observations of LBL height on air-quality studies.

Chapter 6 provides a brief summary of the thesis highlighting the major conclusions in context to what has been achieved and scope for future work in this direction.

Chapter # 2

Observational site, instrumentation and methodology

This chapter deals with the site description, instrumentation, and methodology used to interpret data. All the ground based observations described in this chapter have been conducted over a mountain top observatory in the foothills of the central Himalayas. The data bank is majorly made up of two instruments, a LiDAR and a set of ultrasonic anemometers; however observations made with Radar Wind Profiler (RWP) during GVAX campaign are also utilized. With LiDAR data vertical profiles of aerosol have been estimated, through an intricate method for estimating LiDAR ratio. The two levels of ultrasonic anemometers provide fast response data of wind components and temperature which is carefully subjected to quality checks; with this filtered and corrected dataset surface layer characteristics are being investigated. Along with these instruments, RWP measurements have also been analyzed in order to understand local boundary layer over the site.

2.1 Strategic location of site

The observational site, named as Aryabhatta Research Institute of Observational Sciences (ARIES) situated on a mountain peak (Manora Peak, 79.5°E, 29.4°N and 1958 m AMSL), is a strategically important location for climate change studies in the central Gangetic Himalayan region [Sagar *et al.*, 2015]. Manora Peak is a high altitude regional representative site in central Himalayas [Kumar *et al.* 2010], known for intensive studies on synoptic wind patterns and trace gases [Sarangi *et al.*, 2014], balloon soundings [Ojha *et al.*, 2014] and aerosol extinction profiles [Hegde *et al.*,

2009; Srivastava *et al.*, 2011a; Solanki and Singh, 2014]. In general, ARIES is well known for its fundamental research on atmospheric sciences, astronomy & astrophysics, and solar physics.

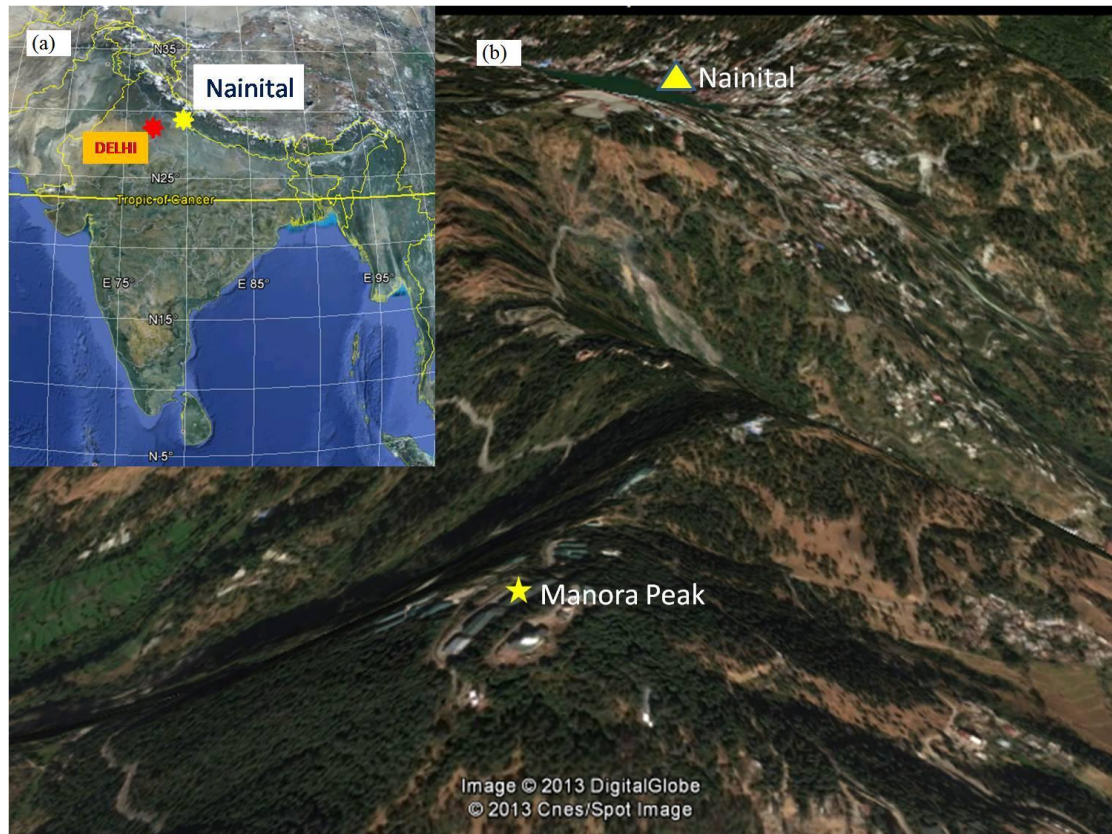


Figure 2.1: Geographical location (marked by yellow star) of observation site at Nainital and nearest megacity Delhi (marked by red star), on the map of India (b) The topography around observation site Manora Peak, and the city of Nainital, in the Google earth imagery.

The observational site is situated at an aerial distance of about 2 km from the city of Nainital, a famous tourist place in North India as shown in Figure 2.1. Observations are being made at the peak of the mountain with steep slopes on the eastern and western sides. To the south of the peak, mountains gradually decrease in altitude merging into a small city called Haldwani, whereas in the North and North-

East higher altitude mountains create complex topography. Overall image of site reveals the complex terrain of the central Himalayas.

The site is free from any major local source of aerosol or anthropogenic activities, hence, considered to be pristine [Sagar *et al.*, 2004], but due to complex topography it has got a local boundary layer (LBL) different from the planetary boundary layer (PBL). The extensive measurements of the LBL depth during different seasons over this site are not available; however RWP measurements made over a period of 5 months have been presented in this thesis (Chapter 5). The site is considered to be ideally in the free troposphere (except for the spring season) since, the model simulated average planetary boundary layer height at a nearby low altitude site Pantnagar, does not evolve above 1.5 km, except in the spring season when the average PBL or mixed layer depth goes up to 4 km [Ojha *et al.*, 2012], however ground based measurement are still missing for actual and real time ABL observations. Since, the site is located at 2 km AMSL on a mountain peak, it is quite likely that over such terrain a stable surface layer exists somewhere between few tens of meters to about 200 m under various atmospheric conditions, depending upon the turbulence and other factors. Also, settling of daytime elevated aerosol layers in association with valley flows and down-slope winds on the slopes of the mountains, take place after sunset. The LiDAR observations presented in this thesis being exclusively nocturnal, therefore, the vertical profile represents the aerosol loading above the PBL. However, on a few occasions strong horizontal gusty winds up to 20 ms^{-1} and upward vertical (with respect to gravity) winds of magnitude as high as 3 ms^{-1} are experienced after the sunset, which can mix the settled boundary layer up to about 1 km, above the site, through orographic lifting of the mountain even during the night time (this phenomenon will be discussed in chapter 5).

ABL characteristics over mountainous terrain are nearly unexplored in context with the Indian subcontinent, thus a micrometeorological laboratory has been established at ARIES, under the NOBLE (Network of Observatories for Boundary Layer Experiment) project of Indian Space Research Organization's Geosphere-

Biosphere Program (ISRO-GBP). In the NOBLE project, ARIES site is a regional representative of complex mountainous terrain of the central Himalayas, with primary objectives as follows:

- (i) Characterization of ABL / LBL processes and their diurnal evolution over complex mountainous terrain (variations in air flow over the ridge),
- (ii) Investigate the role of ABL / LBL in modulating mesoscale circulation over the foothills of the Himalayas,
- (iii) Assess the role of ABL / LBL in modulating the thermodynamics of free-troposphere, and
- (iv) To improve the ABL parameterization schemes in numerical models, through the knowledge derived from (i), (ii) and (iii).

As depicted in Figure 2.2 (a) the region ($0.50^\circ \times 0.50^\circ$) around the site encompasses a series of ridges and valleys in the Northeast (315 to 135 degrees), whereas towards the Southwest direction (135 to 315 degrees) is the Indo-Gangetic plains (IGP), representing the contrasting feature of elevated mountainous terrain on one side and flat terrain on the other, and the site being on the transition line. On a wider perspective, elevation of the Himalayan mountain range in the Indian region generally increases northward; within a distance of 120 km around Nainital, the surface elevation increases northward from < 300 m (in the northern part of the IGP) to above 5000 m in the north.

On the local scale (which is important in governing the surface-layer characteristics), the site is located close to a mountain ridge. The ridge axis is aligned approximately along the north-west direction. The observational site has 600 meters deep valleys on the eastern and western sides and the valley axes are aligned approximately in the SE and SW direction, respectively. The mountain peak has a slope of approximately 25 degrees on the eastern and western side, and is covered with a dense forest on all sides, consisting mainly of trees and shrubs, as depicted in Figure 2.2 (b). All measurements presented in this study were made on the mountain peak with no obstructions such as buildings or trees in any direction, an important

factor of consideration for measurement of wind components and temperature fluctuations, thereby avoiding non-representative measurements.

The measurement techniques and instrumentation used in addressing the objective of this thesis are described under subsequent headings.

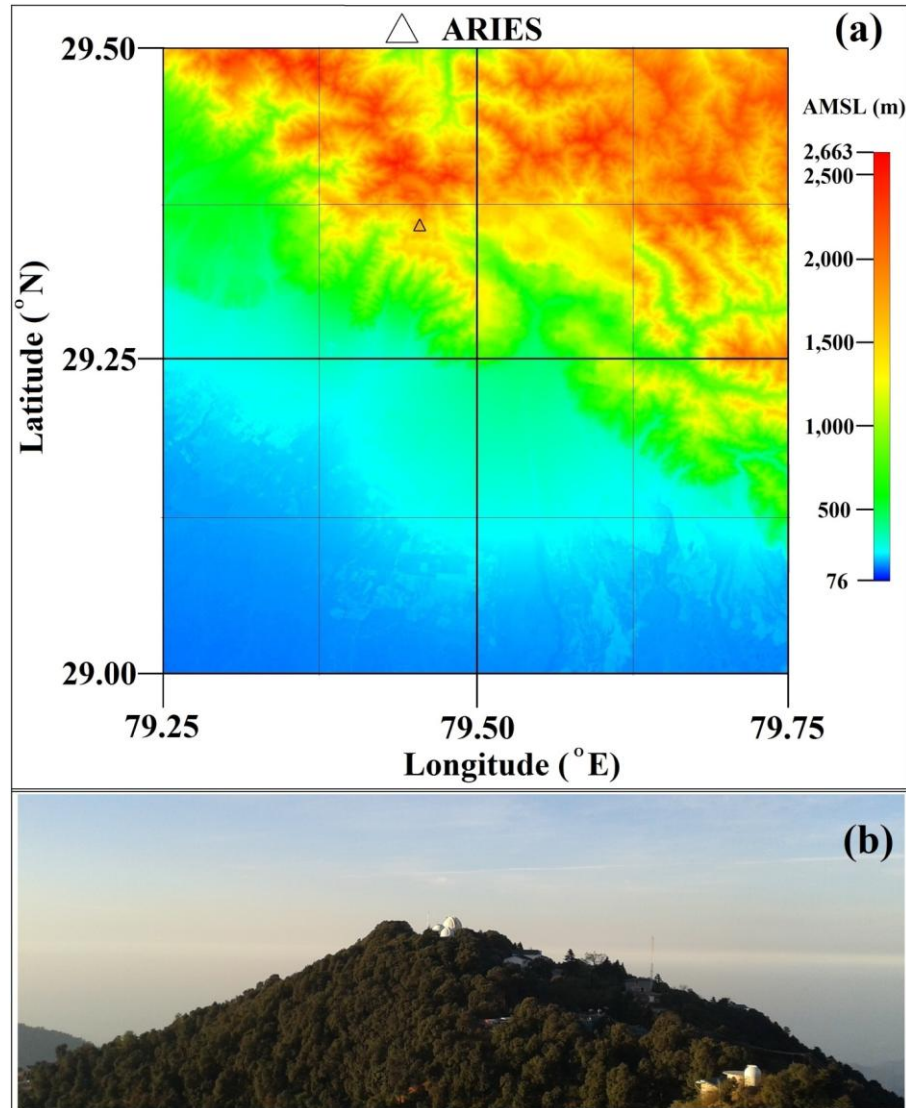


Figure 2.2:(a) Topography of the region around ARIES, Nainital, (b) Photograph of the site taken from the nearby peak of almost equal elevation as Manora peak, situated in the north-east direction.

2.2 LiDAR

LiDAR is the acronym for light detection and ranging technology which employs light waves for identifying the target and estimating distances; the technology is similar to RADAR (SODAR) which uses radio (acoustic) waves for locating objects and their motion. The basic principle of detection and ranging is illustrated in Figure 2.3, wherein a signal is sent towards the object of interest and the backscattered signal from is object is collected by receiver, thus estimating the distance (along with many other parameters based on the technology being used) of the object (scatterer) from observing system.

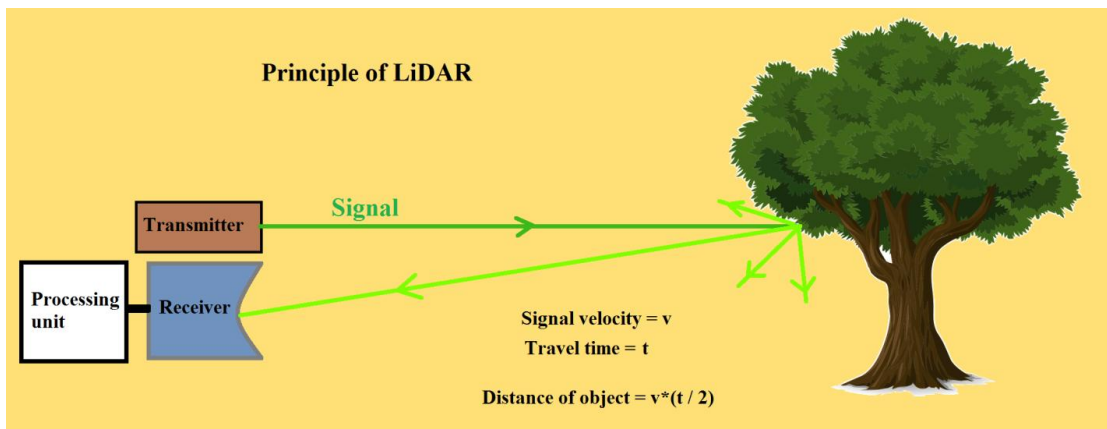


Figure 2.3: The basic principle behind detection and ranging.

The LiDAR technology has tremendous applications (primarily being used in high resolution mapping of surfaces) in fields such as atmospheric remote sensing, agriculture, Geology, Biology, Astronomy, Archaeology, etc. In atmospheric sciences LiDAR is used in ground-based, aircraft and satellite-borne measurements providing details on the vertical profile of aerosols, clouds, winds and atmospheric components. LiDAR technology has advanced quiet a lot during last 50 years, resulting in a variety of LiDAR such as Doppler LiDAR, Rayleigh LiDAR, differential absorption LiDAR (DIAL) and Raman LiDAR. In this thesis, ground based and space-borne LiDAR measurements have been utilized and the following section will provide details on the ground based LiDAR, at ARIES.

2.2(a) LAMP

The advanced version of micro pulse LiDAR System, popularly known as LAMP (Figure 2.4 (a)), designed and developed by National Atmospheric Research Laboratory (NARL), is installed in a temperature and humidity controlled environment at ARIES, Nainital under a joint scientific collaborative program. The LAMP is utilized for the vertical profiling of atmospheric aerosols in the lower troposphere as well as observations of cirrus clouds. This portable micro pulse LiDAR system is basically operated during night in the presence of stable boundary layer when day time well mixed aerosols settle and form layers of suspended particles at various levels in the atmosphere.

LAMP system employs a diode pumped Nd-YAG laser system, a coaxial transceiver for transmitting the laser pulses and detecting the backscattered photons, a dedicated data acquisition system and a computer control with an interface system. The pulses of light (532 nm) energy are transmitted from telescope into the atmosphere. As the pulse propagates, part of it is scattered by molecules, water droplets, ice crystals (cirrus clouds), dust and haze aerosols in the atmosphere, and small portion of back scattered light is collected by the telescope and then detected by an in-built photo multiplier tube. The distance to the particle layer is derived from the time delay between each outgoing laser pulse and the backscattered signal. Schematic of the system (Figure 2.4(b)) and details are provided by *Bhavani Kumar* [2006]. Major specifications and system parameters are given in Table 2.1.

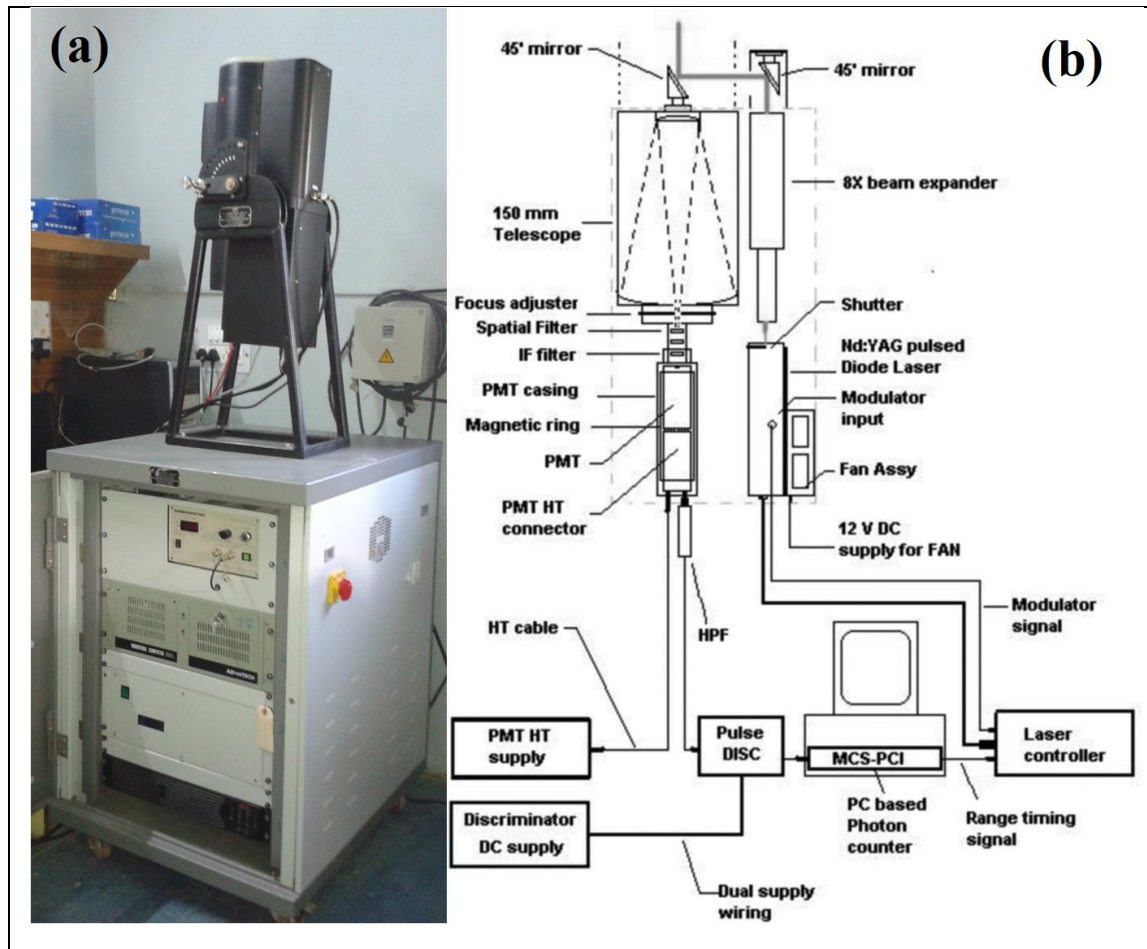


Figure 2.4: (a) LAMP system at ARIES, (b) schematic block diagram of the LAMP system.

The LAMP system sends a laser pulse of width 10 ns and receives backscattered signal at the vertical resolution of 15 m, operating at pulse energy of 4 μJ per pulse and pulse repetition frequency of 2.5 kHz. The range corrected, normalized return signal for one transmitted laser pulse is a combination of backscatter energy from scattering of light by air molecules and particulate matter, thus constituting two types of scattering mechanisms: Rayleigh and Mie. Rayleigh scattering is the dominant type of molecular scattering in atmosphere which takes place when size of scatter is smaller relative to the wavelength (λ) of incident light, this scattering is proportional to the λ^{-4} ; the amount of scattering being equal in forward and backward direction. On the other hand Mie scattering is dominant when particle size is almost equivalent

to the wavelength of incident light with its intensity varying as a complex power of λ , this scattering depends on the geometric shape and size of the particle and the amount of scattering is greater in the forward direction which increases with the size of particle.

Table 2.1: LAMP system: parameters and specifications.

Laser source	
Type	Pulsed diode pumped solid state laser
Operating wavelength	532 nm
Pulse width	<10 ns
Repetition rate	2500 Hz
Beam size	0.4 mm
Polarization	Linear
Beam divergence	< 1.5 mrad
Beam expander magnification	8X
Divergence of the expanded laser beam	< 200 μ rad
Telescope	
Type	Cassegrain
Size	Dia 150mm , f# 9
Field of view	< 400 μ rad
Telescope mount	Gimbal
Filter	
Type	Interference
Central wavelength	532 nm
Full width at half maximum	0.5 nm
Recommended operating temperature	$30 \pm 1^{\circ}\text{C}$
Detector	
Type	Photomultiplier, Hamamatsu R3234
Gain	2.5×10^7 (typical)
Quantum efficiency	<10%
Data Acquisition System	
Model	EG&G Ortec, MCS-pci
Maximum counting rate	150 MHz
Dwell time selectable	100 to 1300 ns
Number of channels	4 – 65536

The LAMP system does not require overlap correction, since it is a coaxial LiDAR and field of view (FOV) of the receiver telescope is $< 400 \mu\text{rad}$, which is double than the divergence of the expanded laser beam. With this arrangement, a complete overlap between the laser beam and the telescope FOV was achieved at every altitude above 150 m, 0 to 150 m is the dead zone (blind region) for the LAMP. The expression for the power of backscattered signal for a coaxial LiDAR configuration is given by

$$P(z) = E_0 \frac{k}{z^2} \beta(z) T^2(z) + P_b, \quad [2.1]$$

where P_b is the background signal from the sky, E_0 is the laser pulse energy, $\beta(z)$ is the total (Rayleigh and particulate backscatter) volume backscatter coefficient, $T(z)$ is the total volume extinction coefficient and k is a calibration constant of the LiDAR system, which is determined from the LiDAR signal $P(z_c)$ at a reference calibration range z_c . A reference height (z_c) of 9 km AMSL was chosen since the aerosol backscatter is negligible compared to the known molecular backscatter value at such an altitude. To obtain the Rayleigh backscatter one requires the temperature and pressure vertical profile, we have obtained these profiles from the Modern-Era Retrospective analysis for Research and Applications (MERRA) reanalysis database. Considering the aerosol properties and size distribution to be homogeneous throughout the vertical column of atmosphere, we assumed a constant LiDAR ratio (LR) (discussed in section 2.2(b)) for aerosol during individual observations while computing the aerosol backscatter coefficient, using the stable backward iteration technique given by and *Fernald* [1984] and *Klett* [1985]. The LiDAR equation derived after the Fernald- Klett formulation is given as:

$$\beta(z) = \frac{\exp[-\{S(z_c) - S(z)\}]}{\frac{1}{\beta(z_c)} + 2(LR) \int_{z_0}^{z_c} dz \exp[-\{S(z) - S(z_c)\}]} \quad [2.2]$$

The vertical profile of aerosol backscatter coefficient is computed by solving the following equation:

$$S(z_c) - S(z) = \ln[z_c^2 P(z_c)] - \ln[z^2 P(z)] - \frac{3}{4\pi} \int_{z_0}^{z_c} \beta_R(z) dz \quad [2.3]$$

$$+ 2(LR) \int_{z_0}^{z_c} \beta_R(z) dz$$

$$S(z) = \ln X(z) \quad [2.4]$$

Where X is the normalized range corrected signal (NRCS) and β_R is the Rayleigh backscatter.

Cloud contaminated profiles are screened based on the criterion by *Kim et al.*, [2007], such that all the profiles with aerosol extinction greater than 500 Mm^{-1} could be excluded from the analysis. The LiDAR inversion method described above contains four major sources of uncertainty as discussed by *Lewandowski et al.*, [2010]. The overall uncertainty of the extinction coefficient from LiDAR inversion algorithm comes out to be 5%. The main sources of error in the retrieval are unknown LR profiles and the missing first 150 meters (termed as the blind region of LiDAR) which may significantly contribute to the AOD. To minimize the error due to the blind region on retrieval process the estimated extinction coefficient (through LiDAR) closest to the ground is chosen to represent the extinction in the blind region (0 to 150 m AGL). The accuracy of calibration of LiDAR measurements is estimated to be 5%.

2.2 (b) LiDAR ratio approximation

The LiDAR ratio is a complicated spatial and temporal function that depends on the composition, size distribution and shape of the aerosol [*Cattrall et al.*, 2005]. In this thesis, the LiDAR being used is monochromatic (532 nm) providing information of backscattered energy returned as a function of time (or distance), from which one can retrieve the aerosol backscatter coefficient profile, although critical assumptions have to be made in the inversion of the LiDAR signal in order to obtain aerosol optical properties. LiDAR derived aerosol optical depth (LiDAR-AOD) is the integrated aerosol extinction coefficient (ground level to 7 km AGL), which is

compared with AOD from Moderate-resolution Imaging Spectroradiometer (MODIS-AOD) in order to determine the LR based on an approach followed by *He et al.* [2006] and *Leon et al.* [2009]. The difference in wavelength between MODIS and LiDAR is negligible and correlation between daytime measurements of MODIS-AOD and sun photometer AOD is reasonably good (0.50 - 0.80 during different seasons) over the site, thus the measurements of MODIS-AOD can be implemented reliably for comparison. A comparison of MODIS-AOD with ground based AOD measurements at Manora peak during a dust storm is available in *Srivastava et al.* [2011].

By using an iterative method, LR was changed in steps of 0.5 sr for minimizing the difference between LiDAR-AOD and MODIS-AOD, selecting the LR for minimum difference as the best estimate. Although earlier studies, carried out with LAMP [*Hegde et al.*, 2009, *Badrinath et al.*, 2009, *Sinha et al.*, 2013] have assumed a constant LR of 28.57 for extracting the aerosol backscatter profile during different observations, whereas more appropriately we derived LR for each individual observation. Additionally, we attempt to compare some of the nighttime CALIPSO retrievals with daytime MODIS-AOD (used to constrain nighttime LiDAR inversion), as it is the best possible approach in current scenario and uncertainties involved in the approach has been addressed by *Royer et al.* [2010]. The low values of LR during the winter season (10 sr to 18 sr) were obtained under the prevailing pristine conditions with low AOD (<0.1). During the spring and post monsoon season when daytime AOD over the site was above 0.5 and the sky was quite hazy in nighttime, the LR was estimated to be in the range of 35 sr to 44 sr. This is how the variability in aerosol vertical distribution is studied using ground based measurements; these measurements were validated with CALIPSO satellite (space borne LiDAR) measurements, which will be described in Chapter 3. In the next section we describe the measurements taken close to ground surface, in order to understand the variations in meteorological parameters.

2.3 Ultrasonic anemometer

A three dimensional ultrasonic anemometer basically consists of 3 pairs of ultrasonic transducers, with each transducer acting as a transmitter and receiver of acoustic signal. The distance between the transducers is fixed, thus the travel time for signal in calm air is known a priori. Since wind flow will affect the signal propagation velocity, thus superposition of wind flow on the three pair of measurements results in different propagation intervals. Altogether, these three pairs of (non-orthogonal) independent measurements are resolved through vector transformations resulting in the measurement of the three orthogonal wind velocity components and speed of sound. The speed of sound is derived for motionless atmosphere, depending on air temperature and humidity, thus corresponding to measurement of acoustic equivalent of virtual temperature [Kaimal *et al.*, 1990]. The measurement principle of ultrasonic anemometer is illustrated in Figure 2.5. The specifications of the ultrasonic anemometer (USA) used for this study are listed in Table 2.2.

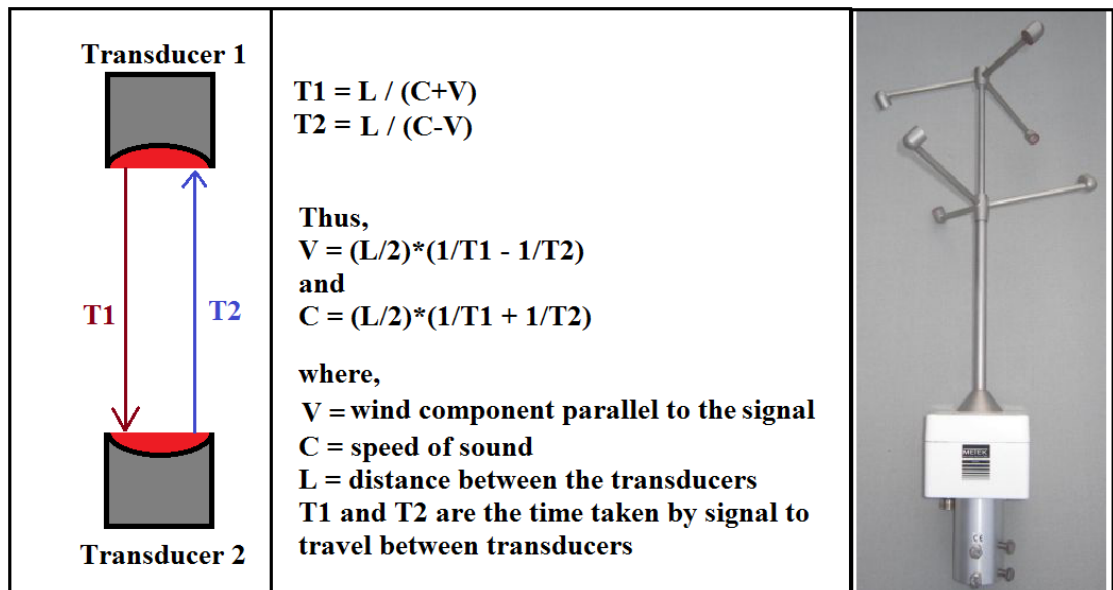


Figure 2.5: Measurement principle of ultrasonic anemometer and its photograph.

Table 2.2: Specifications of USA-1 “Scientific”

	Measuring range	Resolution	Accuracy ^{3***} At horizontal wind speed: 20 m/s < x < 50 m/s
Wind speed	0 to 45 m/s;(For raw data) 0 ... 60 m/s (averages > 60 seconds)	0.02 m/s ^{1*} -or- 0.01 m/s ^{2**} ^{1*} for instantaneous data ^{2**} for averages (≥ 1s)	±2 % (at wind speed 1 m/s: ± 10 cm/s) (at wind speed 4 m/s: ± 15 cm/s) (at wind speed 10 m/s:± 30 cm/s)
Wind direction	0 to 360 degree	1 degree	±2 degree (at wind speed 1 m/s: ± 5°) (at wind speed 4 m/s: ± 3°) (at wind speed 10 m/s: ± 2°)
Wind components	-45 to +45 m/s;(for raw data) -60 to 60 m/s (averages > 60 seconds)	0.01 m/s	^{3***} Indications for accuracy are worst case values. Deviations are typically smaller.
Temperature	-30 to +55 °C derived from the sound velocity, compares to the virtual temperature	0.01 K	

The ultrasonic measurements described in this chapter are taken with ultrasonic anemometers mounted on a 27 m meteorological tower instrumented at two levels: 12-m and 27-m (Figure 2.6(a) and (b)). Booms of 2 m length are provided for mounting the sensors, which comprise of three-axis sonic anemometer (Make: METEK, GmBH, Germany, Model: “USA-1 Scientific”), slow response hygristor and air temperature sensors (PT-100 1/3 DIN, 4 wire - technique). Location of the meteorological tower with respect to the mountain peak is shown in Figure 2.6(c).

The 27 m meteorological tower (base of the tower) is installed on the western side of the peak at an altitude ≈ 15 m lower than the mountain peak and at a horizontal separation of ≈ 160 m between the two. The slope within a horizontal distance of 1 km is about 16° on the western side of the mountain crest (where the observation site is located), while on a relatively larger scale (horizontal distance of 10-15 km), the slope ranges from $4-8^\circ$ on all sides; the slope towards the north is rather small within this horizontal distance. The north-western valley adjoining the ridge is covered with trees, up to a horizontal distance of over 400 m, which is primarily the upwind direction during the spring season. However, the area near the tower and the mountain top is rather barren.

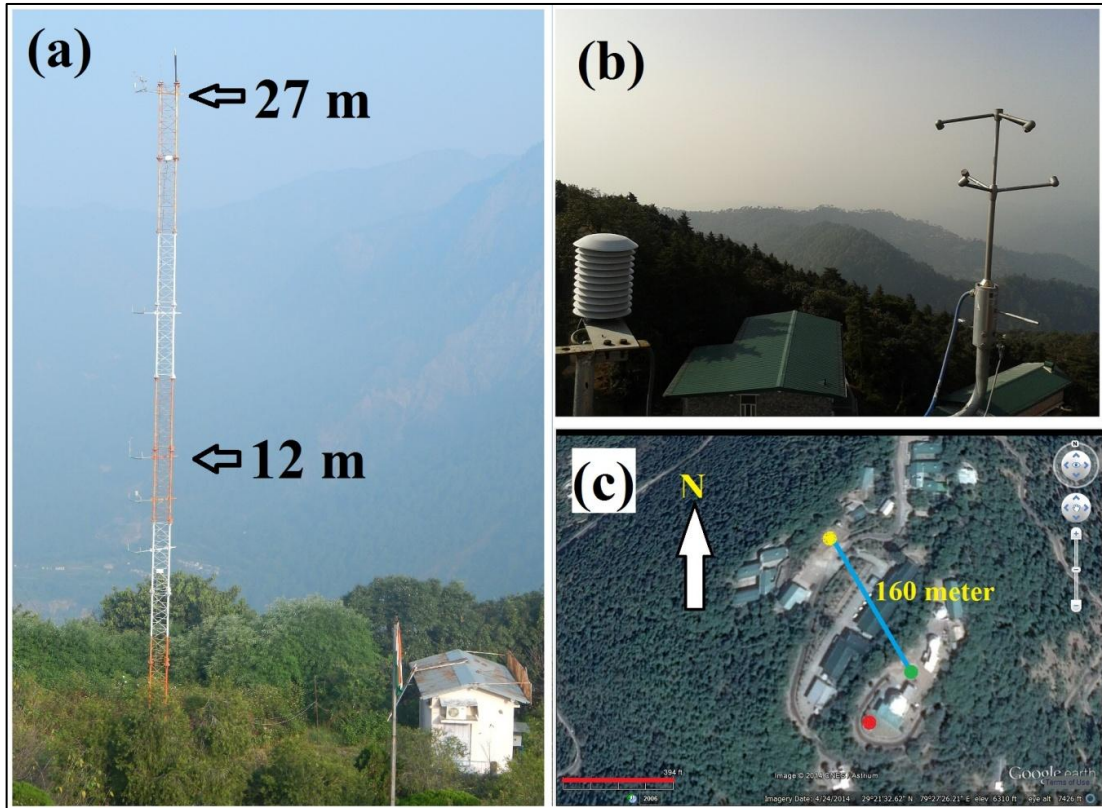


Figure 2.6: (a) 27 m meteorological tower instrumented at two levels, (b) ultrasonic anemometer and hygrometer at 27 m level, and (c) Location of 27 m tower (yellow dot) with respect to the mountain peak (green dot), and collocated AWS (red dot) at the site.

All sensors have been factory calibrated before mounting on the tower. The three orthogonal components of wind and acoustic temperature are measured using the sonic anemometers operating at 25 Hz. Sonic anemometer USA-1 is equipped with a three dimensional (3D) head-correction for angle of attack in the range of $\pm 45^\circ$. The correction factors incorporated in the sensor are determined using wind-tunnel tests carried out and implemented by the manufacturer. This function corrects the flow distortion of the sensor head based on the horizontal and the vertical wind components.

The acoustic temperature (T_s) measured using the sonic anemometer is converted to virtual temperature (T_v) using the equation $T_s \approx T_v - 0.02 * p$ (p being the partial pressure due to water vapour). As the observations used in this study were carried out very near a mountain ridge, with the top level sonic anemometer located above the ridge surface level, the sonic anemometers were mounted in true vertical position (in the direction of gravity), rather than along the local normal (perpendicular to the local surface). Tilt correction are then applied to these measurements before estimating the turbulence parameters and fluxes.

The humidity and temperature measured using the slow response sensors are averaged for 1 min. The surface meteorological observations and the incoming shortwave solar radiative flux are observed using a collocated automatic weather station (AWS) installed by the Indian Meteorological Department (Figure 2.5(c)). These instruments are mounted at 10 m height above ground level at the mountain top (which is about 160 m from the sonic anemometer tower horizontally) and mounted vertically, as the observations are taken at the mountain top. Hourly averaged meteorological data is utilized to understand the background meteorological conditions over this site. Analysis of the micrometeorological observations are further strengthened by a log-book on the prevailing weather conditions (sky condition, amount and type of clouds, appearance of fog, convection, and thunderstorms in the vicinity of the experimental site) noted manually every three hours.

2.3(a) Planar fit method

The mean streamlines near the surface in a sloping terrain are expected to be parallel to the terrain unless the flow separation occurs. Over a sloping terrain, estimation of surface-layer turbulence and fluxes will require a mean streamline-following coordinate system. Generally, sonic anemometers are placed with z-axis oriented perpendicular to the local surface for avoiding artefacts in the measured vertical winds caused by the interaction of horizontal winds with the terrain. For anemometers placed in true vertical coordinate system (z-axis along the direction of gravity) in a sloping terrain, fluctuations in the stream wise velocity will create an apparent stress, magnitude of which varies with slope angle relative to wind direction [Geissbuhler *et al.*, 2000; Wilczak *et al.*, 2001; Yuan *et al.*, 2007, 2011; Richiardone *et al.*, 2008]. Before analyzing the data, the tilt corrections are applied to sonic anemometer data using the planar-fit method (PFM) [Wilczak *et al.*, 2001; Yuan *et al.*, 2007, 2011; Richiardone *et al.*, 2008], thus making the measurements comparable to those over other sites. Studies reported in the literature show that the planar-fit technique has considerable advantages in sonic anemometer tilt correction, compared to the double and triple-rotation methods for rotation of the anemometer with respect to streamlines [Wilczak *et al.*, 2001; Yuan *et al.*, 2007]. Wilczak *et al.* [2001] compared different methods for correcting tilt angles relative to the mean streamline coordinate system. They showed that the double and triple rotation methods might lead to significant run-to-run stress errors due to sampling errors of the mean vertical wind velocity and cross-wind stress. The planar-fit method (PFM) has been shown to reduce the run-to-run stress errors and provide unbiased estimates of lateral stress [Wilczak *et al.*, 2001]. The PFM estimates a set of tilt angles for a set of data runs and is less susceptible to sampling errors. One of the conditions for the application of PFM is that the tilt of the sonic anemometer and its orientation with respect to the terrain slope should not be altered over the duration of the data being analyzed, from which the tilt angles are estimated [Wilczak *et al.*, 2001]. As the PFM provides offset of the mean vertical wind speed, it can also be used to estimate the vertical advection

(e.g. that caused by mountain valley circulation) using the residual vertical winds obtained after the PFM rotation (e.g., *Yuan et al.* [2007]).

The data obtained from the sonic anemometers mounted in true vertical direction near the mountain ridge are converted to the streamline-following coordinate system (thus correcting for the sensor tilt with respect to local normal) using the PFM algorithm as per the details provided in *Wilczak et al.* [2001] and *Yuan et al.* [2007, 2011]. The major steps for applying PFM on a dataset are as follows:

- (i) Firstly generate averaged (30-min) wind components (u, v and w) file for the entire season or data period under consideration, making individual file for different sectors.
- (ii) Secondly, apply the code provided in appendix of *Wilczak et al.* [2001] to the files generated in (i) and the output of the code will be a set of planar fit coefficients (b_0 , b_1 and b_2) for each sector.
- (iii) Finally, take the raw data file (25 Hz data as in this case) and based on the direction of the wind apply the planar fit coefficients for each set of data points (u, v and w), according to the equations (5) and (6) of *Yuan et al.* [2007]

While *Wilczak et al.* [2001] derived a single set of tilt angles for all wind directions; *Yuan et al.* [2007, 2011] suggested that the tilt angles for different mean wind directions (typically estimated at 30° interval of wind direction) could be different. However, during most of the observation period in spring season, the winds are predominantly in the north-westerly direction (270 to 310°) and the data set for other wind directions were rather infrequent (Figure 2.7 (a)) to reliably estimate the tilt angle corrections at different wind directions. Hence, the mean tilt angles are estimated by considering the whole data for the spring season. For the spring season, observations for a total of 46 days have been used for estimating the mean tilt angles using PFM. Values of the regression coefficients b_0 , b_1 and b_2 (Eq. 4 of *Yuan et al.* [2007]) obtained are -0.0059 , 0.2211 , and -0.2872 respectively, and the estimated tilt angles are -12.00° (angle α in the x-z plane) and -16.03° (angle β in the y-z plane).

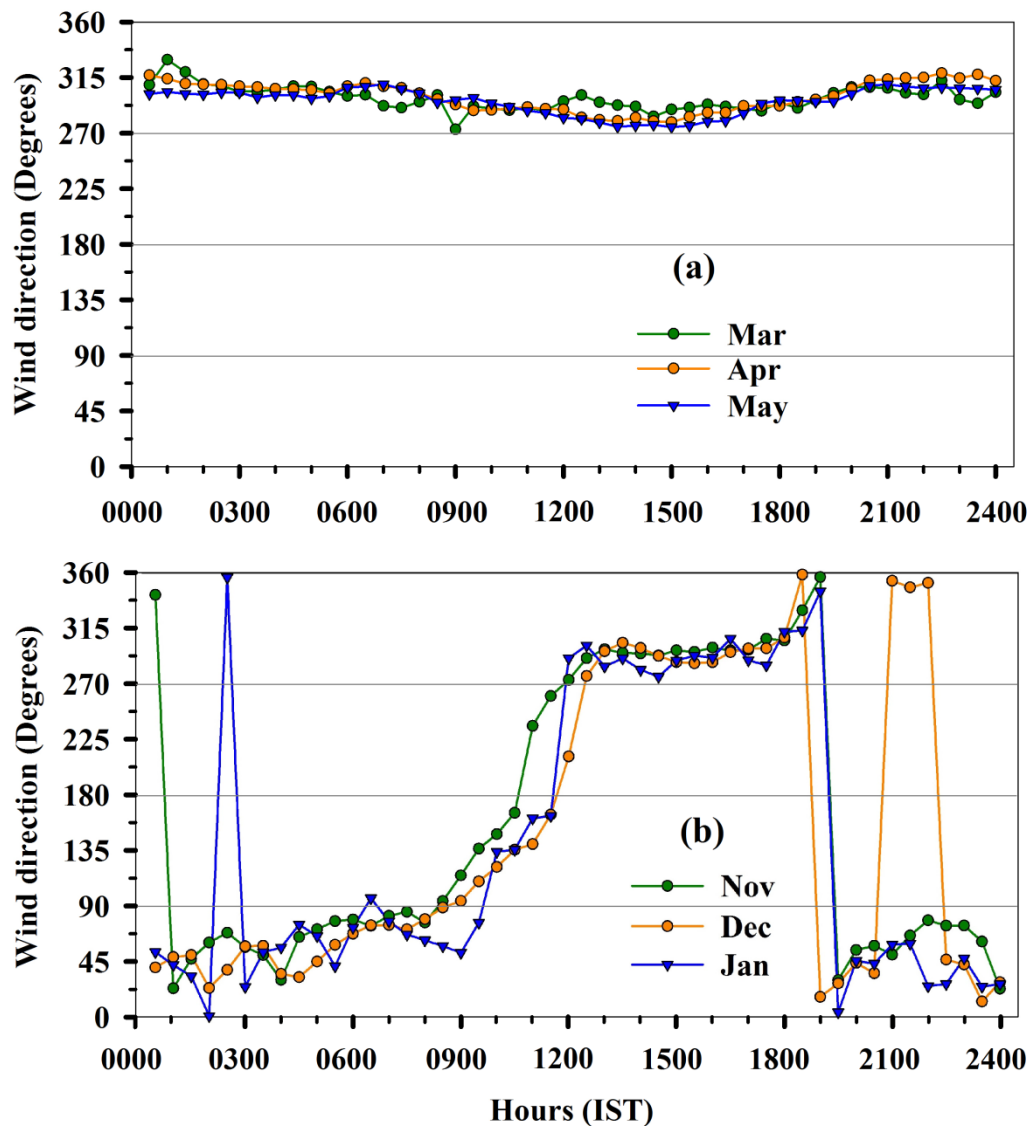


Figure 2.7: Monthly averaged diurnal variations in wind direction for the (a) spring and (b) winter season.

Figure 2.7 (b) shows the monthly averaged wind direction during winter season, clearly presenting the easterly and westerly as two prevailing wind directions, and hence the dominance of mountain circulation over synoptic-flow. Wind direction undergoes a gradual change from 0900 - 1200 IST, transiting between easterly flow of nighttime (2000 – 0800 IST) and westerly flow in daytime (1300 – 1900 IST), the

gradual change in wind direction could be associated to the variations in heating of the mountain slopes as the day evolves.

The contour map (Figure 2.8) of the site depicts in-depth detail of the topography around the site revealing an interesting topographical feature: the site is located at the trisection point of three ridges which appear to be form the Greek alphabet lambda “ λ ”, thus on a horizontal scale of approximately 1 km by 1 km centered at the site one can identify three distinct sectors (S1, S2 and S3) as marked on the contour map.

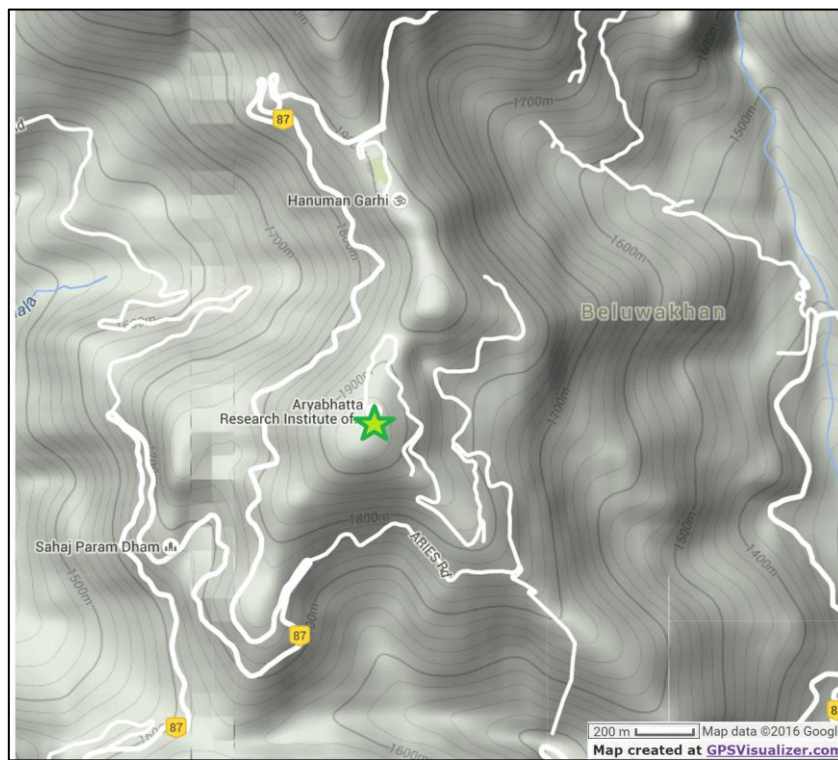


Figure 2.8: Terrain contour map of the topography around the site (marked by green star).

Although, planar fit approach [Wilczak *et al.*, 2001] is considered preferable for aligning wind measurements coordinate system to the mean wind over sloping terrain, taking into account the complex topography of site and diurnal variability of

wind direction, for the winter season we have applied sector-wise planar fit (SPF) [Yuan *et al.*, 2007; 2011] on the dataset, dividing the data into three sectors of 120 degrees each, the first sector, S1(0 to 120 degrees) comprises of the wind flow during the nighttime hours, the second sector,S2 (120 to 240 degrees) represents the transition period from (0900 to 1300 HRS), whereas the third sector, S3 (240 to 360 degrees) involves wind flow from afternoon hours until sunset. For the three sectors the data base was segregated on the basis of the half hourly averaged wind direction and the mean SPF coefficients were estimated for each sector at both levels, the estimated coefficients are tabulated in Table 2.3; it is noteworthy to mention that for hilly terrain in order to derive stable SPF coefficients, for each sector two hundred 30-min datasets are sufficient [Yuan *et al.*, 2011].

Table 2.3: Sector wise planar fitting coefficients for the observation period (November 2013 to January 2014).

Sector range (Degrees)	Number of 30-min Data sets		Pitch angle α in the x-z plane (degree)		Roll angle β in the y-z plane (degree)		Zero offset b_0	
	27 m	12 m	27 m	12 m	27 m	12 m	27 m	12 m
0° to 120°	1200	1013	-9.98	-15.52	-15.58	-12.28	+0.0635	+0.0330
120° to 240°	302	329	-9.50	-10.41	-19.80	-14.30	+0.2075	+0.0499
240° to 360°	1330	1490	-8.66	-7.48	-14.86	-15.91	-0.0153	-0.0493

The dataset before and after planar fit correction is illustrated in Figure 2.9, PFM (or SPF) basically reduces the amplitude of variations in tilt angle to less than $\pm 15^\circ$, thus making the raw-data streamlined with respect to the terrain following coordinates.

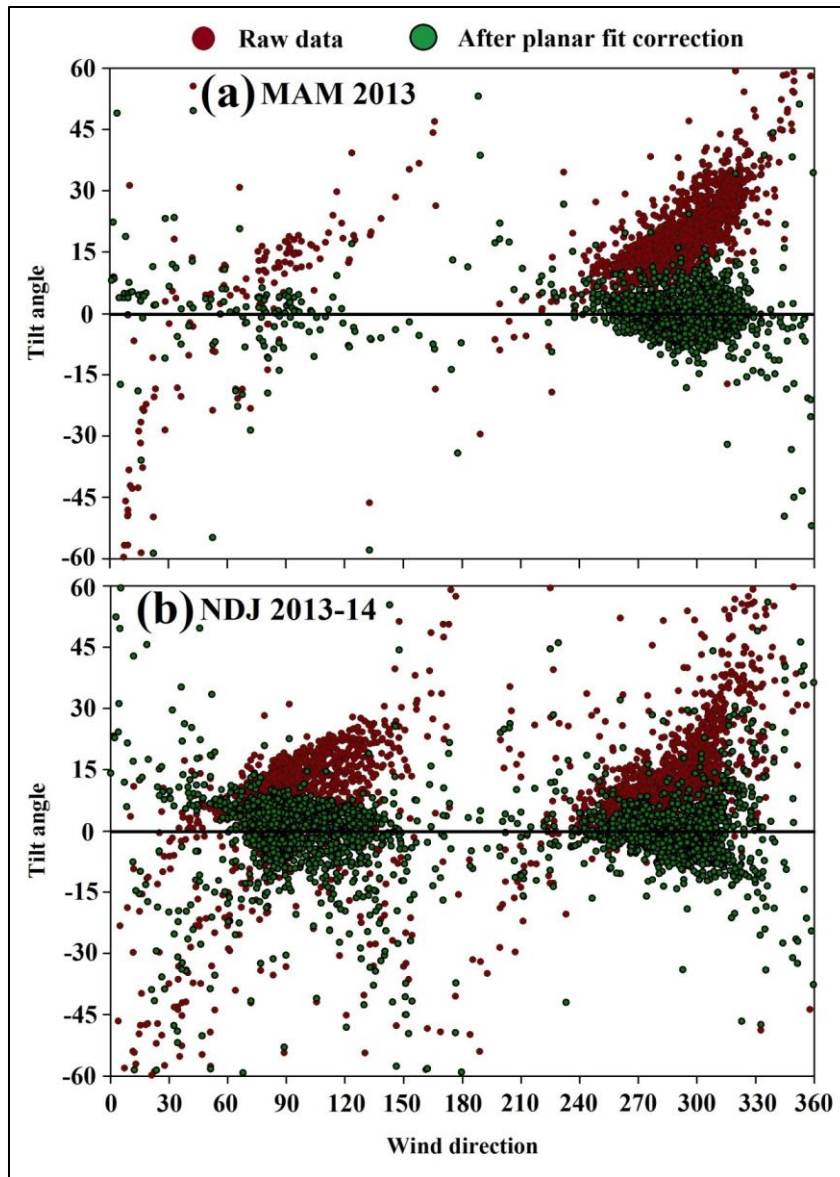


Figure 2.9: Variations in tilt angle ($[\tan^{-1}(\overline{W}/\overline{U})]$) with the tilt angle, before and after planar fit. method correction, for (a) spring and (b) winter season.

2.3 (b) Eddy covariance technique

The eddy covariance method incorporates measurements of vertical fluxes in the surface layer; by instantaneously measuring the properties of eddies as they advect past sensor. The fast response (sampling rate of a few Hz or more) measurements of

wind components: zonal (u), meridional (v) and vertical (w); along with the quantity of interest (such as temperature, moisture, green house gases concentrations, etc.) for which the fluxes in surface layer needs to be quantified form the backbone of a typical eddy-covariance measurement site. An eddy is the turbulence imposed on the mean flow, consisting of irregular swirls of motion. The instantaneous measurement of a quantity x could be split up into the mean \bar{x} and fluctuating (or turbulent) part x' , such that $x = \bar{x} + x'$. The average magnitude of a quantity is computed from raw data time series and then the fluctuating part is obtained by subtracting mean from the instantaneous. In this study, turbulent fluctuations of the u, v, w, and T and the time average of instantaneous covariance such as $u'w'$, $v'w'$ and $w'T'$ are implemented in estimation of fluxes.

In order to understand diurnal variations of parameters being presented in this thesis (Chapter 4), (e.g. winds components, turbulent kinetic energy, fluxes of heat and momentum, etc.) during different representative month of seasons; half hour average parameters of the same time for all available days of a month are utilized to generate a monthly mean over the diurnal (24 hour) cycle. To ensure that all scales of turbulent processes are included in the standard deviation, averaging time of 30 minutes was selected [Krishnan and Kunhikrishnan, 2002; Yusup et al., 2008]. The averaging time was determined by looking at the 25 Hz time series of U, V, W and T and technically on the basis of the empirical method in which we estimated the sensible heat flux for different averaging times and finally selecting the averaging time for which the flux are maximum. The time series of each subset of wind components and temperature were examined for spikes, missing portions of data and such problems were corrected. Spikes were replaced with mean value of neighboring points and missing portions of data were replaced with 'nan'. Further, to justify the conversion from time domain to space domain using Taylor's [1938] frozen turbulence hypothesis (FTH), the turbulence intensity ($TI_i = \sigma_i / M$, where σ denotes standard deviation, $i = u, v, \text{ and } w$ component and M is the averaged wind speed) for each half-hour data subset was determined. Taylor's hypothesis is considered to be

valid when turbulence intensity is small compared to average wind speed [Katul *et al.*, 1997; Pahlow *et al.*, 2001] hence the data subset with $TI_i < 0.5$ were selected for the analysis.

With the focus being mainly on the diurnal evolution of surface-layer characteristics during fair-weather events, days having large-scale cloudiness or convection (assessed on the basis of temporal variations in incoming shortwave flux and weather events recorded in the log-book) are avoided. However, formation of boundary layer clouds (as part of the ABL evolution) is a regular feature during most of the days in spring, and such days are included and subjected to the study. During spring season (March-May period) of 2013, 46 mostly cloud-free days (except for the ABL clouds) are selected for analysis, whereas for the winter season (November 2013 to January 2014), 59 clear-sky days are selected, discarding the days with significant cloudiness or precipitation. In tandem with the daytime surface heating and thermal instability of the surface layer, the turbulent kinetic energy (e) as well as the associated vertical fluxes of momentum and heat, in the surface-layer are expected to undergo systematic diurnal variations. The turbulence intensity is quantified through the magnitudes of e , whereas the exchange of energy and momentum fluxes are quantified through sensible heat flux (H) and vertical momentum flux (τ) respectively.

The fluctuations in the three orthogonal wind components (u , v and w) and virtual temperature measured using the sonic anemometers, after applying the PFM (or SPF) for tilt correction, are utilized for estimating e , τ and H using the eddy correlation method [Kaimal and Finnigan, 1994; Aubinet *et al.*, 2012]. The e , H and τ are computed from:

$$e = 0.5 \left(\overline{u'^2} + \overline{v'^2} + \overline{w'^2} \right), \quad [2.5]$$

$$H = \rho C_p \overline{w' \theta'_v}, \quad [2.6]$$

$$\tau = \rho \sqrt{(\overline{u'w'})^2 + (\overline{v'w'})^2}, \quad [2.7]$$

where u' , v' , w' and θ'_v are the turbulent fluctuations in the orthogonal wind components and virtual potential temperature respectively. These fluctuations at the 27 m height are estimated and averaged for a period of 30 min; the over-bar represents an average over half-hour duration. In the above equations, ρ and C_p represent atmospheric density and isobaric specific heat of air respectively.

Stability of the surface-layer is characterized through the dimensionless length scale z/L , where z is the height of observation (here 12 m and 27 m) and L is the Monin-Obukhov length given by

$$L = -u_*^3 / \left(\kappa \frac{g}{\theta_v} \overline{w'\theta'_v} \right). \quad [2.8]$$

The friction velocity (u_*) and scaling temperature (T_*) are given by:

$$u_* = \sqrt{\tau/\rho}, \quad [2.9]$$

$$T_* = -\frac{(\overline{w'\theta'_v})}{u_*}, \quad [2.10]$$

where κ is the Von-Karman constant (= 0.4), and g is the acceleration due to gravity. Mean winds, temperature, energy and momentum fluxes, stability parameter, and normalized standard deviations of velocity and temperature fluctuations are estimated for each 30 min time bins during the observation period. Monthly mean diurnal variations of the above parameters are obtained by averaging the respective values for the same time bins. Variations of different parameters with stability parameter are obtained by averaging the respective values at constant intervals of z/L .

To meet the third objective of the thesis, RWP measurements are utilized in order to understand the local boundary layer dynamics over the site. Details on RWP instrumentation and its data analysis technique are elaborated in following section.

2.4 Radar Wind Profiler

A radar wind profiler (RWP) is a ground based instrument which transmits electromagnetic energy into the atmosphere and measures the strength and frequency of the backscattered energy. The source of backscatter is the refractive index fluctuations in the atmosphere which provide information on the state of atmosphere, along with the measurement of the mean wind flow (the three components) which is assumed to be associated with these fluctuations. Through sampling of backscatter profiles in the vertical direction and in two tilted planes the profiles of three orthogonal components of wind velocity are determined.



Figure 2.10: Side and top view of the Radar wind profiler operated at ARIES, during GVAX.

During the Ganges Valley Aerosol Experiment (GVAX) campaign (from June 2011 to March 2012) at ARIES, Nainital regular radiosonde launches (comprising of four launches per day, generally at 0000, 0600, 1200 and 1800 UTC), were made, but a clear picture of LBL or ML evolution was not possible, since four radiosonde profiles a day provided only snapshots of the atmosphere. On the other hand, for the first time, a 1290 MHz RWP (Figure 2.10) was operated for wind measurements; which also provides continuous measurements of boundary layer [Angevine *et al.*, 1994; Coulter and Holdridge, 1998] with a finer temporal resolution (15 minutes). Therefore, the RWP is the best possible tool to determine mixed (ML) evolution over the site. The RWP also gives a greater insight into the vertical structure of the

boundary layer in general, which is crucial in understanding dynamic meteorology, pollutant transport and dispersion [Xie *et al.*, 2012]. Studies on ABL dynamics over complex terrain have been made by Reddy *et al.* [2006] and Kalapureddy *et al.* [2007] over a moderately hilly terrain in Gadanki valley region in Southern India. However, no such studies have been made over the Himalayas for the highly contrasting winter and spring seasons. The importance of this study can be understood by the fact that a strong diurnal cycle can appear in the LBL or ML over hilly terrain, under the fair-weather conditions which are suitable for boundary layer evolution [Reddy *et al.*, 2002].

Wind profilers are basically designed to make the continuous measurements of wind components i.e. zonal meridional and vertical, at very fine temporal and spatial resolution in all weather conditions. These profilers generally operate at various frequencies (30-3000MHz) depending upon the science objectives. Such a wind profiler developed by DeTect, Inc., which operates at 1290 MHz was utilized at the observational site. The system is capable of changing the beam pointing angle on a pulse-by-pulse basis for five beam positions, and provided the backscattered signal and the wind profiles between 0.1 and 6 km. The profiler collected a sample every 30 s, completing a cycle of all five beam positions every 150 s. By selecting a beam elevation of 90 degrees, SNR profiles from the vertical beam were only incorporated in this analysis. The SNR data for the vertical beam are available with a resolution of 62.6 m, with the first range bin at 124 m. The specifications of the RWP are enlisted in Table 2.4.

Table 2.4: Specification of RWP utilized during GVAX campaign at ARIES.

Frequency	1290 or 915 MHz
Range Gate	0.06–1 km
Pulse Length	60, 100, 200, 400 m
Spectra/Ave Spectrum	1–100
Pulse/Time Domain Integration	1–1000
Occupied bandwidth @ 1290 MHz	Less than 12.5 MHz @ 400 ns pulse (99% ITU)
Minimum Range	124 m
Maximum Range	3–6 km (15 km for precipitation detection)
Wind speed accuracy (resolution)	± 1.0 (0.01) m/s
Wind direction accuracy (resolution)	± 10 (1) degree
SNR accuracy	1 dB
Antenna	
Type	Electrically steerable micropatch phased-array panels
Gain	~26 dBi
RF beam width	~9 °
Aperture	2.7 m ² @ 1290 MHz, 3.0 m ² @ 915 MHz

2.4 (a) Mixed layer determination technique

For this study, we implemented a new criterion for the SNR that captures nearly systematic feature of LBL evolution with time, since over a mountain peak, the structure of the LBL is not as prominent as that as in high pressure regions or over flat terrains. The estimation method using the RWP has been validated with ML depth from radiosonde profiles (four launches per day). Vaisala DigiCORA III sounding system was used during this campaign which comprises of Vaisala RS92-SGP radiosonde for of pressure, temperature and relative humidity; measurements of wind speed and wind direction were also taken during the flight through a GPS unit on the radiosonde.

The ML height is inferred from the signal-to-noise ratio (SNR) recorded by the RWP. The underlying theory has been discussed by *White et al.* [1991a, b]. The

principal source of scattered signal to RWP is moisture, which is the primary constituent of inhomogeneity in the radio refractive index of the air. These wind profilers basically detect the fluctuations in radio refractive index caused by vertical humidity and temperature gradients. These inhomogeneities are characterized by the refractive index structure parameter C_n^2 [Tatarskii, 1971; Green *et al.*, 1979; Gossard *et al.*, 1982; Gage, 1990; Raghavan, 2003; Singh *et al.*, 2009]. The profiler SNR at a given range is directly proportional to C_n^2 [Ottersten, 1969].

Generally, over a plain site the top of the ML is characterized by increased turbulence, and strong temperature and moisture gradients, which are represented by a peak in the SNR profile, marking the top of the ML [Simpson *et al.*, 2007]. However, this study is carried out over a high altitude site (2 km amsl) and because of the lack of prominent features over the mountainous site the general methods of ML height determination over plains cannot be directly applied. The complex mountainous topography generates its own LBL [e.g. Kossmann *et al.*, 1998], which is different from the PBL in some aspects. One of those is that the SNR profile, instead of exhibiting a peak in the profile, shows a gradual decrease with altitude, as depicted in Figure 2.11; although at another high-altitude research station Kleine Scheidegg [Ketterer *et al.*, 2014] a prominent peak in the SNR profile was always measured in convective state of boundary layer. It may however be noted that the station at Kleine Scheidegg is situated on a mountain pass, whereas the measurements presented in this study were taken over a mountain peak; hence difference in characteristics of LBL could be anticipated due to differences in the topography. One possible explanation for this aspect of the LBL could be the difference in the characteristics of entrainment zone over plains and mountainous terrain, since the entrainment zones basically form between the tops of highest thermal plumes and deepest part of the sinking dry air penetrating through the free troposphere. In contrast to a flat terrain, mountainous or complex terrain may not have that prominent formation of the entrainment zones due to complex topography, as convective mixing over the ridge may be influenced by slope winds and occasional strong horizontal

flows. Therefore, in this study we have considered the region of SNR > 6 decibels (dB) as the LBL over the site and validated this method by comparing the results with those deduced from the vertical profiles of potential temperature and specific humidity from radiosonde (Vaisala RS92-SGP) ascents. In case of RWP SNR profiles showing multiple transitions across the 6 dB threshold, the maximum altitude was selected as the ML height, as shown by the 1000 UTC profile in Figure 2.11.

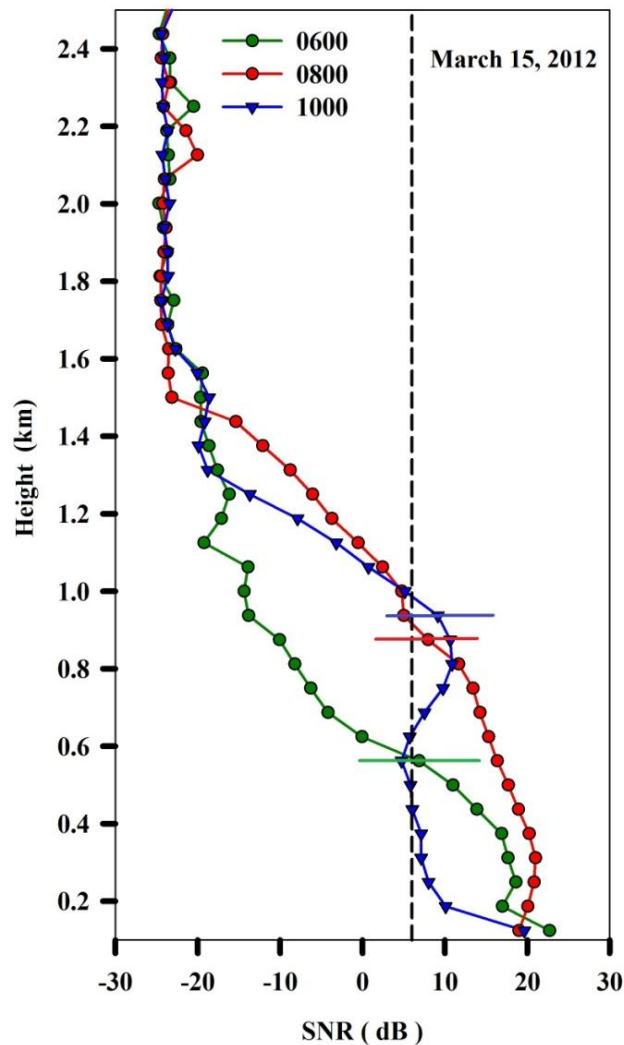


Figure 2.11: The signal-to-noise ratio profiles (15 minute averaged) on March 15, 2012 during the peak sunshine hours. The estimated mixed layer depth for each profile is marked by the horizontal bar.

Although averaging time of 30 minutes is considered for parameters determining the evolution of PBL, but for the LBL study over the site we have considered the averaging time of 15 minutes (for mean SNR profiles) for better statistical average and taking into the mixing timescale, since the LBL is in a much more dynamical state i.e., considering the convective mixing and the topographic effects, as compared to PBL. The contour plots of SNR were also analyzed visually in order to confirm the reliability of the ML depth estimations at the 6 dB threshold. However, the SNR is proportional to refractive index structure parameters, hence can further be subjected to derive reflectivity and the turbulence parameters that again are the tracers of LBL or PBL evolution.

In order to determine the ML height from radiosonde measurements and thus authenticate the 6 dB criterion, the bulk Richardson method, specific humidity gradient (maxima), and virtual potential temperature profiles gradient method were tested; but as expected over a complex terrain, only the specific humidity gradient (maxima) method provided promising results. A detailed correlation analysis was done for ML derived from specific humidity gradient method vs RWP (SNR method) and the maximum correlation ($r^2 = 0.70$; depicted in Figure 2.12) between the two is found to be at the SNR value of 6 dB, for the noon-time and evening (0600 and 1200 UTC) profiles that closely correspond to the convective state of boundary layer over the site. For the analysis, the cases of minimum ML height estimation from RWP (RWP starts measurements beyond 124 m in the vertical) and radiosonde, as well as days of very weak ($< 10 \text{ g kg}^{-1} \text{ km}^{-1}$) gradient in specific humidity profiles were discarded.

The agreement between radiosonde and RWP estimated ML height for midnight and early morning profiles (1800 and 0000 UTC) turns out to be very poor for all of the known methods. The disagreement can be attributed to the topography of the site (a mountain peak) and the drift in the radiosonde, which thus provides measurements of ML height over the adjoining valleys or ridges at nighttime. Since the ML top

follows the topography over mountainous terrain, and the degree to which ML top follows the topography is minimum at noontime and afternoon hours [De Wekker and Kossmann, 2015]. Hence, a higher correlation between radiosonde ML height estimation and RWP derived LBL height is certainly expected to be significant only during the noontime to evening hours.

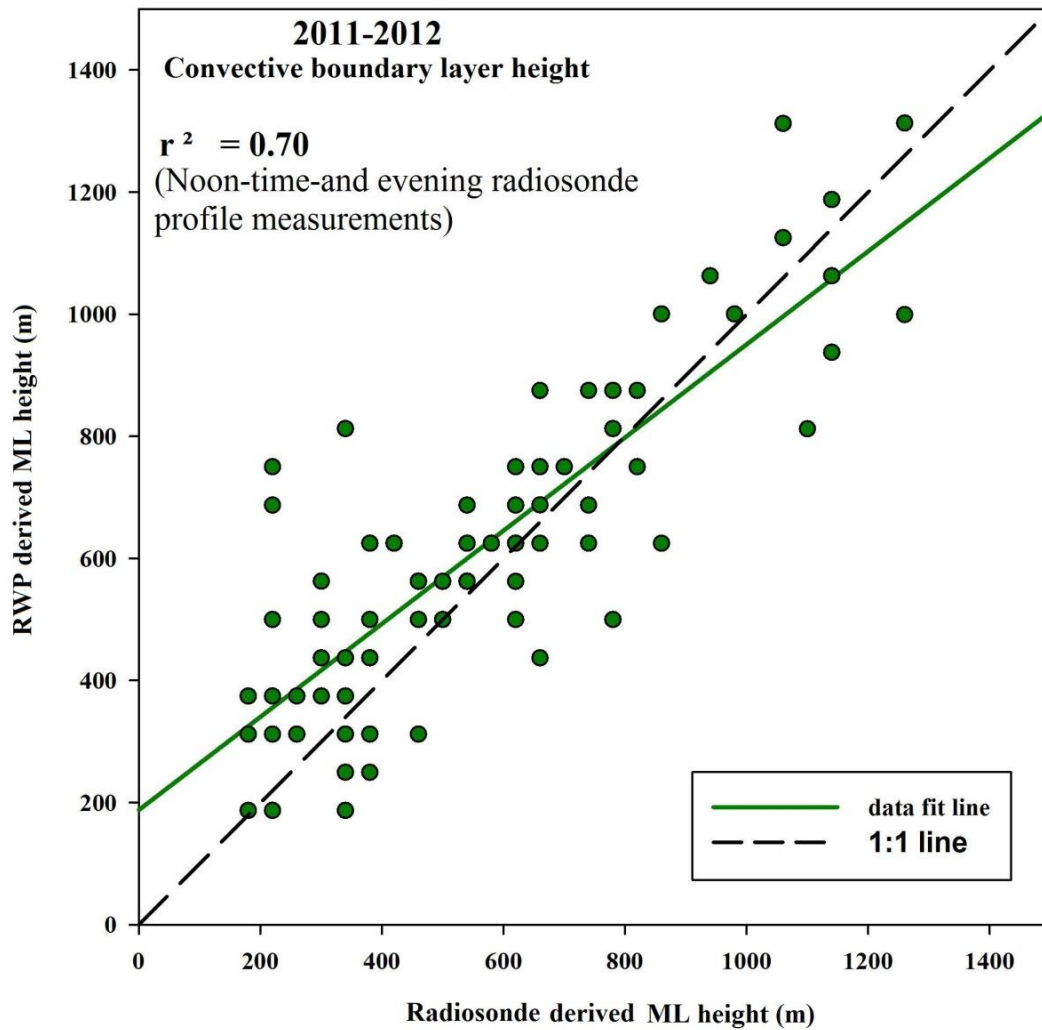


Figure 2.12: Correlation analysis for RWP (ML) vs Radiosonde (ML) at 6 dB.

The vertical profiles of meteorological parameters obtained from the radiosonde ascents are utilized to provide the vertical structure of the atmosphere for comparison

with RWP measurements. The hourly wind speed observations made through a collocated automatic weather station (AWS) over the site are also incorporated to understand the state of the surface layer over the site. Thus with this methodology, the carefully selected 15-min averaged SNR profiles from RWP measurements based on above methodology are utilized to understand the mean diurnal variations of ML depth during months covering the late autumn (November), winter (Dec-Jan-Feb) and early spring (March).

Blank page

Chapter # 3

Variations in aerosol distribution

This chapter elucidates the seasonality in aerosol vertical profiles acquired using LiDAR measurements and compares it with the CALIPSO level-2 data products over central Himalayas. During March 2012 to May 2013 intermittent LiDAR observations were made amounting to a total of 360 hours of LiDAR operation, out of which 57 suitable cases were subjected to further analysis. Aerosol loading in the vertical column was found to be highest with $3.40 \text{ (Mm sr)}^{-1}$ at 3.3 km during the spring and summer seasons (MAMJ-2012), and the lowest with $0.48 \text{ (Mm sr)}^{-1}$ at 2.5 km, during winter season (DJF 2012-13). The aerosol layer reaches to the maximum altitude of 5.6 km in the period of MAMJ-2012 and a minimum at 2.8 km in the winter (DJF). The highest value (124 Mm^{-1}) of extinction coefficient is found at 3.3 km, during MAMJ-2012 and minimum (7 Mm^{-1}) at 2.5 km during the winter season. A comparison of ground based LiDAR observations with the CALIPSO satellite derived aerosol backscatter profiles has been carried out for 37 suitable cases. To determine the LiDAR ratio, AOD measurements from MODIS were used as constrain. The mean percent bias for different seasons are found to be $+18\pm 42\%$, $+22\pm 28\%$, $+32\pm 36\%$ and $+18\pm 51\%$ for MAMJ-2012, SON-2012, DJF-2012-13 and MAM-2013 respectively.

The chapter also presents a case study of each long range transport and convectively driven elevated aerosol layers, observed with LAMP on 22 and 24 March 2012. The seven days back air mass trajectories over three altitude levels for 21, 22, 23, 24, 25, 27, 28 and 29 March 2012 were analyzed to determine the sources of air mass resulting in formation of aerosol layers. The upper levels delineate that the possible origin of the multiple elevated aerosol layers on 22 and 24 March may be transported from far-off regions, such as the dry arid regions of North Africa and Saudi Arabia. To confirm the same, observations were further substantiated with the TERRA satellite yielded aerosol optical depth (555 nm) obtained from the on board instrument Multi-angle Imaging Spectro Radiometer (MISR), which explicitly shows the high value of time averaged columnar aerosol optical depth (AOD) over Saudi Arabia and Red Sea during 18-23 March 2012 and an appreciable decrease during the period 25-29 March 2012, confirming the origin of long range transport. For the first time, such a high altitude aerosol layers (~ 4.5 km) are observed over this region. The lowest aerosol layer observed on 24 and 28 March 2012 in vertical aerosol backscatter profile is attributed to the transport from adjoining regions via boundary layer evolution and associated mixing.

3.1 Aerosol vertical distribution

3.1(a) Inter day variability

Intermittent LiDAR observations were conducted over the site during 89 nights in different seasons and details are given in Table 3.1. A total of 32 nights were cloud contaminated and these observations were excluded from the analysis of aerosol vertical distribution. Hence, for this study a total of 57 nights of LiDAR observations are analyzed and presented, with a seasonal aggregate of 17, 12, 11, and 17 nights in MAMJ-2012, SON-2012, DJF-2012-13 and MAM-2013 respectively. Due to the presence of low altitude thick layer of monsoon clouds over the site the system is not usually operated during JJA; however, at occasions under clear sky conditions in the month of June and July, 3 and 1 observation were taken respectively. Hence, these 4 days were combined with spring season forming one group of MAMJ months.

Table 3.1: Number of observations in a month and total hours of LiDAR operation at Manora Peak, Nainital

Months	Observations	Duration(hours)
March-2012	9	30.83
April-2012	8	35.93
May-2012	7	21.17
June-2012	4	8.87
July2012	1	2.67
August-2012	0	0
September-2012	3	9.17
October-2012	5	17.03
November-2012	7	29.83
December-2012	10	51.98
January-2013	7	38.15
Feburary-2013	6	28.83
March-2013	7	29.4
April-2013	8	30.13
May-2013	7	26.38

Figure 3.1 depicts the inter-day variability over different seasons during the period of study. In MAMJ-2012 prominent inter-day variability is seen up to 3.5 km

with aerosol backscatter of 3.0 (Mm sr)^{-1} in March and April though for the month of May backscatter is quite high and above $10.0 \text{ (Mm sr)}^{-1}$. In June and July the backscatter varies from 7.0 (Mm sr)^{-1} before the arrival of monsoon at site to 2.3 (Mm sr)^{-1} after the onset of monsoon respectively. During the autumn season the inter day variations are quite suppressed with all the vertical profiles showing backscatter up to 1.5 (Mm sr)^{-1} from ground to 3 km, except for the case of November 7, 2012 under prevailing hazy atmosphere over the site, leading to higher backscatter up to 5.6 (Mm sr)^{-1} .

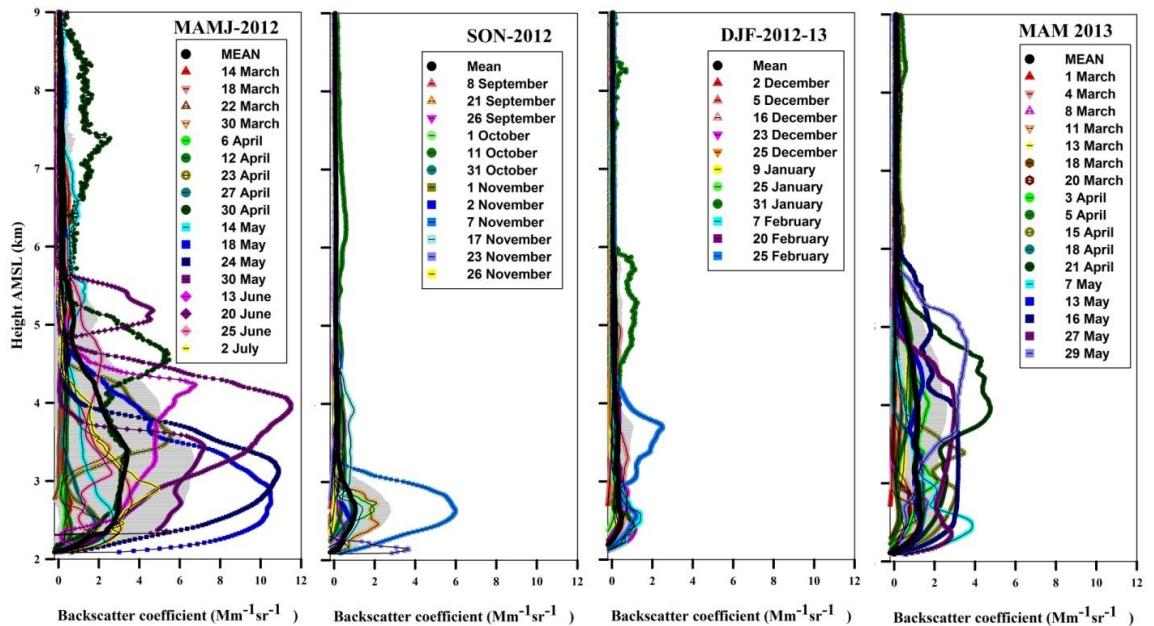


Figure 3.1: Day-to-day variability in the aerosol vertical profiles of back scatter coefficient, during different seasons, 17 observations in spring and summer (MAMJ), 12 in Autumn (SON), 11 in winter (DJF) and 17 in spring season of 2013(MAM) over more than a year of observation.

The winter season displays least variability from day-to-day, with most of the profiles having backscatter coefficient below 1.0 (Mm sr)^{-1} except for 25 February which is nearly the beginning of the spring season when the aerosol layer at 4 km is observed with backscatter of 2.2 (Mm sr)^{-1} . The spring season of the year 2013 shows

reasonably lower aerosol loading in the atmosphere and subdued inter day variability in comparison to the spring season of the year 2012. The lower aerosol loading could be explained by the fact that, during MAM 2013 the region witnessed many rainfall events about a period of every 10-day that occurred due to western disturbances and prevented the buildup of aerosol loading in the vertical column of free troposphere. The maximum backscatter of 4.7 (Mm sr)^{-1} is observed on 21 April 2013 at 4 km in the spring season. Significant loading is seen in the column up to 5.5 km during spring of 2012 and 2013 as well, which could be ascribed to the eastward transport of west Asian aerosols, and increased convective mixing in the nearby lower plains adjacent to the site.

3.1 (b) Back air Trajectory analysis

In order to attribute the possible sources of aerosol at different altitudes of vertical profile we analyzed 7-day iso-sigma back air trajectory simulated using the Hybrid Single Particle Lagrangian Integrated Trajectory (HYSPLIT) model [Draxler and Rolph, 2003] for different seasons over the period of March 2012 to May 2013. NCEP reanalysis data ($2.5^\circ \times 2.5^\circ$ spatial and 6 hours temporal resolution) have been utilized as input for the model. Figure 3.2 and 3.3 show the air mass trajectory at 2.5 km and 3.5 km AMSL respectively, during different seasons corresponding to the days when LiDAR observations were made. The levels were selected based on the variability in the vertical profiles of aerosol as displayed in Figure 3.1. The starting closest time for trajectories is taken as 1200 and 1800 UTC, since the LiDAR is usually operated from late evening to midnight (1800-0000 Hrs local time).

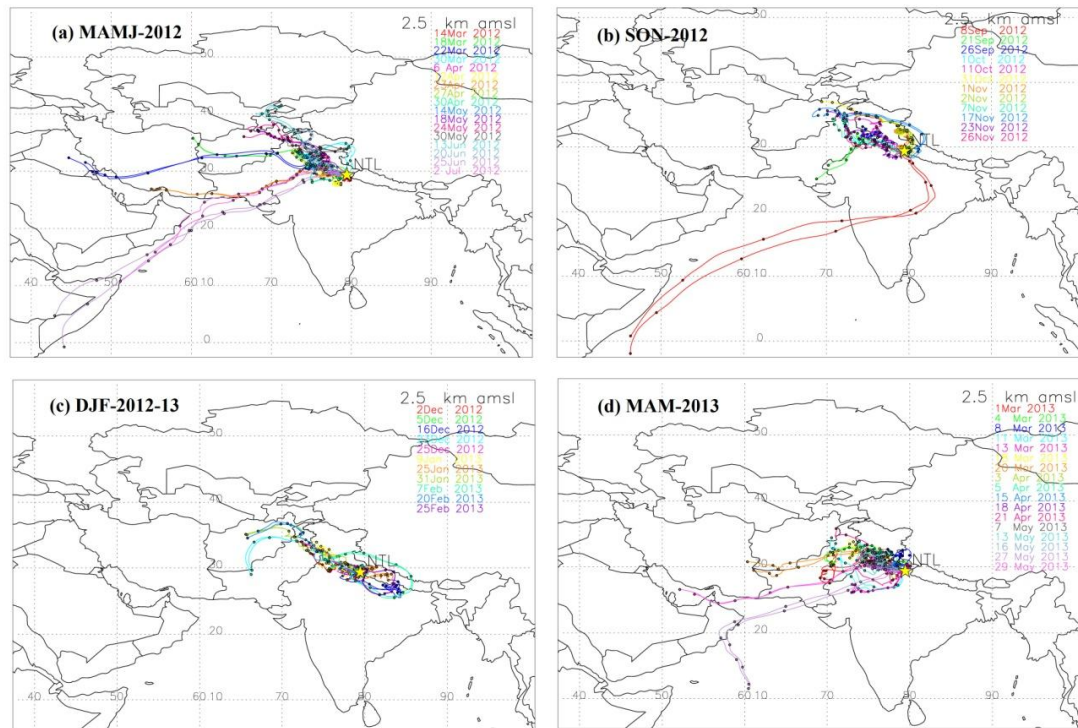


Figure 3.2: HYSPLIT model simulated 7-days back air trajectories originating at 2.5 km AMSL over the site, each starting on 1200 Hrs and 1800 Hrs UTC represented by two concurring lines. Each dot along the trajectory corresponds to one day backward-position of air mass followed by the previous day.

The air masses arriving at the site originate from west (Saudi Arabia, Iran and Pakistan) and northwest regions (Turkmenistan, Afghanistan and northern Pakistan) with smaller spread in trajectories at 2.5 km in the spring season. In the Figures 3.2 and 3.3, it is clear that mesoscale flow is originating over semi-arid regions such as Iran and Saudi Arabia, which in general suffer relatively high temperatures in spring and summer, and the lower atmosphere is being driven with strong convective lifting of aerosol in this region. In the spring season of 2012, prevailing winds at 2.5 km are either westerly or near westerly indicating that in the absence of local source of aerosol and weak convection, the loading over the site is caused by the transport from distant origins, which have been convectively lifted to the altitude range of 2.5-3.5 km in the vertical.

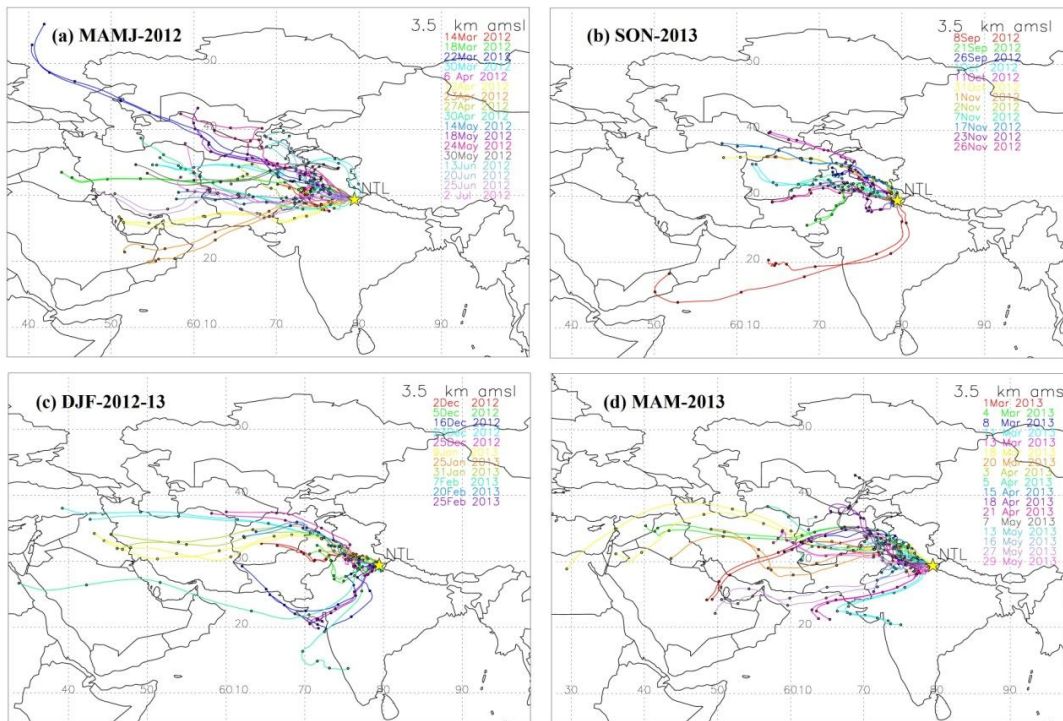


Figure 3.3: Same as figure 3, but with the trajectories originating at an altitude of 3.5 km AMSL over the site.

In contrast to spring 2012, in the bottom right panel of Figure 3.2, on the days 1, 13 March; 18, 21 April; and 29 May it can be noticed that the airflow is from the nearby western continental parts and contributing to the aerosol loading in the vertical column, but quite low as compared to the previous year. It confirms that the local weak convection is least responsible for the higher AOD values in spring and summer.

Figure 3.3 depicts the trajectory analysis at 3.5 km, again confirming the significant contribution of long range transport through westerly and near westerly flows and extending over the entire column of air over the site.

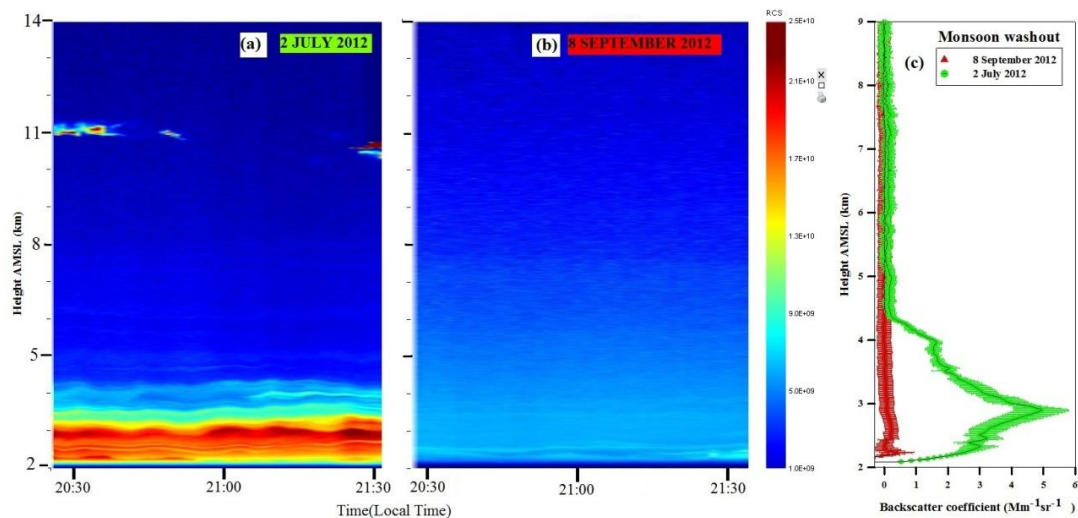


Figure 3.4: (a) Aerosol loading in the vertical column on 2 July 2012, just before the arrival of monsoon, visible up to about 4 km with a decreasing intensity after about 3 km. (b) Range-Time-Intensity plot for a pristine atmosphere observed on 8 September 2012, after the washout of aerosols by monsoon rains, (c) The aerosol backscatter profile estimated for these two cases of (with and without) aerosol loading in the lower free troposphere, the highest value observed at about 3 km AMSL.

A south-easterly flow from Bay of Bengal is observed on 8 September, bringing in cleaner oceanic air mass to the site after washout of aerosol by monsoon as shown in Figure 3.4. In the autumn season the flow changes to north westerly again at both the altitudes but remains more confined to regions of Punjab and Haryana. During winter the air mass circulates over the northern and central Indian regions with general flow being north-westerly only along foothills of the Himalayas, and the wind pattern being more confined at 2.5 km as compared to the wind flow at 3.5 km.

3.1 (c) Seasonal variations

The backscatter profiles for aerosol show strong seasonality in the vertical distribution of aerosol up to 4 km. The spring and pre-monsoon season witness forest fires and strong convection, giving rise to aerosol loading in the vertical column, however, few thunderstorm activities at the same time may lead to wash out of

aerosol. The backscatter coefficient during this period is found to have the maximum values of 3.4 ± 2.6 (Mm sr^{-1}) at 3.5 km, including some cases of elevated aerosol layer 0.5 ± 0.3 (Mm sr^{-1}) up to 8 km, as shown in Figure 3.5 (MAMJ-2012 panel).

The large horizontal bars (envelope around the thick mean line representing the standard deviation of the measurement) depict the large variability in backscatter profiles, basically due to dust storms observed over the site [Srivastava *et al.*, 2011; Solanki *et al.*, 2013] during the spring and post monsoon season when the backscatter values are 2-3 times the normal aerosol backscatter. Due to intense solar radiation and convection the planetary boundary layer rises above the altitude of site during daytime in the spring and summer seasons and thus the local sources of aerosol also contribute to aerosol loading in the lower part vertical column (below 3 km) along with long range transport from far off dry regions leading to aerosol loading at higher altitudes (above 4 km) over the site as compared to the other seasons.

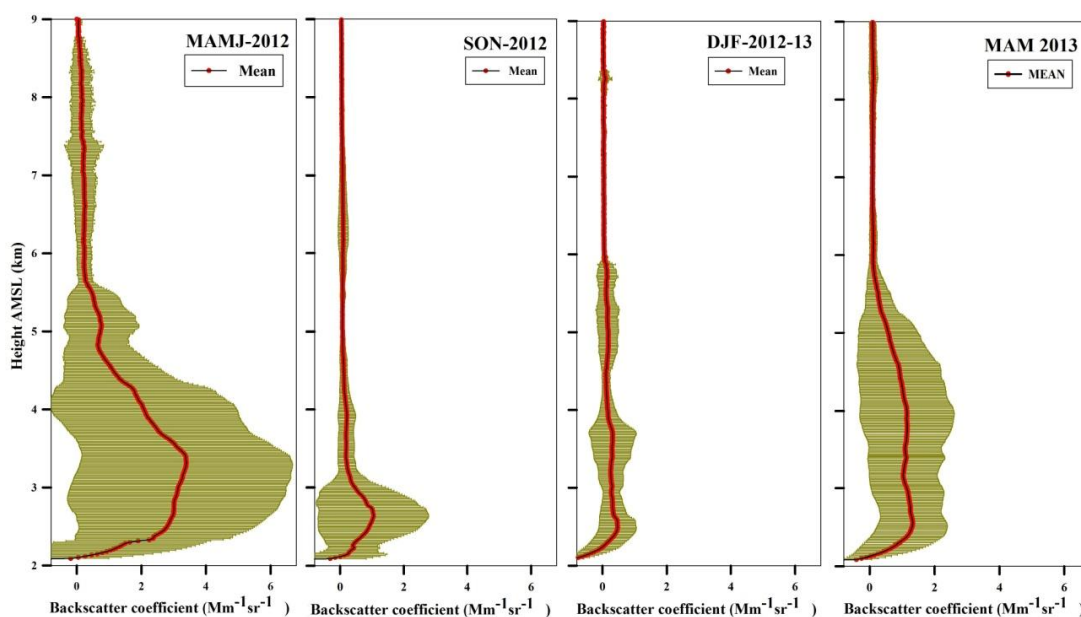


Figure 3.5: Seasonal variability of aerosol backscatter profiles over Nainital during 2012-13, the seasonal mean is the thick red-line and sheath over horizontal bars represents the standard deviation at each altitude.

The autumn season shows drastic decrease in the aerosol backscatter values to 1.0 ± 0.8 (Mm sr^{-1}) at 2.67 km due to washout of aerosol by heavy rains in the monsoon period. Also, during the autumn and winter season cold flows with low wind speed especially come from high Himalayan mountain range along the foot hills of Himalayan belt [Gautam *et al.*, 2007] which lead to formation of stable layer over the region, thus trapping the aerosol in the plains adjacent to the site. During winter months due to weak solar radiation and low temperatures the evolution of atmospheric boundary layer (ABL) in nearby plains is suppressed down to 900 m AMSL, thus the transport of aerosol to the mountain peak is inhibited and site is free of all local contamination which is evident from the lower values of backscatter coefficient 0.48 ± 0.46 (Mm sr^{-1}) at 2.5 km, and 0.33 ± 0.31 (Mm sr^{-1}) at 3.6 km, representing the pristine air quality over the site and free tropospheric conditions. A similar seasonal pattern in backscatter coefficient at altitudes above 2 km has been reported by Mishra and Shibata [2012] over the IGP.

The aerosol layer height also demonstrates strong seasonal behavior. Considering the altitude where the aerosol backscatter is less than 0.3 (Mm sr^{-1}) as top of the aerosol layer, the aerosol layer height is ascertained to be 5.6 km in spring and pre-monsoon season (MAMJ 2012), 3.2 km in autumn (SON 2012), 2.8 km in winter (DJF 2012-13) and 5.3 km the spring season (MAM) of the year 2013. Thus, the aerosol loading can take place up to 5.6 km over the central Himalayas in spring and summer seasons except in particular case of long range transport when aerosols reach up to 7 km. The aerosol layer heights at our site are comparable to the results of Komppula *et al.* [2012] reported near Delhi.

The seasonal variability of aerosol extinction coefficient at 532 nm is shown in Figure 3.6, which indicates that for a constant LR, the vertical profile of extinction coefficient follows similar pattern as the backscatter profile. Maximum extinction of 124 ± 138 Mm^{-1} at 3.2 km is observed in the spring and pre monsoon season (MAMJ-2012) and a secondary layer of aerosol at 5.1 km with extinction of 25 ± 40 Mm^{-1} . However, extinction in the autumn season is considerably reduced to a value of

$14 \pm 19 \text{ Mm}^{-1}$ at 2.6 km, and is lowest ($7 \pm 8 \text{ Mm}^{-1}$ at 2.5 km) in winters. The extinction coefficient profile in spring season (MAM) of 2013 shows a considerable reduction as compared to MAMJ-2012, with maximum of $45 \pm 41 \text{ Mm}^{-1}$ at 2.54 km. The values of aerosol extinction over the site are close to those reported by *Misra et al.* [2012], *Kompulla et al.* [2012] during the spring and pre monsoon season, but much lower in the autumn and winter season. *Ramana et al.* [2004] reported extinction of 200 Mm^{-1} at 3.0 km in February 2003 at the Kathmandu site (1300 m), which is much higher than our results. Though to make a comparison between our site (1951 m), Kanpur (125 m) and Delhi (237 m) would be inappropriate because of the difference in altitude, but still comparison of profiles at above 2 km is reasonable. By integrating the seasonal mean extinction profiles (ground to 9 km) of LiDAR, the AOD comes out to be 0.259, 0.019, 0.014 and 0.124 during MAMJ-2012, SON-2012 DJF-2012 and MAM-2013 respectively. The extinction profiles were constrained using the MODIS-AOD; hence these values are a direct function of the MODIS measurements.

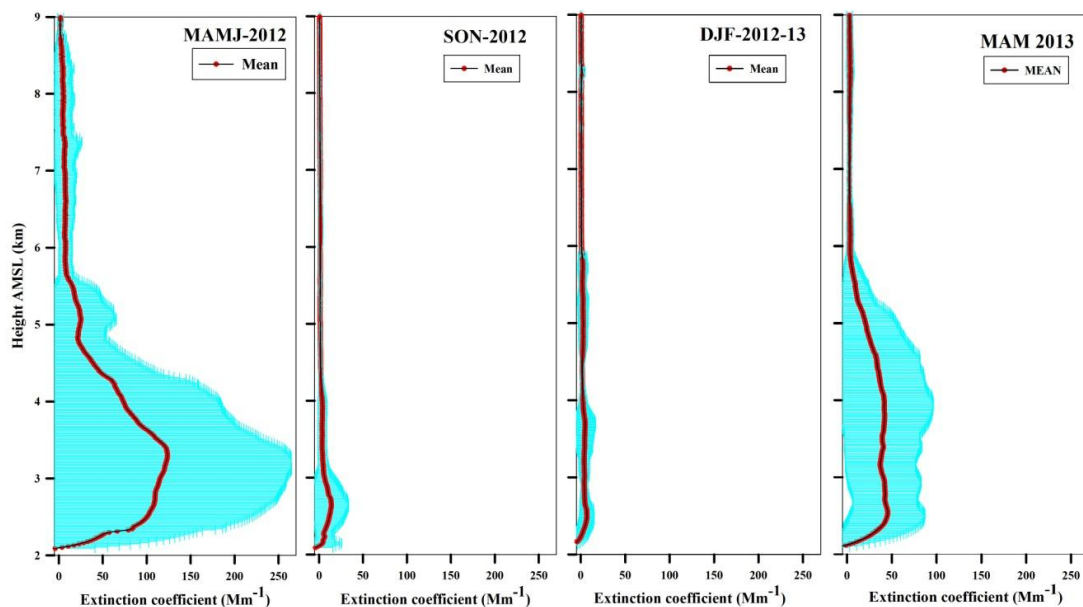


Figure 3.6: Seasonal variability of aerosol extinction profiles which is the product of Lidar ratio and aerosol back scatter, over the period under study. Mean and envelope are similar to that in Figure 3.5.

3.2 Comparison of LiDAR measurements with CALIPSO satellite retrievals

A comparison of the satellite (CALIPSO) retrieved vertical profiles over the central Himalayas with ground based measurement is being studied, as satellite observations provide time constrained observations of aerosol vertical distributions but ground based LiDAR can give information on the evolution of the distribution over a location. Thus, with the aid of a composite study on satellite, ground based observations and transport models; one can extricate the temporal, spatial distribution and the evolution of aerosol on a regional to global scale [Ansamann, 2006]. Studies on comparison of CALIPSO data with ground based observations have been reported in several research articles [Mamouri *et al.*, 2009, Pappalardo *et al.*, 2010, Tesche *et al.*, 2013) indicating the utility and importance of the satellite observations and comparison with ground truth at different locations over the globe. Vertical aerosol distribution with CALIPSO measurements over Delhi has been studied by *Srivastava et al.* [2012b] during winter and summer season. However, due to sparsity of the ground-based observations, such comparison with the satellite data is still severely lacking over Himalayan region. This comparison study over such a complex terrain would enable the CALIPSO satellite retrievals to be used with greater confidence over the Himalayas and the adjoining IGP region.

3.2 (a) CALIPSO data processing

The Cloud-Aerosol Lidar and Infrared Pathfinder Satellite Observations (CALIPSO) satellite was launched in April 2006; and since June 2006 it started providing continuous and vertically resolved observations of global atmospheric aerosol distribution. A complete overview of the CALIPSO mission and CALIOP (Cloud Aerosol Lidar with Orthogonal Polarization) data products is given by *Winker et al.* [2009]. CALIPSO Level-2 version 3.02 (March-2012 to February-2013) and version 3.30 (March-2013 to May-2013) profile products are used for comparison presented in this chapter. The third release of the CALIPSO data products features a comprehensive restructuring, expansion and significant enhancement to the LiDAR

Level-2 cloud and aerosol profile products, numerous quality flags and the implementation of an improved calibration technique for the LiDAR Level-1 532 nm daytime calibration. The version 3 products have a vertical resolution of 60 m up to 20.2 km and horizontal resolution of 5 km providing better screening of clouds using improved cloud-aerosol discrimination algorithm (CAD) [Liu *et al.*, 2010]. Comparison of the CALIPSO data with the LiDAR was made after applying various data quality screening flags such as CAD (-100 to -30), aerosol layer fraction (5 to 30), extinction quality check flag either 0 or 1. A quality flag is assigned to each observed data point in the CALIPSO data file, so as not to modify the original observed data point, and still be able to assess its quality.

Over the period of study, a total number of 52 overpasses occurred within a spatial distance of less than 220 km and a temporal difference of less than 18 Hrs between our LiDAR and satellite overpass. However, previous studies [Tesche *et al.*, 2013] have considered spatial distances of 500 km for comparison purpose. According to Anderson *et al.* (2003), in PBL a 12 Hours of time difference and 120 km of spatial difference is too far away to expect the PBL aerosol distribution to be similar, but since this comparison is being made 2 km AMSL, which is well above the PBL height, hence, assuming that we are comparing the free tropospheric column of the atmosphere, a high correlation can still be expected.

Out of 52 overpasses of satellite, 37 qualified for comparison, remaining 15 cases were excluded due to unavailability of data and presence of clouds over our LiDAR site. In order to compare an individual observation, all profiles within the horizontal separation of 220 km from LiDAR site, were averaged and interpolated to the vertical resolution of 15 m, equal to that of our LiDAR. Details of 37 cases subjected to the comparison are listed in Table 3.2.

Table 3.2: Days of LiDAR observations and CALIPSO overpasses used for comparison

S. No.	LiDAR observations date	CALIPSO OVERPASS DETAILS	
		Delay (Hours: Minutes)	Separation (km)
1	22-Mar-12	13:40	197
2	24-Mar-12	02:00	109
3	30-Mar-12	07:24	36
4	6-Apr-12	05:42	133
5	23-Apr-12	14:48	196
6	27-Apr-12	02:41	218
7	30-Apr-12	15:31	32
8	24-May-12	06:05	130
9	13-Jun-12	18:00	106
10	25-Jun-12	06:18	131
11	21-Sep-12	14:18	33
12	26-Sep-12	16:45	52
13	1-Oct-12	05:42	196
14	11-Oct-12	04:29	45
15	31-Oct-12	06:06	137
16	1-Nov-12	07:37	196
17	2-Nov-12	06:02	196
18	17-Nov-12	17:54	196
19	2-Dec-12	04:30	134
20	5-Dec-12	03:55	110
21	23-Dec-12	04:29	219
22	25-Jan-13	17:06	217
23	31-Jan-13	00:00	50
24	7-Feb-13	01:02	122
25	20-Feb-13	01:52	147
26	25-Feb-13	04:09	208
27	1-Mar-13	05:16	18
28	4-Mar-13	02:26	43
29	8-Mar-13	05:08	145
30	11-Mar-13	03:43	119
31	13-Mar-13	02:42	214
32	5-Apr-13	02:53	48
33	18-Apr-13	05:50	28
34	21-Apr-13	03:17	50
35	7-May-13	03:29	59
36	13-May-13	06:01	201
37	29-May-13	06:45	199

3.2 (b) CALIPSO versus LiDAR

We have carried out comparison of aerosol backscatter profiles measured by CALIPSO over the central Himalayas with the ground based LiDAR measurements made over Manora Peak. For the comparison cases, we have used the same vertical profile of temperature and pressure as used by the CALIPSO algorithm, so as to remove the molecular backscatter differences.

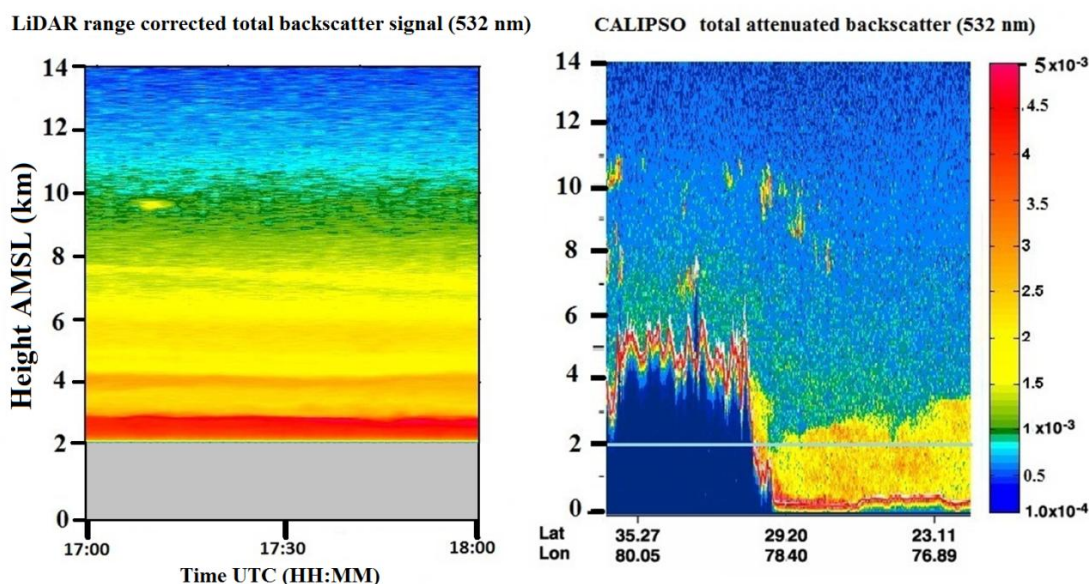


Figure 3.7: Range-Time-Intensity plot for the comparison of range corrected LiDAR-backscatter (integration time 120 s) and CALIPSO-total attenuated backscatter (version 3.02), on 24 Mar 2012. The signal intensity observed with both Lidar and CALIPSO is in the same order of magnitude.

Figure 3.7 shows time series plot of ground based LiDAR range corrected signal (left panel) and CALIPSO derived total attenuated backscatter (right panel), for the satellite overpass on 24 March 2012 at a separation of 109 km from the LiDAR site and the time difference of 2 hours. In the CALIPSO time series plot a dense aerosol layer is evidently visible and extending up to about 2 km in the adjoining IGP region which is considered to be originating with the evolution of convective boundary layer. But as we approach northward, steeply rising Himalayan range acts as a barrier

to the aerosol layer and confining it to the foothills. Here, it is important to notice that the regional mixing and transport of aerosol may also contribute to some extent to the aerosol loading over the site, through the evolution of PBL beyond 2 km in the nearby plain regions at lower altitudes and merging with the LBL; but major contribution is through from long range transport. Also, it is evident from Figure 3.7 that boundary layer variations could be influenced by complex topography, however, these variations are only influencing the lower part of the free troposphere (1-2 km above ground level over Himalayas) and no significant variability is seen on horizontal scales above these altitudes.

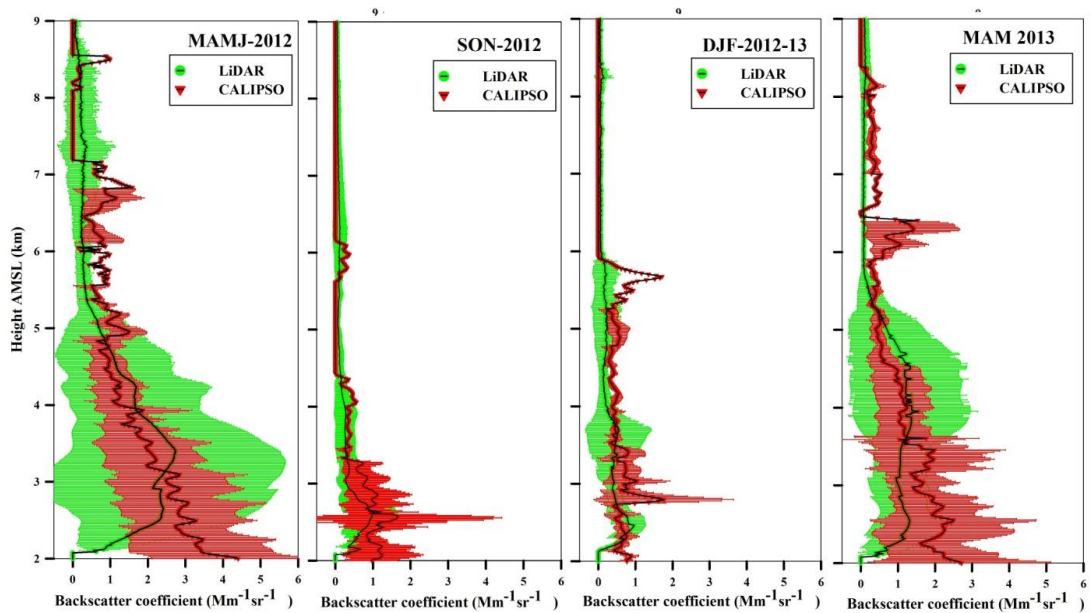


Figure 3.8: Comparison of seasonal mean aerosol backscatter profiles acquired with CALIPSO and LiDAR over different seasons. The two measurements are in reasonably good agreement above 3 km, whereas below 2.5 km in spring and summer, significant mismatch is observed.

Figure 3.8 provides the comparison of ground based LiDAR and CALIPSO satellite measured vertical profiles of aerosol backscatter coefficient. Pre-defined LR are used in the CALIPSO level 2 retrieval algorithm to obtain backscatter coefficient profile of aerosol from the level 1 attenuated backscatter signals shown in Figure 3.7.

The averaging of 10 profiles in MAMJ-2012, 8 in SON-2012, 8 in DJF-2012-13 and 11 in MAM-2013 is performed for comparison. During the spring season the profiles show strong variability ($>1\text{-}\sigma$) in the lower troposphere ($< 3.5\text{km}$) mainly because of being a dynamically active region. In order to quantify the comparison, we have calculated the percentage bias [Mamouri *et al.*, 2009] between LiDAR and CALIPSO backscatter profiles using the following formulation:

$$\text{bias}(h) = \frac{\beta_{\text{CALIPSO}}(h) - \beta_{\text{LiDAR}}(h)}{\beta_{\text{CALIPSO}}(h)} \times 100 \quad [3.1]$$

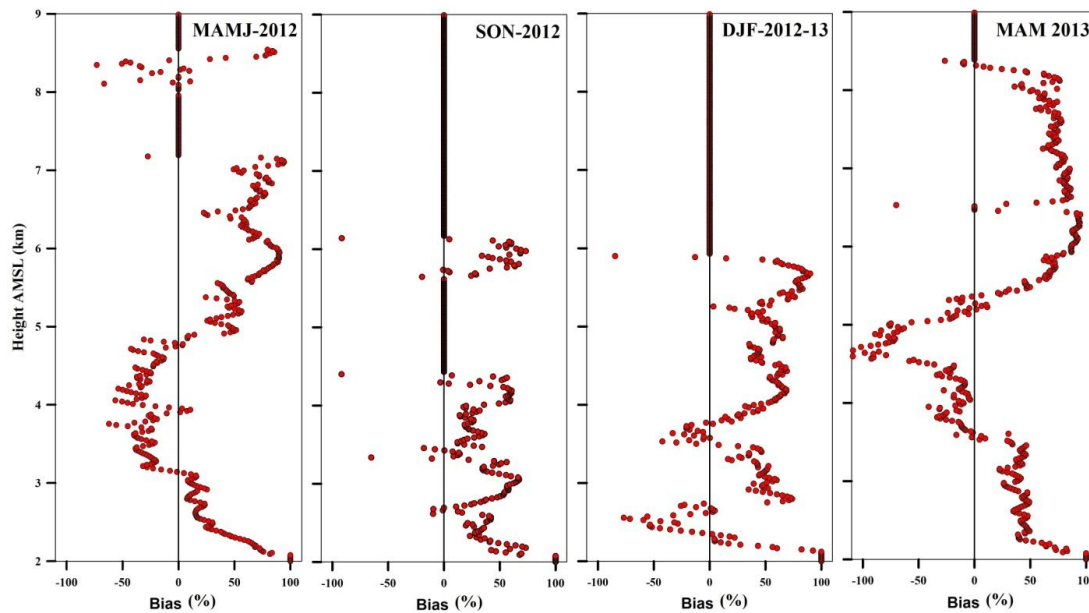


Figure 3.9: Percent Biases between CALIPSO and LiDAR over different seasons. Bias is found to range from -50 to +90 during spring and summer (MAMJ), -10 to +60 in autumn (SON), -75 to +90 in winter (DJF), and -100 to 90 in spring of 2013 (MAM).

The directly calculated percent bias during different seasons is shown by Figure 3.9. Further, the mean biases are calculated for the height region between 2 and 6.5 km AMSL. The CALIPSO overpass for 31 January 2013 occurred at 50 km from the site with exact temporal match with ground based observation, which was

individually analyzed and the mean bias was found to be $+15\pm 63\%$. For spring and pre-monsoon season (MAMJ-2012) satellite overestimates the backscatter coefficient by $+18\pm 42\%$. The comparison shows that the satellite significantly overestimates ($+53\%$) the backscatter values over the altitude region from 2 to 2.5 km which is expected, otherwise comparisons are reasonably good with the ground based measurement for heights above 2.5 km, with an overestimation of $+16\%$ from 2.5 to 3.1 km and the underestimation of -18% from 3.2 to 4.8 km. For the autumn season the satellite retrievals overestimate the ground measurement all throughout the vertical profile, with an average mean bias of $+22\pm 28\%$. During the winter period CALIPSO overestimates the aerosol backscatter coefficient almost throughout the vertical profile, with a mean bias of $+32\pm 36\%$. The mean bias for MAM-2012 is however $+0\pm 35\%$, with an overestimation of $+15\%$ from 2.1 to 3.1 km and the underestimation of -18% from 3.2 to 4.8 km. A similar mean bias of $+18\pm 51\%$ is found for the spring season of the year 2013 (MAM-2013 panel). When biases of different altitudes for MAM-2013 are considered they turn out to be higher, when compared to MAM-2012, with overestimation of $+39\%$ from 2.3 to 3.5 km and underestimation of -33% from 3.6 to 5.4 km. The seasonal mean biases are in reasonable agreement with such efforts over other parts of the world [*Mamouri et al.*, 2009; *Pappalardo et al.*, 2010].

3.3 Elevated aerosol layer: A case study

The formation of elevated aerosol layers in the atmosphere has great significance in the radiative forcing applications [*Gadhvi and Jayaraman*, 2006; *Niranjan et al.*, 2007]. In this context, LiDAR observations are very useful as they potentially provide the vertical distribution on the aerosol optical properties. Such elevated aerosol layers are found in northern India, particularly during the winter season due to dry convective lifting of pollutants at distant sources and subsequent horizontal upper air long range transport [*Ramana et al.*, 2004]. However, at Manora Peak, Nainital, by and large these layers are observed in all months during the spring season of the year,

but here, only two cases, of multiple aerosol layers as observed with LAMP system, are discussed.

LiDAR profiles show multiple elevated layers present over Nainital as a result of local meteorology and mostly upper level long range transport of aerosols originating from arid and semi-arid regions of the western part of the Indian subcontinent and other parts of the countries to the west of India. Aerosol layers found above the boundary layer could have been transported several thousands of kilometers without significant removal and as a consequence can contribute significantly to the columnar aerosol optical depth at times, more than what local boundary layer does. Elevated aerosol layer has also been observed during the month of June 2006 [Srivastava *et al.*, 2011] at an altitude of 1300 m. On 22 March 2012, elevated aerosol layers were observed at altitude of about 3.5 and 4.5 m for the first time over this region, indicating that a strong surface forcing have lifted dry air masses to the higher altitudes, followed by a horizontal transport to the site under observation.

A total number of 51 data sets were analyzed for this study, nine data sets were found to have the signature of elevated aerosol layers particularly in spring. Figure 3.10 (left panel) shows the typical vertical profile of range-time-intensity (RTI) measured during 1900 hrs IST to about mid night on 22 March 2012. A shallow intensity layer at about 4.5 km, very strong backscattering signals at about 3.5 km and around 1 km are observed. The aerosol backscatter coefficient derived from the signal intensity is further averaged to get the vertical profile up to 6 km. Signature of a shallow layer of aerosols is evident in RTI plot, this shallow layer gradually settles down at around 2230 hrs IST and mingles to the denser lower aerosol layer at about 3 km. The lowest aerosol layer is detected at about 1 km, which also settles down around mid night and becomes a part of the stable layer or localized nocturnal boundary layer.

Average vertical profile of backscatter coefficient is given in Figure 3.10 (right panel), where three peaks at the corresponding RTI heights is clearly seen, however, the peak at 3 km is prominent and an indicative of denser elevated aerosol layer. The

back air mass trajectory analysis using the HYbrid Single Particle Lagrangian Integrated Trajectory [Draxler and Rolph, 2003] (HYSPLIT) model reveals the source of aerosols transported from distant regions. Figure 3.11 depicts the seven days back trajectories of air mass, at three altitudes 4.5 and 3 km, for 21 (one day prior), 22 (day of observation) and 23 (one day later) March 2012. The trajectory analysis reveals that the air masses at 4.5 km are coming near westerly and dust seems to be originating from Europe and Saudi Arabian regions; whereas at 3 km, air masses are originating from Europe and extreme North African regions with northwesterly winds that turn westerly as it passes over Iran, Afghanistan and northern Pakistan regions.

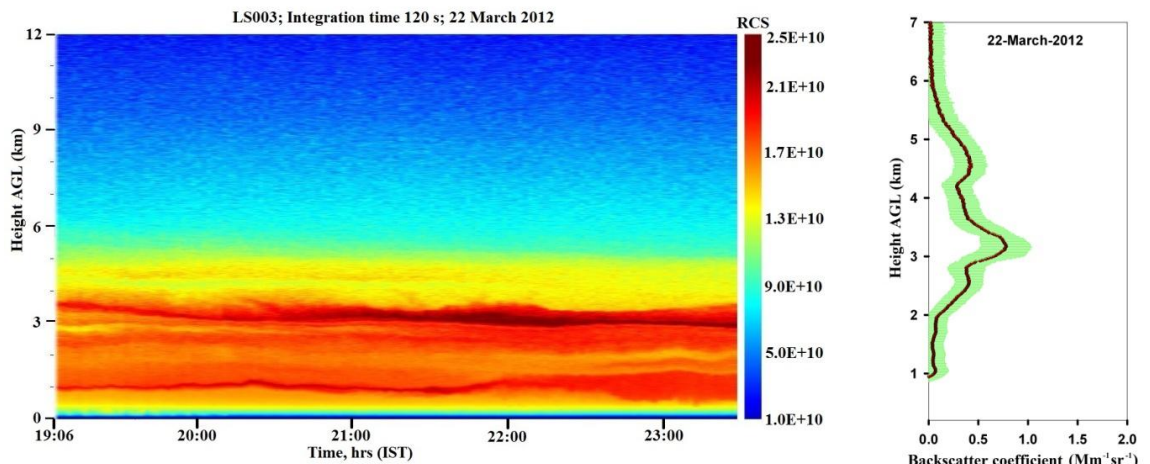


Figure 3.10: Altitude vs time contour plots of range corrected photon counts on 22 March 2012 (left panel) (b) Aerosol backscatter profile (right panel) on 22 March 2012 (Standard deviation shown in horizontal error bars).

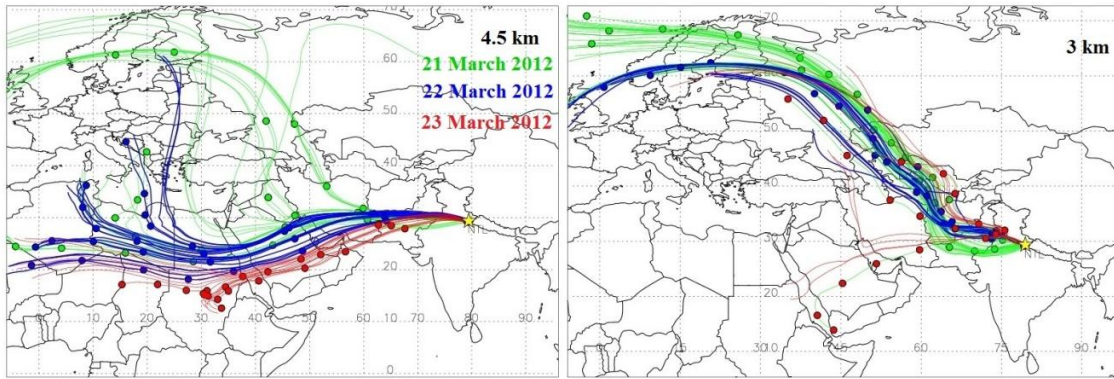


Figure 3.11: HYSPLIT seven days back trajectories of air mass analyzed for 21, 22 and 23 March 2012 at three different altitudes: (left panel) 4.5 km and (right panel) 3 km.

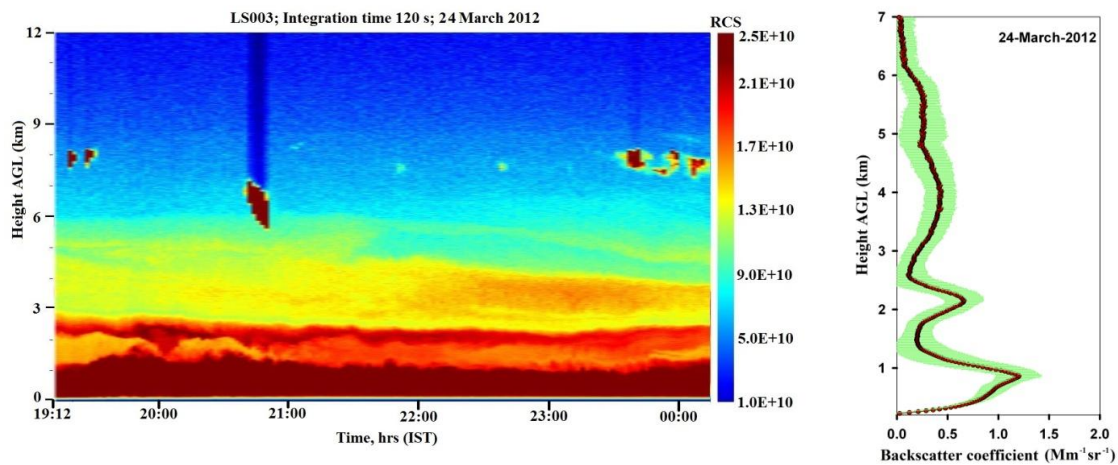


Figure 3.12: Altitude vs time contour plots of range corrected photon counts on 24 March 2012 (left panel), aerosol backscatter profile (right panel) on 24 March 2012 (Standard deviation shown in horizontal error bars).

LiDAR observation on 24 March 2012, presented in Figure 3.12 (left panel), shows the aerosol layers observed at about 700 m, ~2 km and a very shallow layer at about 4 km. The patches of cirrus clouds are also observed above 6 km. The mean

vertical profile of the aerosol backscatter coefficient in Figure 3.12 (right panel) shows the peaks at corresponding elevated aerosol layers with maxima at ~ 700 m. Figure 3.14 (left column) depicts the back air mass trajectories derived at 4.5 and 2 km, for 23, 24 and 25 March, which indicate that the winds are coming mostly from western and north-western part of the world. The 4.5 km elevated layer gradually weakens and this could be justified from the 4.5 km trajectory which shows far separated blue and red circles indicating that the air mass now spends less time over the aerosol loaded region. However, strong aerosol layer at 700 m is due to air masses that are transported from adjoining regions via boundary layer evolution and associated mixing.

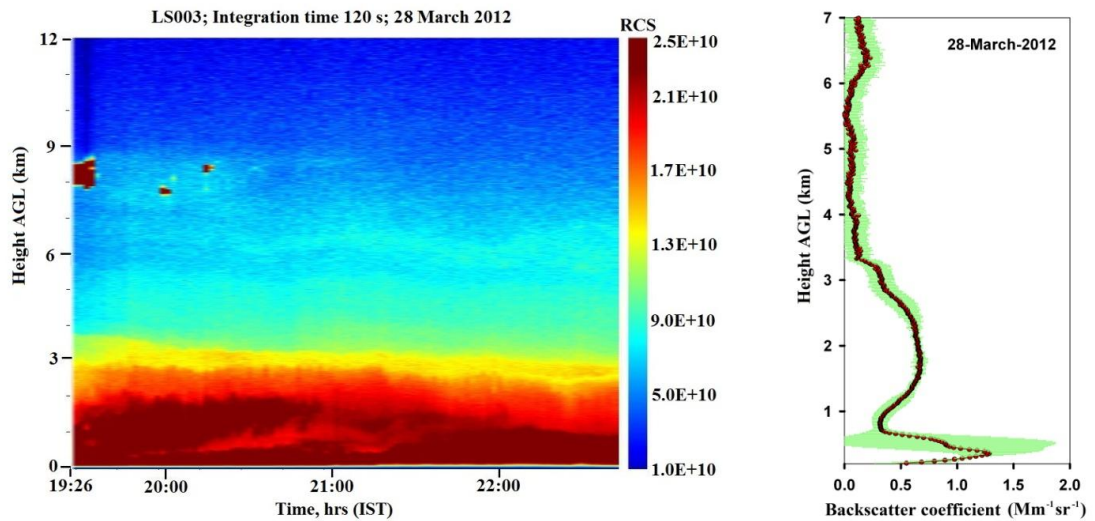


Figure 3.13: Altitude vs time contour plots of range corrected photon counts on 28 March 2012(left panel), aerosol backscatter profile (right panel) on 28 March 2012 (Standard deviation shown in horizontal error bars).

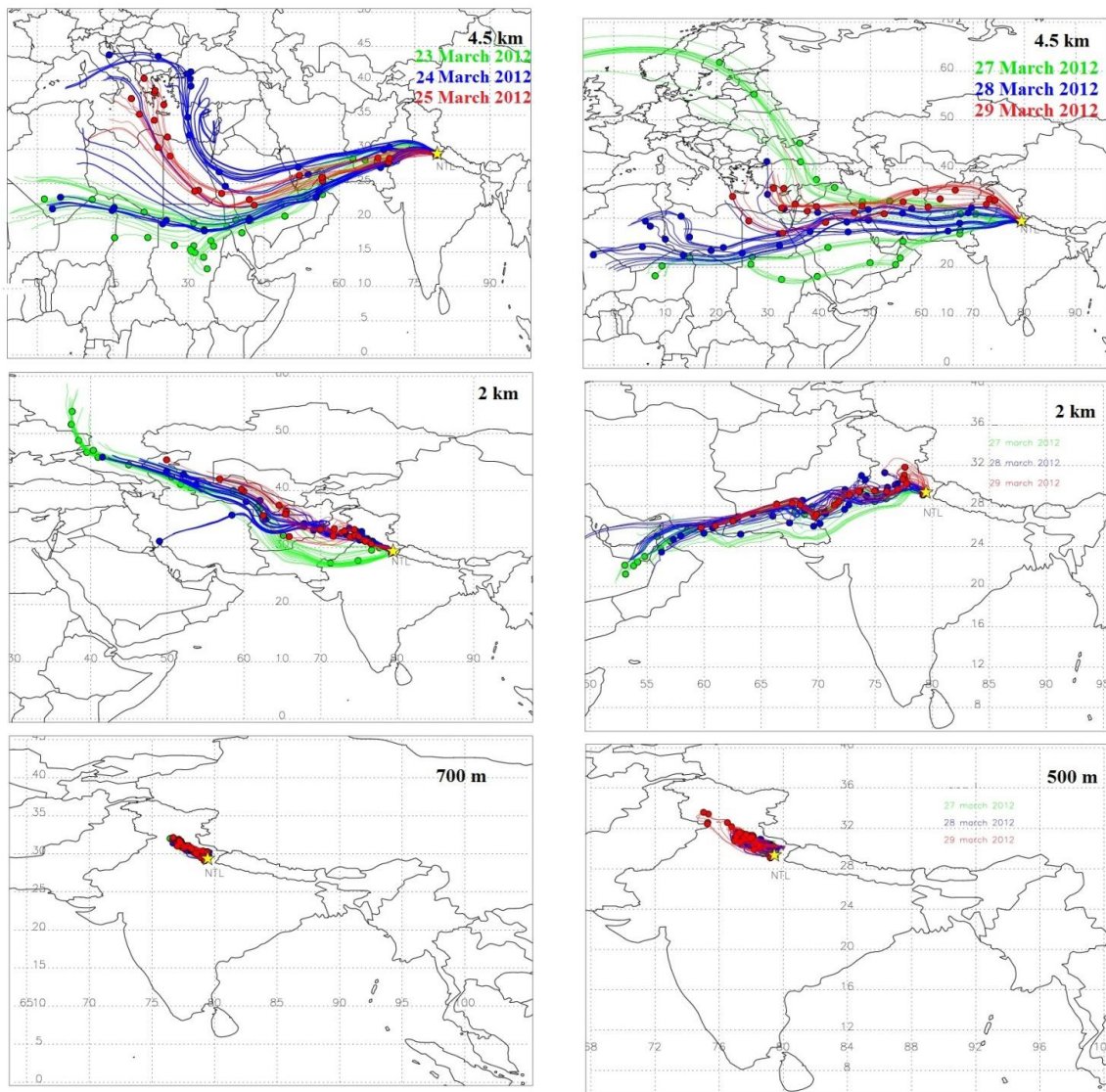


Figure 3.14: (left column) HYSPLIT seven days back trajectories of air mass analyzed for 23, 24 and 25 March 2012 at three different altitudes: (top panel) 4.5 km, (middle panel) 2 km, and (bottom panel) 700 m. (Right column) HYSPLIT seven days back trajectories of air mass analyzed for 27, 28 and 29 March 2012 at three different altitudes: (top panel) 4.5 km, (middle panel) 2 km, and (bottom panel) 500 m.

RTI profile for a normal day (28 March 2012) is shown in Figure 3.13 (left panel), demonstrating a very shallow air mass above 1.5 km, and a significant aerosol layer only up to about 1 km. Corresponding backscatter coefficient given in Figure 3.13 (right panel) shows the prominent peak at about 1 km and no signature of multiple layers are seen. The back air mass trajectory at 4.5 km AGL reveals that the prevailing wind during the previous day have the same origin as the other days; and on the subsequent day, the air masses are quite westerly but without aerosol loading as shown by Figure 3.14 (right column, top panel). Trajectory at 2 km shows that air masses are following the same path during all three days; whereas, at 500 m the air masses are originating from the nearby regions within few 100 km. From figure 3.11 and Figure 3.14 general inference is that, the air masses reaching at high altitudes over the site are basically transported from very far distances, whereas the lower altitude (below 1 km) layers are mostly contributed by the dry air masses from western part of the country.

Figure 3.15 (left panel) shows contour plot of time averaged AOD for 18-23 March 2012 derived from MISR (555 nm) instrument on TERRA satellite, indicating a high AOD (>1.0) over Saudi Arabia, Red Sea, Punjab and North East Pakistan regions. Satellite derived AOD values compliment the origin of aerosols, which are transported to long distances, as explained by the trajectory analysis particularly to the higher altitude aerosol layers above 4 km. The 4.5 km elevated layer is due to the long range transport from Saudi Arabia as the time spent by the air mass is more in this region (shown by the clustering of red circles over the region). An elevated layer at about 3.5 km may be attributed to have been originated from the nearby regions of Punjab and North East Pakistan as clusters of air masses over this region are evident in the trajectory. Figure 3.15 (right panel) depicts the MISR derived contour plot of AOD (time averaged from 25 to 29 March 2012), representing appreciable decrease in AOD from being greater than 1 during 18-23 March to less than 0.6 for 25-29 March 2012; and thus, indicating the absence of elevated layer on 28 March. The LiDAR derived AOD values for 22, 24 and 28 March 2012 are 0.023, 0.025 and

0.018, respectively. The cause for the formation of these elevated aerosol layers may be the convective lifting of the dry air to higher levels, at a distant source containing mostly aerosols and dust that are long range transported to the pristine site Nainital. Such elevated layers of aerosol which mainly consists of coarse mode particle primarily dust, as suggested by the angstrom exponent being less than one (0.817) for 22 March, can play crucial role in heating the atmosphere [Lau *et al.*, 2006]. Also, the long wave absorption caused due to these dust particles can significantly contribute to tropospheric warming over the central Himalayas.

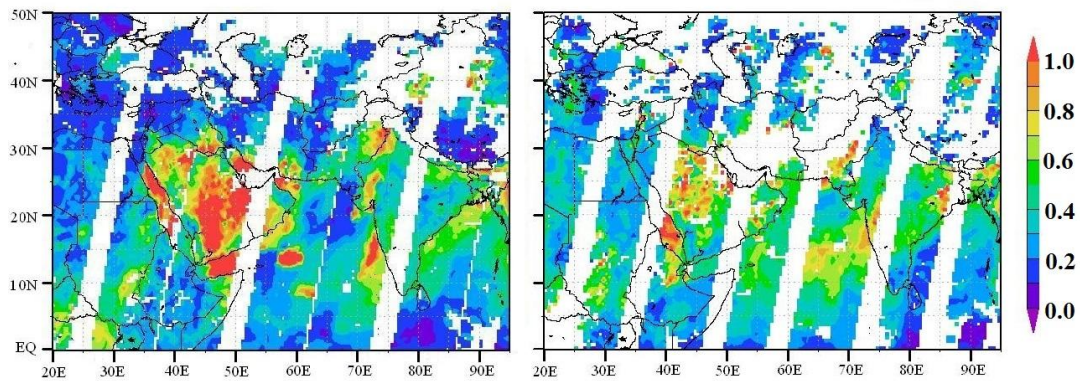


Figure3.15: Time averaged contour plots of columnar AOD (555 nm) (Green band, unit less) derived from MISR satellite (MIL3DAE.004) during: (left panel) 18-23 March 2012, (right panel) 25-29 March 2012.

3.4 Summary and conclusions

Aerosol vertical distribution over a high altitude, regional representative site in the central Himalayas is analyzed with intermittent LAMP observations. In this chapter, observations made during the period of March-2012 to May-2013 are presented, with primary goal of studying the seasonality in aerosol vertical distribution and comparison with CALIPSO satellite products, for the first time over such a complex terrain. The structure of vertical distribution was generally multi-layered during the spring season on account of long range transport of aerosol from arid region in the west and north-west. Strong seasonality in the mean vertical profile of aerosol is prominent within the lower 4 km, particularly in spring and summer seasons. During the autumn and winter seasons, the site is quite pristine in air quality due to the confinement of aerosol in the PBL below the altitude of site.

The comparison study of CALIPSO is presented for more than yearlong LiDAR observation, the mean bias is estimated to be +18% in spring season +22% in the autumn and +32% in the winter season. The profiles from LiDAR and CALIPSO revealed almost similar structure throughout the vertical column in the autumn and winter, whereas some discrepancies were observed at altitudes below 3 km during the spring season. The difference in the profiles for lower heights during spring season can be attributed to 1) Local boundary layer variation influenced by complex topography, 2) horizontal aerosol inhomogeneity within the mixed layer and 3) spatial mismatch of measurements. Nevertheless, this comparison study over the central Himalayas would contribute in the better utilization of CALIPSO aerosol products, and for investigating the changes in vertical distribution of aerosols that usually contribute to the radiation budget of the atmosphere in different ways at different altitudes. Comparison of satellite observations with ground measurement over this region is of paramount importance for understanding radiative effects of aerosol over the Himalayas.

As a result of intermittent observations on the vertical profiling of aerosol, elevated layers (basically dust) were detected on 22 and 24 March 2012, for the first time formation of aerosol layer at an altitude of about 4.5 km was observed over the site on 22 March 2012, which is quite unusual. The origin of such layers is found to be associated with convectively lifted dust over dry arid North Africa and Saudi Arabian region. The source and transport of the aerosols is explained by Satellite observations (TERRA) and back air mass trajectory analysis.

Chapter # 4

Surface layer characteristics over a mountain ridge in different synoptic conditions

This chapter presents time-variability of surface-layer characteristics during spring (March-May 2013) and winter season (November 2013 - January 2014) over Manora peak (29.4°N, 79.5°E, 1926 m above mean sea level). We mainly utilize the three-dimensional wind components and virtual temperature observed with sonic anemometers (sampling at 25 Hz) mounted at 12-m and 27-m height on a meteorological tower. The wind flow at this ridge site is quite different from slope flows in spring season. Notwithstanding the prevalence of strong large-scale north-westerly winds, diurnal variation of the mountain circulation is clearly discernible with the strengthening of wind speed and a small but distinct change in wind direction during the afternoon period. However, during the winter season dominance of mountain wind system over the regional flow is observed with a reversal of wind direction in the course of the day. Tilt corrections using the planar fit method (sector-wise planar fit method) have been applied to convert the measurements to streamline-following coordinate system for the spring season (winter season) before estimating turbulence parameters. The seasonal and diurnal variability in measured fluxes of momentum and heat, along with turbulent kinetic energy (e) has been analyzed.

Sensible heat flux (H) exhibits prominent diurnal variations attaining peak values ($276 \pm 108 \text{ W m}^{-2}$ for the spring and $116 \pm 52 \text{ W m}^{-2}$ in winter season) from 1200 to 1400 IST; the seasonal and diurnal mean H (from surface to atmosphere) decreases from spring (50 W m^{-2}) to winter (17 W m^{-2}). Although the seasonal mean value of e is reduced by half, from spring to winter but the momentum flux (τ) remains unchanged. Variations of the standard deviations of vertical wind normalized with friction velocity (σ_w/u_) as a function of stability parameter (z/L) indicate that they follow a form of power law variation during the unstable conditions, with an index of $1/3$ for the spring season, whereas for the winter season this index is $1/5$. The coefficients defining the above variations are found to be in agreement with those derived over flat as well as complex terrain for spring season. The value of σ_w/u_* is found to be ~ 1.2 (0.2) during spring (winter) season for neutral stability conditions. A prominent diurnal variation is observed in the vertical wind component as well, depicting almost equal amplitude of variation in both the season, with positive values after 0900 IST attaining peak values of 0.2 to 0.3 m s^{-1} at 1300 IST and reversal to negative values from 1800 IST (1600 IST) in the spring (winter) season.*

4.1 Background meteorological conditions during spring and winter season

During spring season, the study region experiences generally fair-weather and large surface heating by the incoming solar radiation, which favour significant diurnal variations of surface-layer energetics, evolution of ABL and boundary-layer circulation. Space borne regional distribution of clouds shows that the 10°-30°N latitude belt over the Indian region is almost cloud-free (< 20 % monthly mean cloudiness) during the spring season [Meenu *et al.*, 2007; 2010]. This is caused by the large-scale tropospheric subsidence associated with the descending limb of the Hadley cell which is located above this region during spring, favouring fair weather conditions and significant diurnal evolution of ABL. In contrast, large-scale cloudiness and precipitation occur over this region during summer, suppressing the clear diurnal evolution of ABL. Winter season over foothills of the Himalayas is generally characterized by ample sunshine, low wind conditions and cloudless-crystal clear skies, and low water vapour content of air, collectively leading to a diathermanous nature of atmosphere [Tiwari and Joshi, 1997] especially over the mountain peaks and ridges; the season also witnesses few instances of rainfall and snowfall as a result of western disturbances. Comparatively little is known about the BL evolution over steep and complex terrain [Singh *et al.*, 2016], since surface layer characteristics over mountains are modulated by the heating and cooling of the slopes in day and night hours respectively. Weak mesoscale wind conditions are crucial in discerning the impact of mountainous topography on the wind flow over a mountains terrain. The lateral temperature gradients over mountain slopes and ridges are the driving force of katabatic and anabatic winds, the transition of these flows from one to another and their strength depends actively on the background winds and passively on the topography of site [Papadopoulos and Helmis, 1999].

Figure 4.1 depicts a comparison of the seasonal mean synoptic circulation at 800-hPa level over the region during the four seasons, obtained from the European Centre for Medium-Range Weather Forecasts (ECMWF)-Interim reanalysis data. Figure 4.1

(a) indicates the large-scale advection of strong north-westerly winds over the Indo-Gangetic plain and the south-central Himalayas during the spring season. The seasonal mean wind (at 800-hPa level) in this belt ranges from 6-10 m s^{-1} ; the observational site (marked by the symbol ‘o’) is located at the northern fringe of this strong north-westerly wind regime during the spring season. In contrast, the mean winds associated with the regional circulation are weaker and significantly variable during the other seasons.

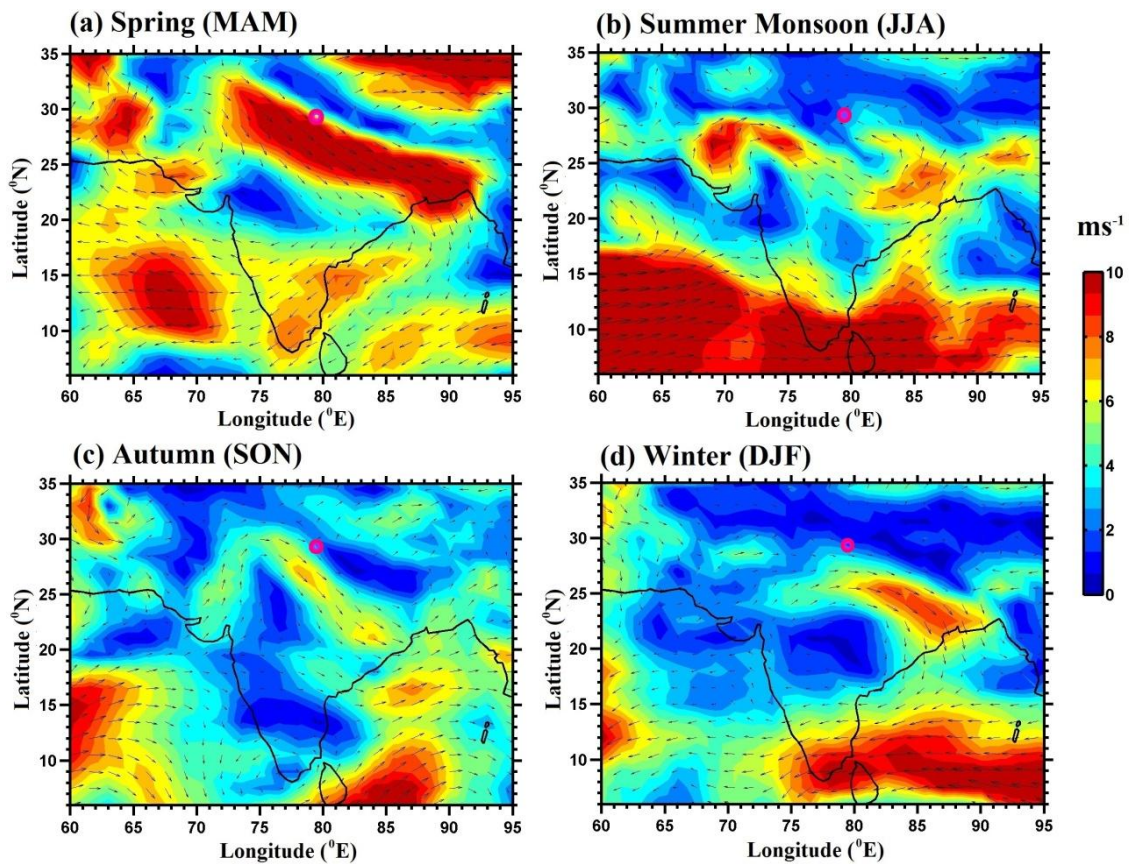


Figure 4.1: Seasonal mean winds at 800-hPa level during (a) spring (March-May), (b) summer monsoon (June-August), autumn (September-November) and (d) winter (December-February) seasons of 2013-14, obtained from the European Centre for Medium-Range Weather Forecasts (ECMWF)-Interim reanalysis data. The colour scale indicates wind speed.

For the complete seasonal cycle presented in Figure 4.1 DJF is presented as winter season, however for rest of the analysis presented in this chapter NDJ is

presented as winter season having a large number of clear sky days, low wind speed and dry conditions. Also, the month of February 2014 was manifested with intense synoptic weather systems leading to snow fall, hailstorms and rains during most of the days.

4.2 Diurnal cycle of meteorological parameters

4.2 (a) Shortwave flux

The monthly mean diurnal variations of the incoming solar radiative flux (shortwave flux, S_{\downarrow}) observed at the site during March, April, and May 2013 is shown in Figure 4.2 (upper panel) along with the variations for the month of November, December 2013 and January 2014 (bottom panel). The vertical bars represent the respective standard deviations. The S_{\downarrow} values at noon attain a peak of 1000-1100 W m^{-2} over this hill station during spring season. Such high values are due to the favourable solar declination, high altitude of the station and clear sky conditions prevailing during this season. The S_{\downarrow} values during April and May are about 100 to 150 W m^{-2} more than the corresponding values during March, indicating an increase in surface heating during April-May.

For the winter season, a well defined diurnal variation is observed during all the months with the peak values ranging between 700 to 800 W m^{-2} . The S_{\downarrow} values during November are approximately 100 W m^{-2} higher than those during December and January, with peak value of 796, 694 and 754 during November, December and January respectively, depicting the average variations in intensity of solar radiation before and after winter solstice. The standard deviation in S_{\downarrow} is an indicator of the presence of isolated cloud patches during each month. Larger standard deviations of S_{\downarrow} observed during the afternoon are due to the increase in the frequency of occurrence of boundary-layer clouds (visual observations) during the afternoon especially during spring season.

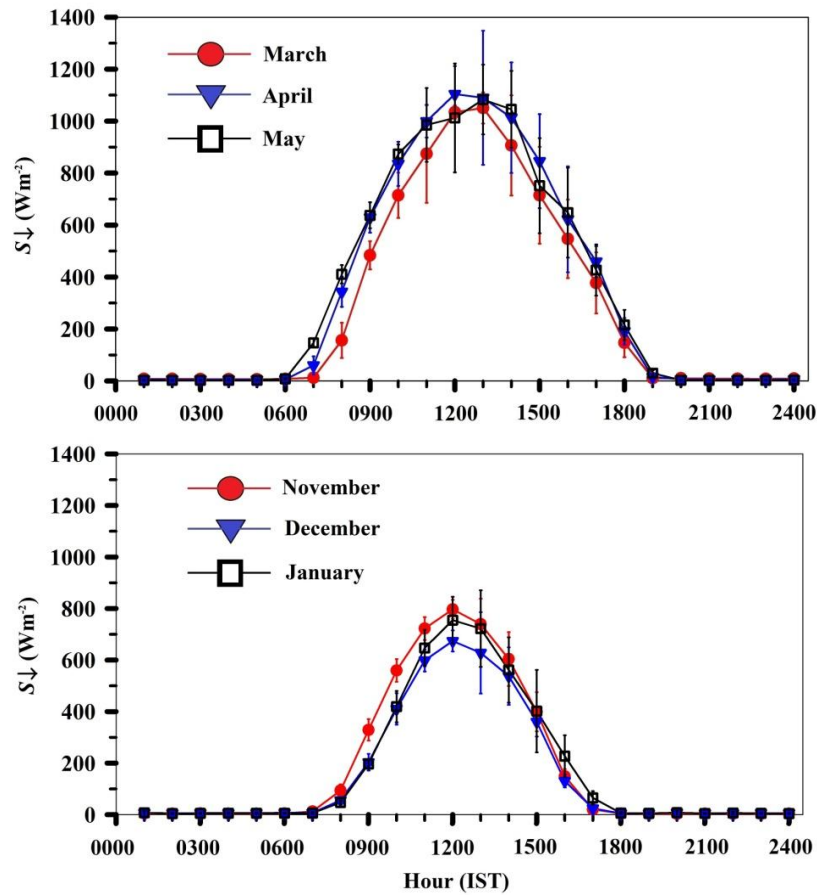


Figure 4.2: Monthly mean diurnal variations of the incoming shortwave solar radiative flux (S_{\downarrow}) during spring (upper panel) and winter season (bottom panel) observed at the site. The vertical bars indicate the standard deviations.

4.2 (b) Wind speed, wind direction and wind shear

Contour maps of the diurnal and seasonal variations of horizontal wind speed and wind direction observed using the sonic anemometer at the 27-m level are given in Figure 4.3. Corresponding contour map of the horizontal wind shear between 12-m and 27-m levels are also shown in Figure 4.3. The monthly mean diurnal variations of wind speed 27-m levels during spring and winter season are shown in Figure 4.4.

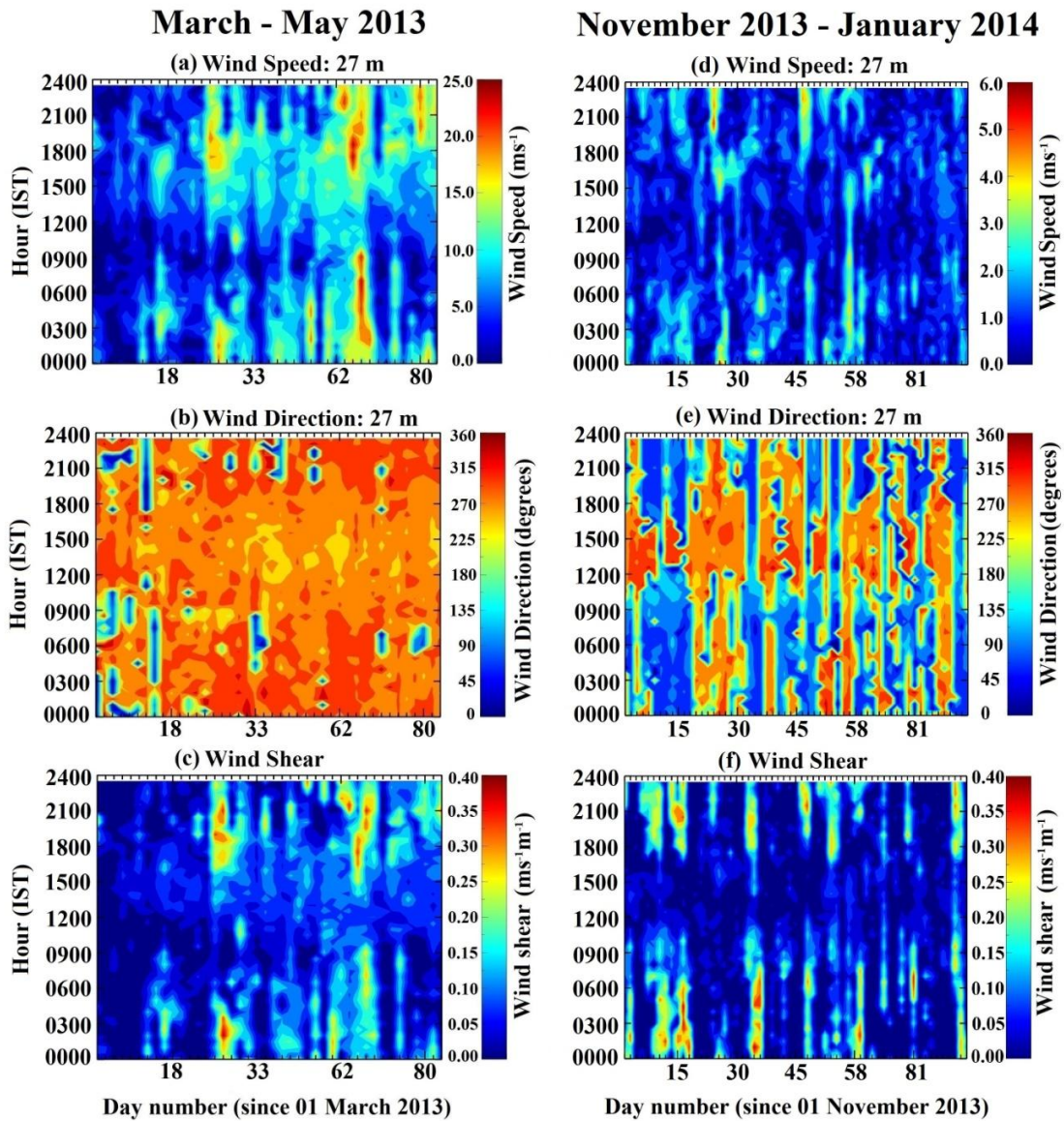


Figure 4.3: Contour maps of the diurnal and seasonal variations of (a) horizontal wind speed, and (b) wind direction observed using sonic anemometer at 27-m level. (c) Same as (a) but for the horizontal wind shear between 12-m and 27-m levels for the spring season, and similarly in panel (d, e and f) for the winter season. The x-axis represents day number and the y-axis shows time of the day. The colour bars on the right side of each panel indicate their respective scales.

Figure 4.3 and Figure 4.4 show that, throughout the spring season, the diurnal variation of wind speed is manifested by two prominent maxima and minima: the minima occur around pre-noon (0900-1100 IST) and midnight (2300-0100 IST),

while the maxima occur in the early morning ($\approx 0400-0600$ IST) and late-afternoon and evening ($\approx 1500-1900$ IST). Among them, the slowest and fastest wind speeds generally occur around the pre-noon and evening periods respectively. The average wind speed systemically increases with the advancement of the season. The wind direction is predominantly north-westerly; however, during the periods of minimum wind speed observed during the pre-noon and midnight period, the wind direction occasionally changes to easterly.

The wind speed observed at the 27 m in spring season is always larger than that at 12 m. At the 27 m, the probability of occurrence of wind speeds $> 7 \text{ m s}^{-1}$ is $\approx 34 \%$ during the night-time while it is only $\approx 22 \%$ during the daytime. At 12-m level, the above probability is 12% during the night-time and rare ($< 3 \%$) during the daytime. The day-night difference in wind speed is largest at the 27-m level. During April and May, the night-time peak winds observed at 27-m level sometimes exceed 10 m s^{-1} . Such events are also associated with significant wind shear (exceeding $0.25 \text{ m s}^{-1} \text{ m}^{-1}$) between the 12-m and 27-m levels, which has the potential for generating turbulent eddies and increasing the vertical mixing of surface-layer air. Phase of the diurnal variation of wind shear is same as that of wind speed, with both of them maximizing around $0400-0600$ IST and $1500-1900$ IST; the peak wind shear increases from March (typically $\approx 0.06 \text{ m s}^{-1} \text{ m}^{-1}$) to April-May (typically $0.2 \text{ m s}^{-1} \text{ m}^{-1}$).

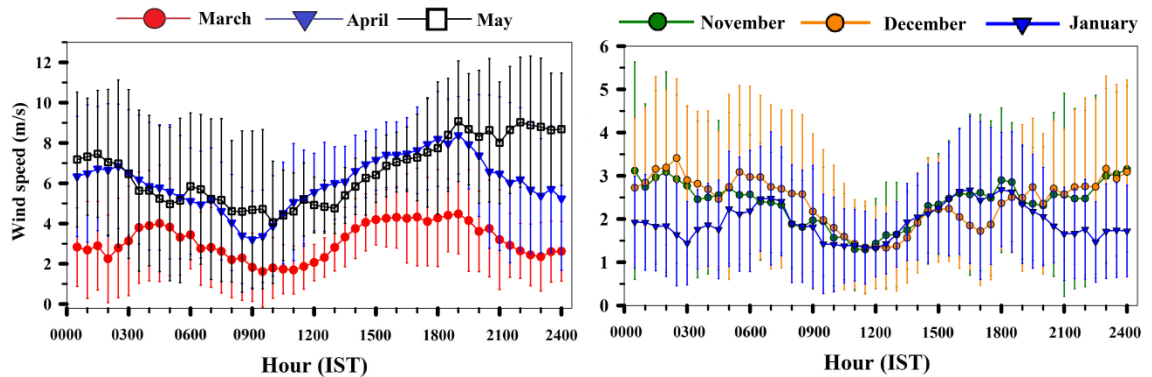


Figure 4.4: Monthly mean diurnal variations of the wind speed during spring (upper panel) and winter season (bottom panel) observed through sonic anemometer at 27-m level. The vertical bars indicate the standard deviations.

MAM 2013

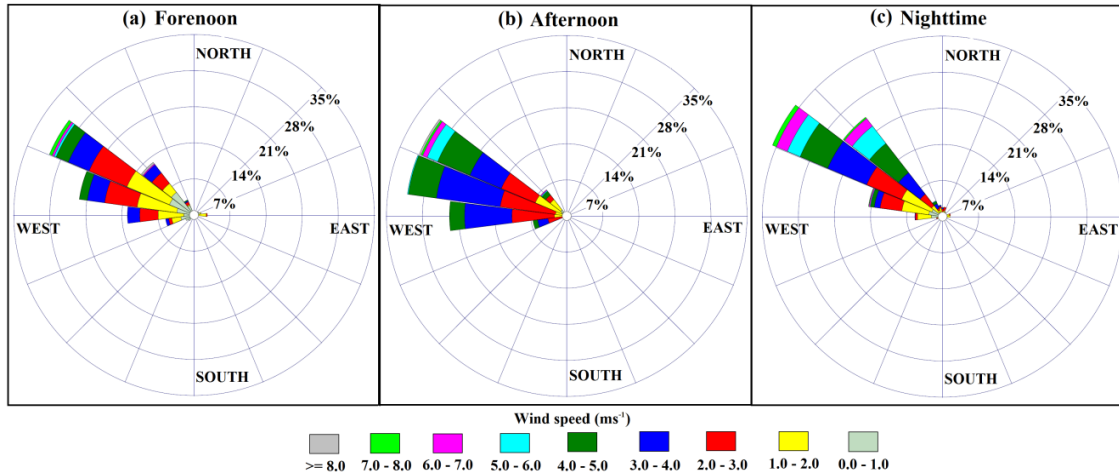


Figure 4.5: Wind roses at the 27-m level for (a) forenoon (0700-1200 IST), (b) afternoon (1300-1800 IST) and (c) night (1900-0600 IST) during the spring season of 2013.

In order to investigate the detailed variations in the wind-direction, the entire dataset for season was segregated into three time bins and plotted as wind rose. Figure 4.5 shows wind roses during the forenoon: 0700-1200 IST; afternoon (1300-1800 IST) and night (1900-0600 IST). In general, the wind direction is predominantly west-north-westerly with rather narrow spread (wind direction is mostly within a cone of 285° and 305°) during the forenoon, while the spread in wind direction is rather wide (nearly equal probability for winds in the cone of 265-305°) during the afternoon. During night, the wind is strong and mostly flows from a cone of 295-315°. Enhancement in the probability of occurrence of westerly winds during the afternoon period, similarity in the wind directions west-north-westerly during the night and forenoon periods, and the considerable enhancement in wind speed during the night are particularly notable. However, even during the afternoon period, the strongest winds ($> 10 \text{ m s}^{-1}$) are generally north-westerly, rather than westerly.

During the winter season, the wind speed is generally close to 2 m s^{-1} from 0900 to 1300 IST, with higher values ($> 3 \text{ m s}^{-1}$) during night-time hours for the month of November and December, whereas in the month of January the wind speeds from 2000 to 0500 IST are also weaker ($< 2 \text{ m s}^{-1}$). The wind directions undergoes regular diurnal variations throughout the season with westerly winds from 1200 to 1800 IST, easterly winds from 1900 to 0800 IST and a transition phase from 0900 to 1200 IST. The wind shear is mostly below $0.10 \text{ m s}^{-1} \text{ m}^{-1}$, however there are also some scattered events of higher wind shear ($> 0.20 \text{ m s}^{-1} \text{ m}^{-1}$) in the nighttime hours corresponding to wind speed more than 3.0 m s^{-1} in Figure 4.3 (d). The strong wind shear in nighttime could be attributed to absence of rising thermals, strengthening of regional wind system thus leading to stronger wind flow with increasing height above the surface of ridge.

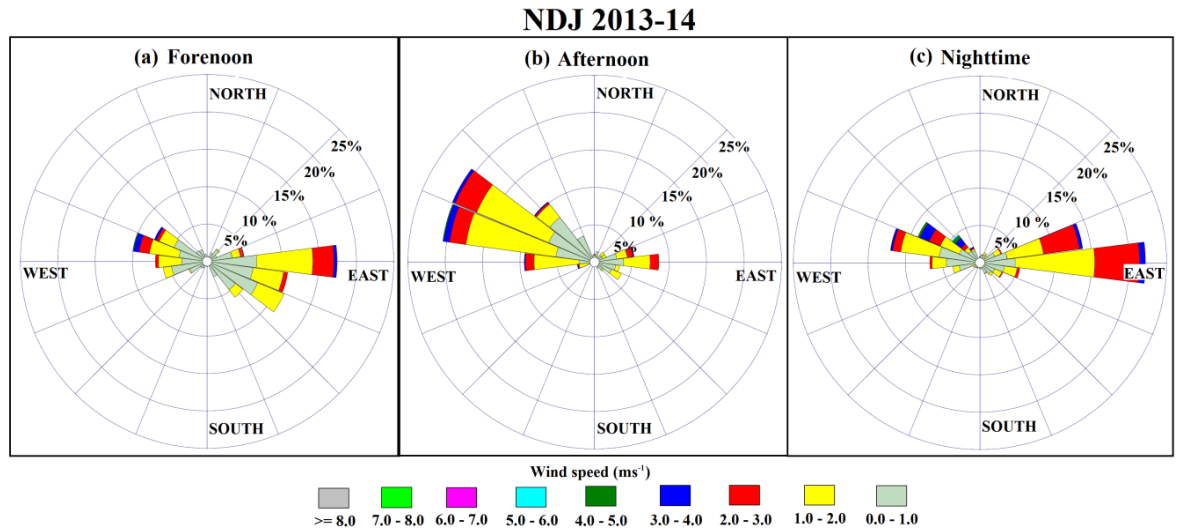


Figure 4.6: Wind roses at the 27-m level for (a) forenoon (0700-1200 IST), (b) afternoon (1300-1800 IST) and (c) night (1900-0600 IST) during the winter season of 2013-14.

4.2 (c) Mixing ratio

The diurnal variations of relative humidity (RH) during spring and winter months were also analyzed. In March, dry condition (mean $RH < 40 \%$) prevails during the post-midnight and morning period and the RH generally increases during the daytime

till about 1500-1600 IST, when the mean RH is $> 80\%$ and sometimes reaches saturation level. The relative humidity undergoes a systematic decrease during the post-sunset period. Visual observations show the boundary layer cloud formation during the afternoon period and their dissipation after the sunset, especially in March. The evening enhancement of relative humidity is smaller during April-May, while the post-midnight dry conditions prevail during this period as well. The diurnal variation of mixing ratio is most prominent in March when it increases from 4.1 g kg^{-1} at 0700 IST to 10.5 g kg^{-1} at 1600-1700 IST. In April, the monthly mean diurnal variation of mixing ratio shows an increase from 4.3 g kg^{-1} at 0600-0700 IST to 8.1 g kg^{-1} at 1300-1500 IST. The water vapour mixing ratio is larger and highly variable during May: on average, it increases from 5.8 g kg^{-1} at 0600 IST to $\approx 11.2 \text{ g kg}^{-1}$ at 1300-1400 IST. The monthly mean water vapour mixing ratio is 6.1 ± 1.9 , 5.8 ± 1.8 and $8.4 \pm 3.8 \text{ g kg}^{-1}$ during March, April and May respectively. The day-to-day variation of mixing ratio is the largest in May (when the average water vapour content is quite high) and the least in March.

The mixing ratio undergoes a consistent diurnal variation throughout the winter season as well with values below 4.0 g kg^{-1} from 1900-1100 IST (on many nights being as low as 1.0 g kg^{-1}) and going above 6.0 g kg^{-1} from 1200-1800 IST, this time period of higher mixing ratio corresponds to the winds coming from western sector which advect air from forested areas, being rich in moisture during daytime due to evapotranspiration. Another possible explanation for higher mixing ratio could be the strong upslope winds after 1200 IST, since intense forest coverage is also present on the eastern as well as the southern slopes, but due to the downslope flow moisture is restrained from reaching the mountain top during night-time. The monthly mean water vapour mixing ratio for winter months is 4.5 ± 2.1 , 4.9 ± 1.7 and $4.1 \pm 1.6 \text{ g kg}^{-1}$ during November, December and January respectively.

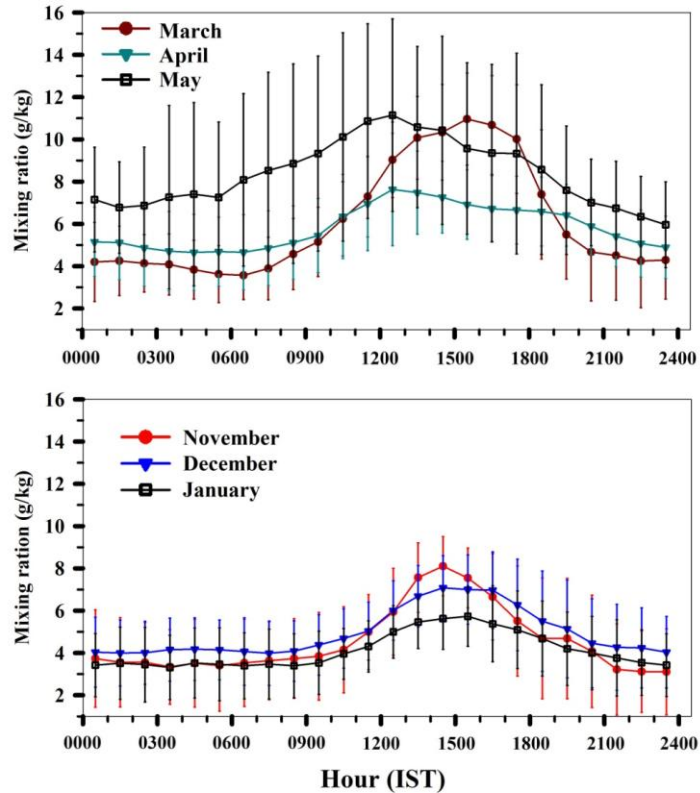


Figure 4.7: Monthly mean diurnal variations of the mixing ratio during spring (upper panel) and winter season (bottom panel) observed at the site. The vertical bars indicate the standard deviations.

From the diurnal variations of wind speed, wind direction, and humidity observed during the spring season we can speculate the following. The variations in all the above stated meteorological variables are more prominent in March, when the background mean wind is weak. The large-scale circulation during this season is predominantly north-westerly. Orientation of the local orography suggests that the upslope winds, generated by surface heating during daytime, would be predominantly south-westerly/westerly. During the daytime, this wind will get added with background north-westerly winds, which enhances the wind speed and the westerly component in it. Strength of this upslope wind would increase during daytime and might have contributed to increase in wind speed observed during afternoon. This may be the reason for larger spread in wind direction, with significant westerly winds, observed during the afternoon (Figure 4.5). These winds bring more air mass from

humid forested areas in west/southwest, especially during daytime, which increase the surface-layer specific humidity till afternoon. This causes the formation of boundary layer clouds in afternoon over the region. In contrast, during night-time, the down-slope winds would be largely easterly/north-easterly. The background wind being north-westerly, this down-slope easterly wind would reduce net wind speed and reduce westerly component in the background north-westerly winds, as observed during the night-time. This makes the flow predominantly north-westerly during nighttime, as observed. The winds from this direction bring more air mass from relatively barren hills (compared to airflow from forested areas in the west/southwest during daytime). This, together with the reduction in evapotranspiration during night, would reduce mixing ratio and relative humidity, as observed during nighttime, especially during post-midnight period.

However, as the site is located near the ridge and that the prevailing background north-westerly winds are rather strong, a complete reversal associated with the katabatic and anabatic winds are not observed, though the effect of these mountain circulations are discernible, especially in the consistent change in wind direction (albeit with small magnitude) and wind speed. The dissipation of ABL clouds after the sunset also supports this inference. The relatively warm nights with nearly constant (or increasing) temperature during the pre-midnight period might have resulted from the vertical mixing of the surface-layer air by wind shear generated turbulence, which prevent the stabilization of cold air near the surface [e.g., *Gustavsson et al.* 1998].

4.3 Applicability of Monin Obukhov similarity theory

In principle, the scaling methods for turbulence variables observed over flat horizontally homogenous terrain are not applicable as such in complex terrain because of the slope winds. Although, studies on the flow and exchange characteristics within and above steep vegetated terrain showed that many statistical properties typical for the flat terrain are also observed in complex terrain [*Rotach and*

Zardi, 2007]. The variations of the standard deviations of vertical wind normalized with friction velocity and standard deviations of temperature normalized with scaling temperature are used here to assess the quality of data and turbulence parameters derived for non-ideal conditions such as complex terrain [Foken and Wichura, 1996; Geissbuhler et al., 2000].

Standard deviations of the wind velocity components normalized by friction velocity (e.g., σ_w/u_*) can be used to verify the applicability of Monin-Obukhov similarity theory (MOST) for the observations and existence of equilibrium conditions in the atmospheric boundary layer [Foken and Wichura, 1996; Geissbuhler et al., 2000]. The variations of σ_w/u_* and standard deviations of temperature normalized with the scaling temperature (i.e., σ_θ/T_*), also referred as integral turbulence characteristics, are also used to assess the quality of data and turbulence parameters derived from them over complex terrain [Foken and Wichura, 1996]. While the above normalized standard deviations remain constant in neutral conditions, they are expected to undergo a power law type variation as a function of stability parameter (z/L) in unstable surface layer, when the stress is non-zero [e.g., Stull, 1988; Mores et al., 2005; Martins et al., 2009; Trini Castelli et al., 2014].

Figure 4.8 shows the variations of bin-averaged σ_w/u_* with z/L for unstable ($z/L < 0$) and stable ($z/L > 0$) conditions for different angles of attack (within $\pm 20^\circ$, $\pm 30^\circ$, and for all ranges within $\pm 45^\circ$) at 27-m level. Results for different angles of attack are presented here to investigate any inconsistency in the observations as a function of angle of attack (though the observations made using USA-1 sonic anemometers equipped with a 3D head-correction are corrected for angle of attack within the range of $\pm 45^\circ$). The dashed curve represents the variations derived by Foken and Wichura (1996) (FW96), while the dotted curve represents the values 30% lower or larger than FW96. The corresponding variation proposed by Panofsky and Dutton (1984) is shown by the dashed-dotted curve. The solid curve represents the curve fitted using the following equation (Foken and Wichura 1996; Moraes et al. 2005).

$$\frac{\sigma_w}{u_*} = A \left[1 + B \left(\frac{z}{L} \right) \right]^C \quad [4.1]$$

The values of A, B and C obtained from the present study for the unstable condition are 1.2, 7.5 and 0.3 respectively for spring season, whereas for the winter season the respective values are 0.2, 1.5 and 0.2. The variation of σ_w/u_* with z/L for unstable conditions for different angle of attack are almost consistent with each other (except for better statistics obtained with wider range of angle of attack) and are mostly within $\pm 30\%$ of FW96 for $-3 < z/L < 0$. It has been suggested that the data may be considered as of good quality if the difference between the measured integral characteristics and those calculated using empirical model is less than about 30%. On the contrary, if additional mechanical turbulence caused by other sources (e.g., obstacles) or artefacts due to terrain effects, surface inhomogeneity, or measuring device itself are present, the measured value of the integral characteristics of the scalars would be substantially larger than those from the model [e.g., *Panofsky and Dutton*, 1984; *Foken and Wichura*, 1996]. The empirical model following *Panofsky and Dutton* [1984] has $A = 1.25$, $B = 3.2$ and $C = 1/3$, and the curve shows general agreement with the present observation for $-3 < z/L < 0$.

During neutral conditions ($z/L \approx 0$), the value of σ_w/u_* is found to be ≈ 1.2 , which is comparable to the value reported by *Moraes et al.* [2005] and *Panofsky and Dutton* [1984] for the spring season, whereas for the winter season the near neutral value is comparatively much smaller (0.2).

Low wind conditions are important in understanding the pollutants dispersion over mountainous terrain [*Moraes et al.*, 2005] however, due to the very weak turbulence intensity in calm conditions, the applicability of Monin-Obukhov similarity theory (MOST) still needs to be properly understood and so does the dispersion relations. *Martins et al.* [2009] through turbulence measurements at the edge of sharp cliff, found MOST as appropriate to describe turbulence characteristics for all conditions in case of vertical wind component and temperature, however applicability was limited for the horizontal wind components.

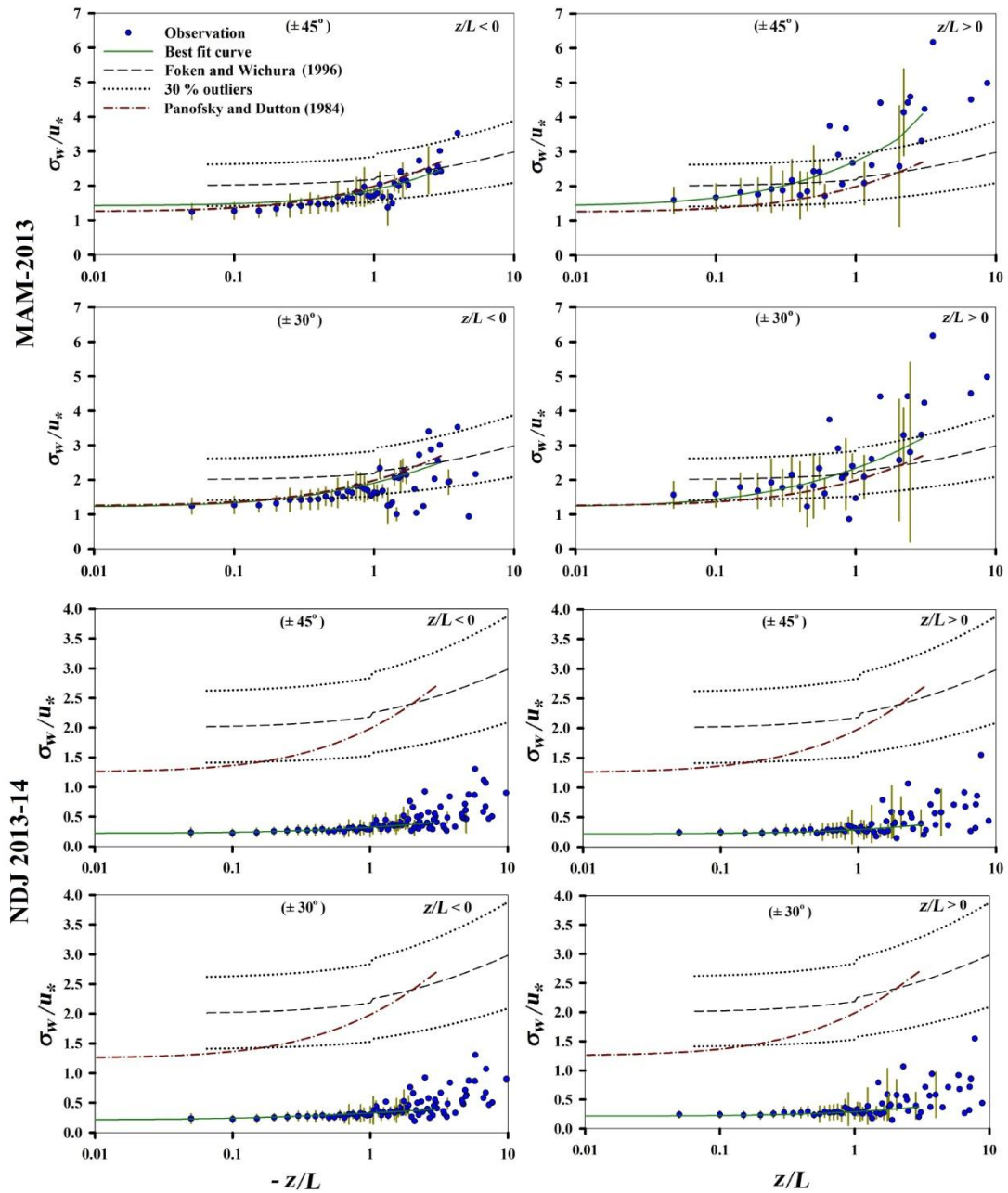


Figure 4.8: Variations of bin-averaged σ_w/u_* with z/L for unstable ($z/L < 0$) and stable ($z/L > 0$) conditions during spring and winter season, for different angles of attack (within $\pm 30^\circ$ and for all ranges within $\pm 45^\circ$) at 27 m height. The solid line represents the curve fitted using the present observations. The dashed line represents the variation derived by Foken and Wichura (1996) (FW96). The dotted line represents the values 30% lower or larger than FW96. The variation proposed by Panofsky and Dutton (1984) is shown by the dashed-dotted line.

Figure 4.9 shows the variation of σ_θ/T_* with z/L for different ranges of the angle of attack. Under unstable conditions, variation of σ_θ/T_* with z/L shows a relationship (fitted line in Figure 4.9):

$$\frac{\sigma_\theta}{T_*} = 2.13 \left(\frac{z}{L}\right)^{-1/3} \quad [4.2]$$

$$\frac{\sigma_\theta}{T_*} = 13.51 \left(\frac{z}{L}\right)^{-1/2} \quad [4.3]$$

Equation 4.2 and 4.3 correspond to the fitted line in Figure 4.9 for spring and winter season respectively. This relationship and coefficients are in agreement (for the spring season) with the general understanding that the variation of σ_θ/T_* with z/L follows a power law variation with an index of $-1/3$ during unstable conditions [Wyngaard *et al.*, 1971; Stull, 1988; Moraes *et al.*, 2005].

Notwithstanding the complexity of the terrain and the corrections applied to the measurements, comparison of Figure 4.8 and Figure 4.9 with the empirical model relationships reported in the literature show that the present data quality is good to estimate turbulence fluxes. However, it may also be noted here that consideration of the integral statistics alone may not be adequate to provide complete quality assessment.

Unlike vertical winds, the variations of normalized standard deviations of u and v with z/L may not follow MOST, as they might be significantly influenced by large-scale convective cells having length scale of mixed layer height, z_i [e.g., Moraes *et al.*, 2005]. These variables are to be scaled by the convective velocity scale (w_*) and are related to z_i/L rather than z/L . As the present observations do not have direct information on z_i , variations of the normalized standard deviations of u and v as a function of z_i/L are not presented here.

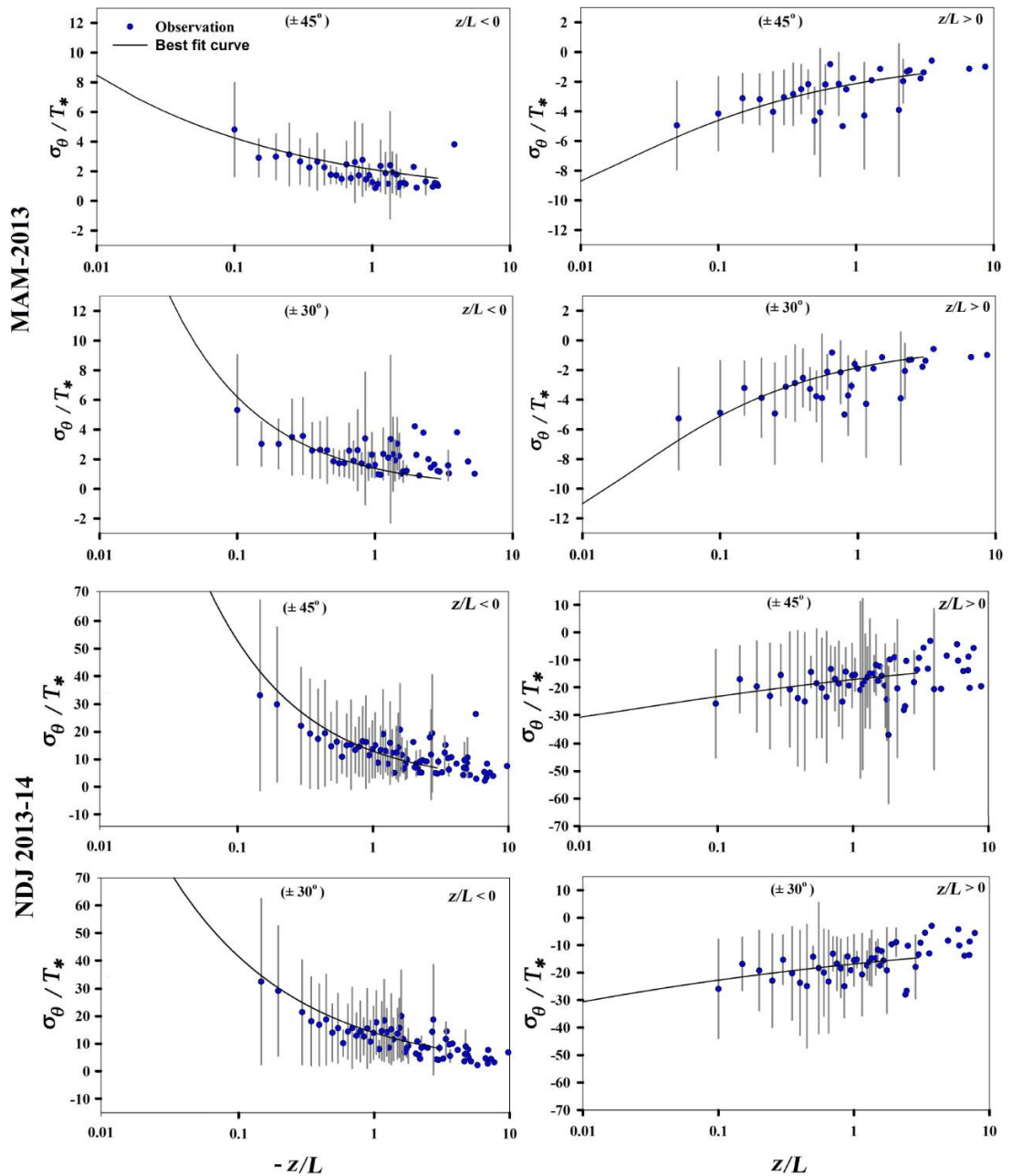


Figure 4.9: Variations of bin-averaged σ_{θ}/T_* with z/L for unstable ($z/L < 0$) and stable ($z/L > 0$) conditions during spring and winter season, for different angles of attack (within $\pm 30^\circ$ and for all ranges within $\pm 45^\circ$) at 27 m height. The solid line represents the curve fitted using the present observations.

4.4 Time variability of surface layer fluxes

4.4 (a) Sensible heat flux

Diurnal variation of H is highly prominent for both spring and the winter season. For the spring, H increases systematically after ≈ 0800 IST, attains peak values during 1200-1400 IST and decreases to negative night-time values by ≈ 1800 IST. The time of occurrence of the peak H values is in agreement with the phase of the largest surface heating by the incoming shortwave solar flux as depicted in Figure 4.10 (a). The peak value of H is the largest ($353 \pm 147 \text{ W m}^{-2}$) in May and the least ($222 \pm 46 \text{ W m}^{-2}$) in March. The peak value of H during April-May is larger than the corresponding values observed at some of the plain tropical regions. Such high values of H over this Himalayan station during spring are aided by the large values of shortwave radiative flux (which heat the surface) and the vertical winds that might prevail during the daytime. A rather weak downward transport of H is observed during the night-time (typically H in the range of -10 to -25 W m^{-2}), magnitude of which is more prominent during April-May. In contrast, the magnitude of the night-time H is least during March (typically $+5$ to -10 W m^{-2}). The net diurnal mean upward transfer of H from surface to atmosphere during the spring season is 50 W m^{-2} .

Distinct diurnal variability in H is observed for all months of the winter season (Figure 4.10 (b)), with peak noon-time value being $116 \pm 80 \text{ W m}^{-2}$ and net diurnal mean of $+17 \text{ W m}^{-2}$. Atmosphere to surface transport of heat is observed from 1800 to 0800 IST throughout the season, with average value of -20 , -12 and -8 W m^{-2} during November, December and January respectively, this reduction of nighttime heat flux is probably due to the decrease in the air temperature from November to January, implying lower temperature contrast between surface layer and ground.

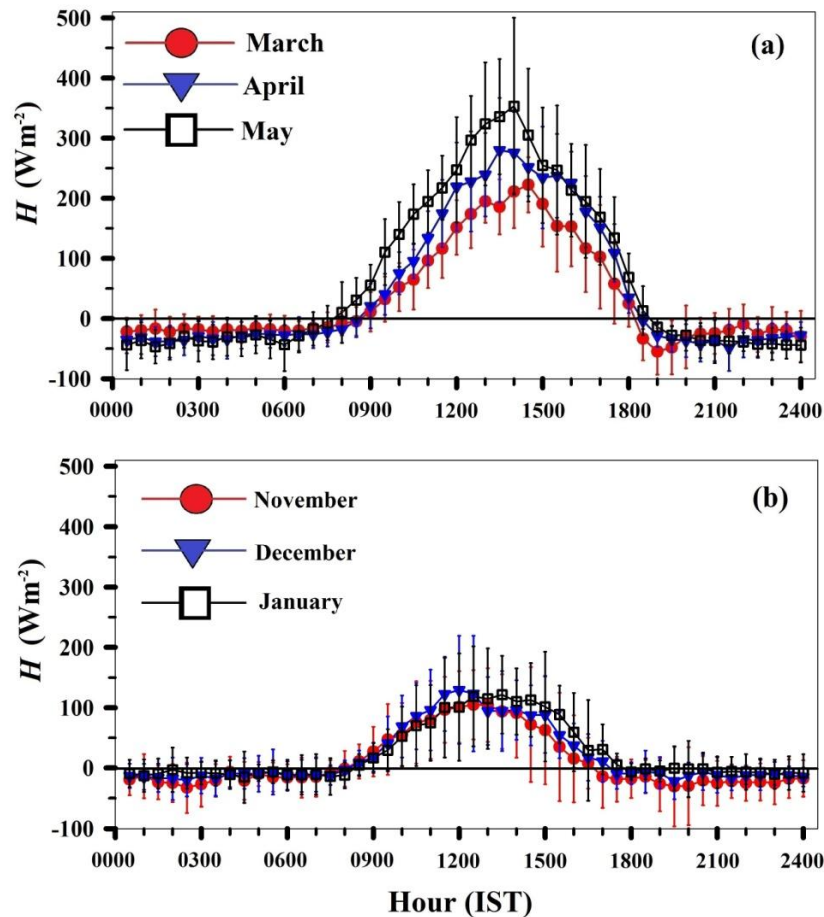


Figure 4.10: Monthly mean diurnal variations of the sensible heat flux (H) during (a) spring and (b) winter season observed at the site. The vertical bars indicate the standard deviations.

4.4 (b) Momentum flux and turbulent kinetic energy

The diurnal variation of e during March is quite small, while the values of e show an enhancement in the afternoon (especially during 1500-1600 IST) during April-May. These afternoon peak values of e observed during April-May are almost 30-50 % larger than the corresponding values observed during the night-time, indicating the magnitude of the increase in the turbulence strength during the afternoon. Note that, during April-May, the peak values of e are attained about 2 h after the peak values of the incoming shortwave flux and H are attained. However, as seen earlier, the

turbulence generated by wind shear would be increasing in the afternoon period, till late evening or early night. The observed variations in e clearly show the continued increase in the production of turbulence by the systematic increase in wind shear during the afternoon period, even after the intensity of the thermals started decreasing during the afternoon. Interestingly, the nocturnal values of e also increase from March to May, which might be due to the corresponding increase in wind shear, which enables the increase in turbulence intensity. The τ observed during the March-May period does not show any well discernible diurnal variation, although the values during the afternoon are marginally larger than those during the post-midnight period. The net diurnal spring season mean of e and τ are $1.46 \text{ m}^2 \text{ s}^{-2}$ and 0.09 Nm^{-2} respectively.

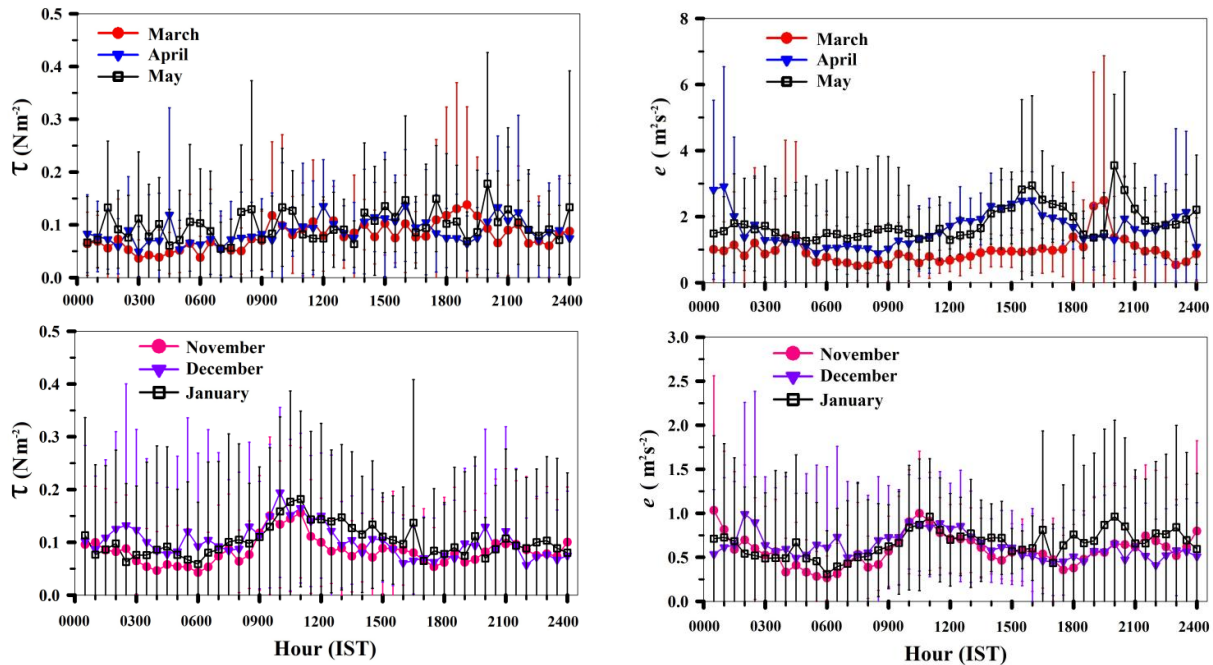


Figure 4.11: Monthly mean diurnal variations of turbulent kinetic energy (e), and momentum flux (τ) during spring (top panels) and winter season (bottom panels) observed at the site. The vertical bars indicate the standard deviations.

A less prominent diurnal variability is depicted by e and τ for the winter season also, showing marginally higher values during 0900 to 1300 IST. This period of

higher turbulence and stress also corresponds to the transition phase of the wind direction (from easterly to westerly), lower wind speeds, gradual change of solar inclination and direction (from east to south). The magnitude of e and τ reduces after 1200 IST when wind direction of the mountain winds is also westerly, being similar to the regional flow of weak ($< 2 \text{ m s}^{-1}$) westerly winds. From these observations it can be inferred that, the evolution of mountain wind system and its interaction with regional wind system results in higher values of e and τ . The net diurnal winter season mean of e and τ are $0.62 \text{ m}^2 \text{ s}^{-2}$ and 0.10 Nm^{-2} respectively.

4.5 Time variability of vertical winds

Vertical wind component is a very crucial parameter in deciding the day to day weather, vertical transport of momentum, and pollutants, and the direct measurements on vertical motions are rarely available. Here, sonic anemometer adds a unique value to quantify the role of orography in terms of slope winds. A clear transition between downslope and upslope winds is depicted (Figure 4.12) by diurnal variations of the vertical wind component (w) for spring and winter season. The transition between positive ($+w$) and negative ($-w$) values is rather systematic. In the spring season positive values (mean 0.17 m s^{-1}) are observed from 0900 to 1500 IST and negative values (mean 0.10 m s^{-1}) from 1830 to 0830 IST; for the month of March the evening transition take place at 1730 IST. However, for the winter season (Figure 4.12 (bottom panel)) the magnitudes of mean and maximum values of vertical wind are reduced by half and the evening transition from positive to negative values takes place 3 hours earlier, showing positive values (mean 0.12 m s^{-1}) from 0900 to 1500 IST and negative values (mean 0.05 m s^{-1}) from 1530 to 0830 IST.

Vertical wind component in combination with mean horizontal winds would result in upslope and downslope flows, with upslope flows reaching the mountain peak during daytime from the southern and western slopes. The positive values of w (0900 IST onwards) show a rather consistent pattern (increasing and decreasing) in all months as a response to systematically increasing radiative heating of the ground

during daytime. In nighttime (1700 to 0800 IST) a weaker downslope flow is observed with comparably stronger magnitudes (similar for all three months) around 0600 and 1800 IST in winter season (1900 IST for spring season), otherwise showing variable patterns from 1930 to 0400 IST in different months.

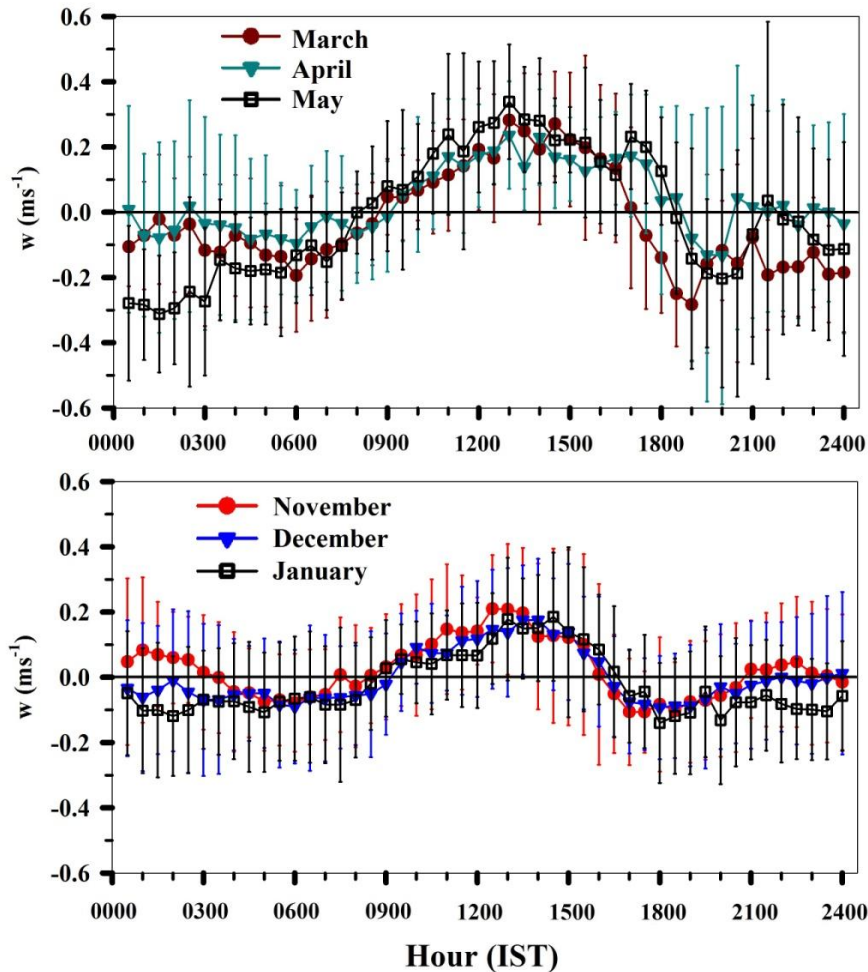


Figure 4.12: Monthly mean diurnal variations of the vertical wind component (w) during spring (upper panel) and winter season (bottom panel) observed at the site. The vertical bars indicate the standard deviations.

Since downslope flow intensity is inversely proportional to ambient stability [Zhong and Whiteman, 2008], one can infer from the stability of atmospheric flow over the ridge from the magnitude of w ; thus stronger magnitude of w at the time of

day and night transitions indicate weaker stability over the ridge, whereas being strongly stable around midnight hours (2100 to 0300 IST). Remarkably, for the month of May and January, around midnight the vertical winds are rather strong in comparison to other months of the season (almost comparable to the peak positive magnitude of the season). Contrastingly, the horizontal wind speed (around midnight hours) are highest (8.0 m s^{-1}) in month of May for the spring season and lowest (2.0 m s^{-1}) for the month of January in winter season.

4.6 Stability parameter

Diurnal variation of z/L (depicted in Figure 4.13) shows the development of instability during the daytime while the nocturnal surface-layer is generally stable or neutral. In the spring season, analysis shows that during the daytime unstable conditions prevail for 85 % of the time, while the frequency of occurrence of stable conditions is 14 % at 27-m level. In contrast 10 % of the night-time is either unstable or neutral and stable conditions prevail only for about 90 % of the time at 27-m level. Inferences observed using the observations at 12-m level are also similar. The significant occurrence of night-time neutral or unstable conditions is associated with the large wind shear during the early night, which leads to mixing of the surface-layer air mass.

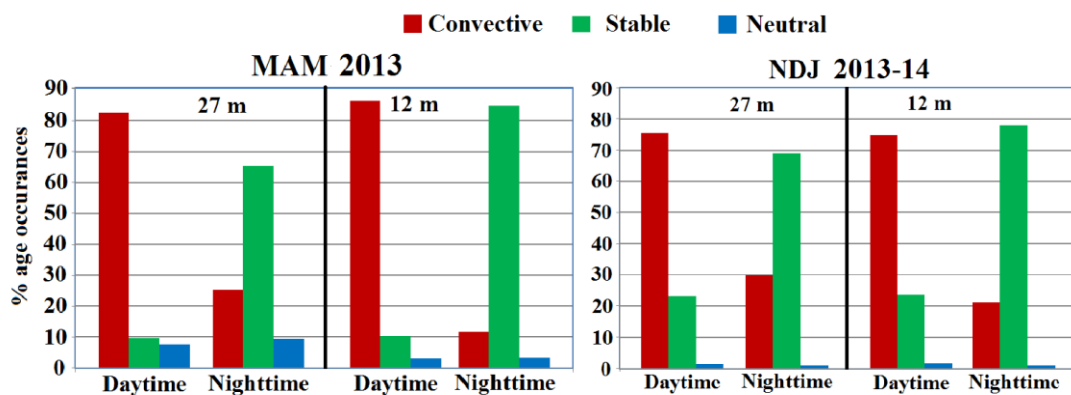


Figure 4.13: Frequency of occurrence of unstable, neutral and stable conditions observed in the daytime and night-time during spring and winter season.

For the winter season, the stability parameter (z/L) analysis displays a milder contrast in the percentage occurrence of stable and unstable conditions in day and nighttime respectively, with unstable (75 %) / stable (70 %) conditions in daytime / nighttime respectively. In contrast with spring season the neutral conditions are rather uncommon in winter season, being less than 2 % at both levels during day and night.

4.7 Impact of wind speed on surface layer fluxes

As the surface-layer turbulence might be affected by wind speed, diurnal variations of H , e , τ and z/L during the days when the daily mean wind is calm ($< 1.5 \text{ m s}^{-1}$), moderate ($1.5 \text{ to } 4 \text{ m s}^{-1}$) and strong ($> 4 \text{ m s}^{-1}$) are further investigated for spring season.

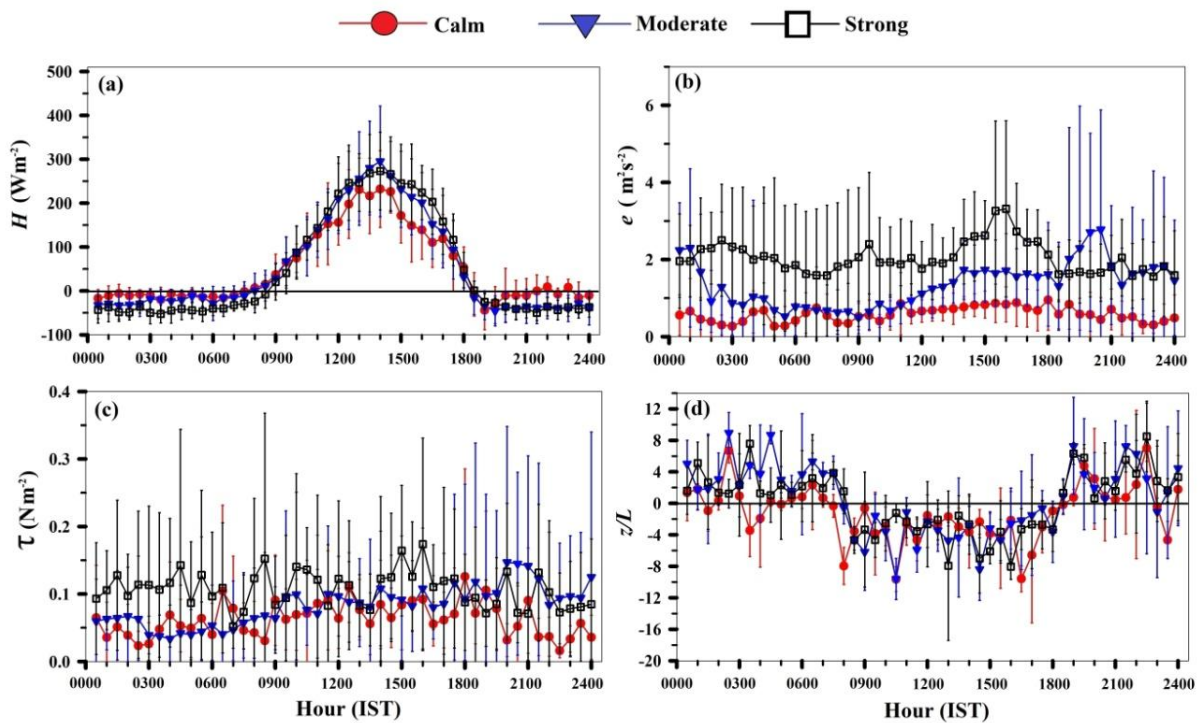


Figure 4.14: Monthly mean diurnal variations of (a) sensible heat flux (H), (b) turbulent kinetic energy (e), (c) momentum flux (τ) and (d) stability parameter (z/L) during MAM-2013, for different daily mean wind conditions: calm ($< 1.5 \text{ m s}^{-1}$), moderate ($1.5 \text{ to } 4 \text{ m s}^{-1}$) and strong ($> 4 \text{ m s}^{-1}$). The vertical bars represent the standard deviations.

As shown in Figure 4.14, the e values are distinctly larger when the mean winds are stronger, with an average enhancement from $0.7 \text{ m}^2 \text{ s}^{-2}$ during calm wind conditions to about $2 \text{ m}^2 \text{ s}^{-2}$, when the winds are strong. The momentum flux almost doubles between the calm and strong wind conditions. The H shows an enhancement of $\approx 50 \text{ W m}^{-2}$ in the noon-time values during strong wind periods compared to calm periods.

4.8 Summary and conclusions

Surface-layer characteristics over the mountainous terrain of the south-central Himalayas are unexplored. First observations of the diurnal variations of micrometeorological parameters and surface-layer characteristics derived from fast-response sonic anemometer observations carried out at two height levels (at 12 m and 27 m on a meteorological tower) near a mountain ridge at the south-central Himalayan station, Nainital (29.4°N , 79.5°E , 1926 m surface elevation) during the spring season (March-May of 2013) and winter season (November 2013 – January 2014) are investigated. This study focuses on spring and winter as significant heating of the surface by solar irradiance and fair-weather conditions that prevail during these seasons provide favourable conditions for the systematic diurnal evolution of the ABL. These observations also provide an opportunity to investigate the variations in mountain circulation when the region experiences strong north-westerly background winds associated with synoptic circulation and during winter season when mean winds associated with the regional circulation are weak (2 m s^{-1}).

Aided by the favourable solar declination, high surface elevation and clear sky condition, the incoming shortwave flux at surface attains peak noon-time values of $1000\text{-}1100 \text{ W m}^{-2}$ during the spring season. The wind speed generally increases from a minimum at ≈ 0900 IST to maximize around the evening and early night. The wind shear is quite significant during the evening and night, with its phase similar to the wind speed; the peak wind shear increases from March (typically $\approx 0.06 \text{ m s}^{-1}\text{m}^{-1}$) to April-May (typically $0.2 \text{ m s}^{-1}\text{m}^{-1}$). In general, the wind direction is mostly within a

cone of 285° to 315° during the night-time and forenoon, while the occurrence of westerly winds ($265\text{-}305^\circ$) increases during the afternoon. This reveals the effect of the diurnally varying upslope and downslope winds and the drainage circulation in modulating winds over the mountain ridge, which experiences strong prevailing large-scale synoptic winds. As the site is located near the ridge and that the prevailing background north-westerly winds are rather strong, a complete reversal associated with the katabatic and anabatic winds is not observed. Dry condition (mean $RH < 40\%$) prevails during the night and morning period (when the wind is predominantly north-westerly from the barren areas), while the RH generally increases to $>80\%$ during the daytime till about 1500-1600 IST (when the occurrence of westerly wind is frequent, bringing humid air from the forest areas). The observed diurnal variation in RH in spring season arises mainly due to enhancement in water vapour mixing ratio (which typically increases from 4.1 g kg^{-1} at 0700 IST to 10.5 g kg^{-1} at 1500-1600 IST) rather than the variations associated with temperature. This causes the formation of boundary layer clouds during the afternoon period and their dissipation after the sunset. In the winter season, the diurnal variation of mixing ratio peaks (7 g kg^{-1}) in afternoon hours (1200-1800 IST), aided by the westerly winds and strong upslope air flow which brings the moist air from the adjoining forest area to the site; manifested by formation of local clouds over the peak.

Large surface heating by the incoming solar flux during the daytime leads to enhancement of H which attains peak values (at 1200-1400 IST) of $353\pm 147\text{ W m}^{-2}$ in May. The diurnal mean upward transfer of H from surface to atmosphere during the spring season is 50 W m^{-2} . The peak H value occurs almost in phase with the incoming solar flux. The diurnal variation of e is significant only during April-May, when their peak values occur at $\approx 1500\text{-}1600$ IST; about 2 h after the peak values of the incoming shortwave flux and H are attained. This phase delay of the diurnal variations of e indicates the continued increase in turbulence generation by the increase in wind shear during the course of the day, even after the intensity of the thermals have started decreasing. On average, the magnitude of e is found to increase

from about $0.7 \text{ m}^2 \text{ s}^{-2}$ during calm wind periods to more than $2 \text{ m}^2 \text{ s}^{-2}$ when the winds are strong ($> 4 \text{ m s}^{-1}$) corresponding to the enhancement in the peak noon-time value of H is $\approx 50 \text{ W m}^{-2}$ from calm to strong wind conditions.

Weak synoptic wind conditions are highly appropriate to study the effects of mountain topography in exchange of momentum between surface and atmosphere, thermally generated mountain wind system, etc. A complete reversal in wind direction occurs during course of the day with a gradual change from easterly to westerly flow from 0900 to 1200 IST. During this evolutionary phase of mountain circulation due to heating of the slopes (with gradually changing wind direction, winds coming from southern sector, 120 to 240 degrees) the mountain winds interact with the regional westerly flow, resulting in higher turbulence and vertical exchange of momentum flux. On comparison of the average magnitudes of e and τ for the weak mean flow conditions of winter season and the similar quantities for strong synoptic conditions of spring season, it appears that the strength of synoptic flow does not have any major impact on the strength of momentum flux over the ridge, with the magnitudes of e during spring being twice of the magnitude for winter. Due to feeble intensity of incoming shortwave flux and weaker synoptic wind flow over the region, magnitude of H (mean peak value of $116 \pm 80 \text{ W m}^{-2}$ and seasonal mean value of $+17 \text{ W m}^{-2}$) is reduced by more than half of the magnitude during spring season.

Variations of the standard deviations of vertical wind normalized with friction velocity (σ_w/u_*) and temperature normalized with scaling temperature (σ_θ/T_*) as a function of stability parameter (z/L) indicate that they follow form of power law variation during unstable conditions, with an index of $1/3$ ($1/5$) for the former and $-1/3$ ($-1/2$) for the latter during spring (winter) season. The value of σ_w/u_* is found to be ~ 1.2 (0.2) during spring (winter) season for neutral stability conditions. The coefficients defining the above variations are found to be in agreement with those derived over flat terrain thus, MOST is applicable but only during the spring season, this could be due to higher mean wind speed (5.2 m/s) for the spring season. For the winter season wind speed is rather low (2.3 m/s), it thus appears that for the winter

season the turbulence intensity is too small for MOST to be appropriate for describing the turbulence characteristics. If artifacts due to terrain effects were present, the measured values of the integral characteristics of the scalars would have been substantially different for spring season (as suggested by observations reported in the literature).

This study provides rare experimental evidence (first of its kind over the Himalayan terrain) to show that the parameterization of surface layer turbulence characteristics over complex terrain is similar to those over flat homogeneous terrain, at least for the limited wind conditions(primarily moderate to strong winds).

Chapter # 5

Local boundary layer evolution and model validation

In this chapter the time-evolution of the Local Boundary Layer (LBL) for the first time over a mountain ridge at Nainital (79.5°E, 29.4°N, 1958 m amsl) in the central Himalayan region, using a Radar Wind Profiler (RWP) during November 2011 to March 2012, as a part of the Ganges Valley Aerosol Experiment (GVAX). We restrict our analysis to clear-sunny days, resulting in a total of 78 days of observations. The standard criterion of the peak in the signal-to-noise ratio (SNR) profile was found to be inadequate in the characterization of Mixed Layer (ML) top at this site. Therefore, we implemented a criterion of $SNR > 6$ dB for the characterization of the ML and the resulting estimations are shown to be in agreement with radiosonde measurements over this site. The daytime average (0500-1000 UTC) observed boundary layer height ranges from 440 ± 197 m in November (late autumn) to 766 ± 317 m above ground level (AGL) in March (early spring). The observations revealed a pronounced impact of mountain-topography on the LBL dynamics during March, when strong winds (> 5.6 m s^{-1}) lead to LBL heights of 650 m during nighttime. The measurements are further utilized to evaluate simulations from the Weather Research and Forecasting (WRF) model. WRF simulations captured the day-to-day variations up to an extent ($r^2 = 0.5$), as well as the mean diurnal variations (within 1-sigma variability). The mean biases in the daytime average LBL height vary from -7% (January) to +30% (February) between model and observations, except during March (+76%). Sensitivity simulations using a Mixed Layer model (MXL/MESSy) indicated that the springtime overestimation of LBL would lead to a minor uncertainty in simulated surface ozone concentrations. However, it would lead to a significant overestimation of the dilution of black carbon aerosols at this site. Our work fills a gap in observations of local boundary layer over this complex terrain in the Himalayas, and highlights the need for year-long simultaneous measurements of boundary layer dynamics and air quality to better understand the role of lower tropospheric dynamics in pollution transport.

5.1 Mixing layer height variations over the site

Through Radar wind profiler measurements, the mean diurnal variations of ML height during months covering the late autumn (November), winter (Dec-Jan-Feb) and early spring (March) has been analyzed. The impact of mountain topography on LBL evolution in the presence of strong winds during nighttime is investigated. Comparison of the day-to-day and diurnal variations in LBL height deduced from RWP measurements with simulations from a regional model (WRF) has been made to estimate model-observation biases along with the implications of these biases on air quality studies.

The main objectives of our study are:

- (1) To investigate the diurnal, and monthly variations in LBL evolution over the central Himalayas using RWP observations.
- (2) To evaluate boundary layer height with regional model (WRF) simulations, by using a setup similar to the one evaluated and extensively used over the Indian region (e.g. *Kumar et al.*, 2012a; *Kumar et al.*, 2012b; *Saranghi et al.*, 2014; *Ojha et al.*, 2016).
- (3) To assess the influence of model uncertainties in boundary layer height on air quality simulations, by conducting sensitivity runs with a mixed layer model (MXL/MESSy).

5.1 (a) Comparison between simultaneous measurements

Figure 5.1 and 5.2 depict the diurnal variability (24 hour cycle) of the RWP measured SNR profiles (15 minutes averaged) on two contrasting representative days in different months (with sensible heat flux of 17 and 50 W m⁻² during December and March). For each day, data from four radiosonde launches (approximate launch times of 0000, 0600, 1200 and 1800 UTC) were also available, which are used to investigate the profiles of potential temperature and specific humidity for comparison with ML height estimated from the RWP.

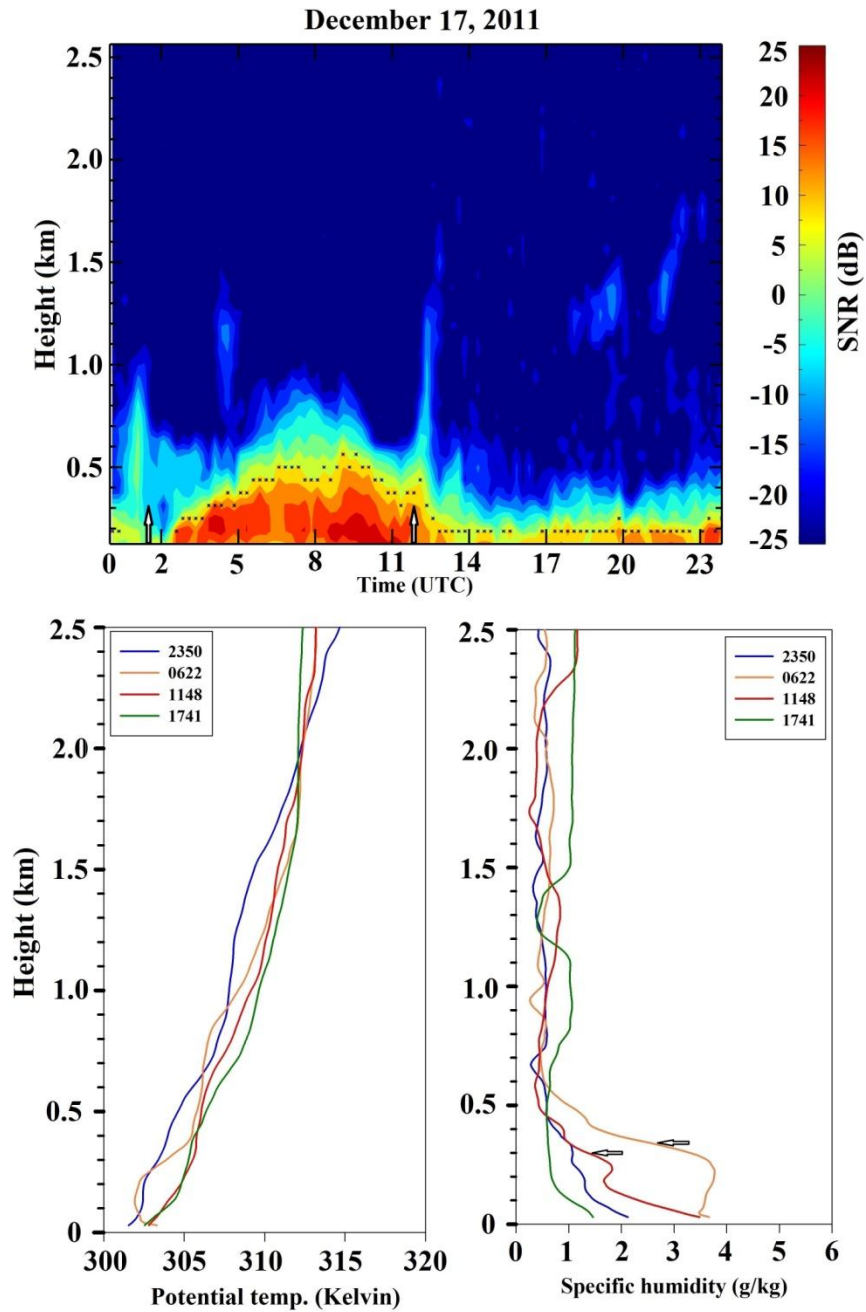


Figure 5.1: Mixed layer height for December 17, 2011. The upper panel shows range time intensity (RTI) plot of SNR (15 minute averaged) measured with RWP, the vertical arrows indicate the time of sunrise and sunset. The mixed layer height is marked by the black dots on the RTI plot. The lower panel shows the vertical profiles of potential temperature and specific humidity (horizontal arrows indicate the ML height estimated with specific humidity gradient maxima method) derived from the four radiosonde flights conducted during the day (marked with different colors).

A very clear smooth diurnal variation in SNR is observed on December 17, 2011, as illustrated in Figure 5.1; this feature is characteristic of a mountain LBL in the winter under calm wind conditions (wind speed $< 2 \text{ m s}^{-1}$); the evolution is seen from 0200 to 1300 UTC (i.e., 0730 h to 1830 h local time; UTC+5.5 h), attaining a peak of 500 m at noon (0700 to 0800 UTC). During nighttime (1300 to 0200 UTC) the LBL is extremely shallow in depth, and under the RWP lower detection range (i.e., 124 m). The specific humidity and potential temperature profiles also show a clear demarcation between the LBL and the free troposphere during daytime (0622 UTC), and the height of the inversion ($\sim 300 \text{ m}$) agrees quite well with the RWP-derived LBL height at the same time. The other radiosonde profiles (2350, 1148 and 1741 UTC) show stable potential temperature profiles, which is consistent with a stable (nocturnal) boundary layer.

Figure 5.2 shows the ML height evolution on March 15, 2012, which is considered as representative of the early spring season over the site, based on the mean diurnal variability of the ML during March. Two distinct growth phases of the ML are observed during the 24 hour cycle, with one starting at 0500 UTC and the other at 1300 UTC. The growth and decay in ML from 0500 to 1200 UTC is consistent with the diurnal cycle of incoming solar radiation. The peak height of the ML is above 900 m, and attained from 0800 to 1000 UTC. A second growth phase in the ML depth starts from 1300 UTC, and the ML remains stable from 1500 to 2030 UTC with ML height reaching up to approximately 700 m. The minimum ML height of 300 m is observed from 0000 to 0330 UTC.

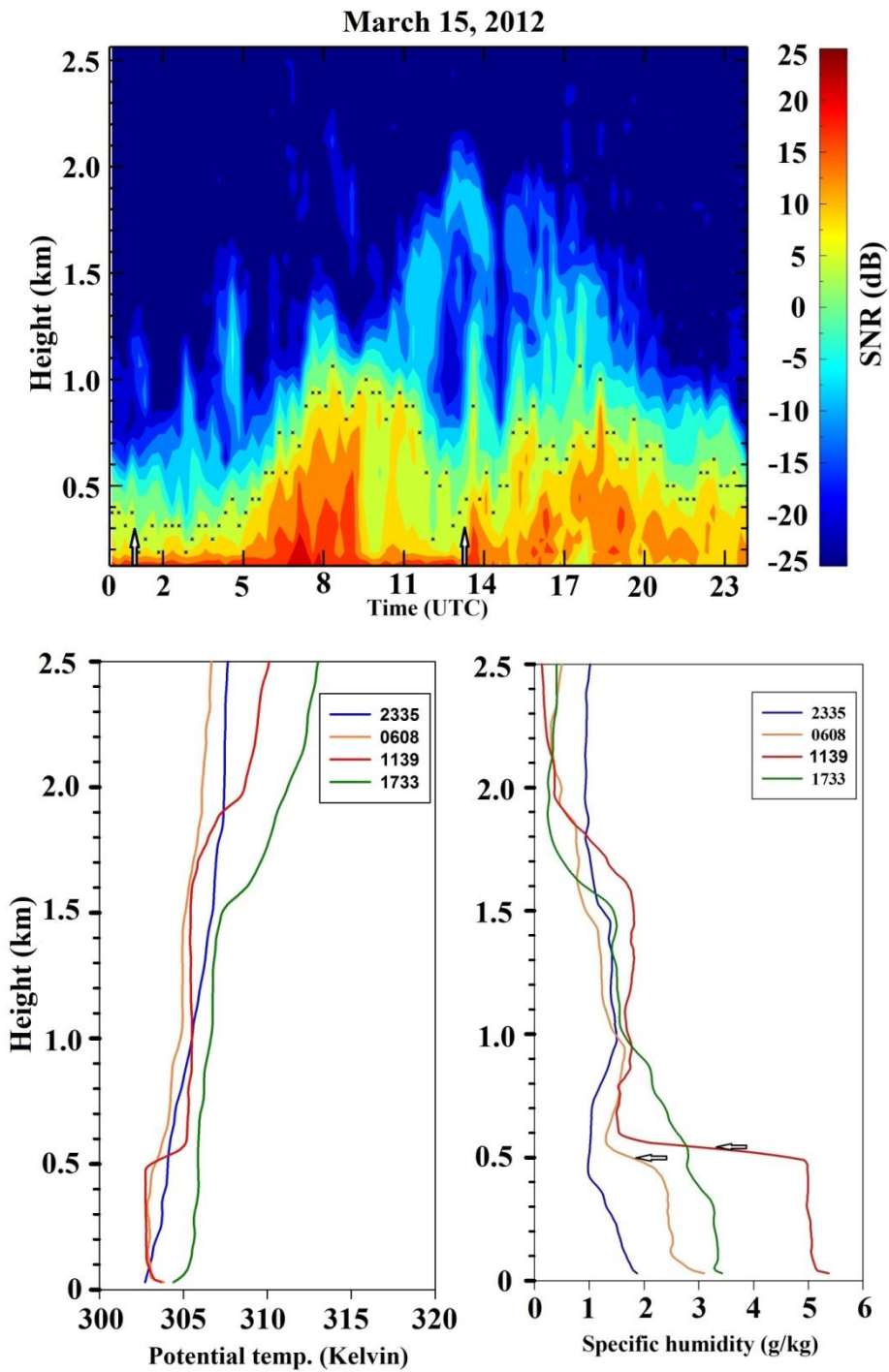


Figure 5.2. Same as Figure 5.1 but for March 15, 2012.

The vertical profile of specific humidity shows a strong inversion between 500 to 550 m, which is consistent with the estimated ML height derived from the RWP at the respective radiosonde launching time (0608 and 1139 UTC). However, a clear inversion in the potential temperature profile is seen only for the 1139 UTC ascent and a very weak gradient is also seen for the 0608 UTC profile, for both the profiles the inversion occurs at approximately 500 m pointing at a convective ABL. It is also notable from 1139 and 1733 UTC radiosonde launches, that inversion in the potential temperatures and specific humidity are taking place between 1500m and 2000m which could be due to advected residual layers.

5.1 (b) Diurnal variations

The comparison of monthly average diurnal variations in the ML height during the period from November 2011 to March 2012 is presented in Figure 5.3. The ML height was estimated only for the clear sunny days (without any large mesoscale activity), which were selected for each month through the sky condition log book that is maintained at the site and also by the visual inspection of sky camera videos. Table 1 shows the number of clear sky days for the different months.

A clearly defined diurnal variation in ML height is observed from November to February with minimum amplitudes during November and December, exhibiting a peak value of 500 m from 0700 to 0900 UTC. From January to March, the mean ML height shows overall a gradual increase, with peak values above 800 m. In general, the nocturnal boundary layer height remains below 300 m from 1600 to 0100 UTC. Towards the start of spring in the month of March, the ML height shows a distinct behavior with a mixing depth as high as 650 m during 1400 to 2200 UTC, which is attributed to the strong horizontal flow hitting the mountain (discussed in section 4.3), which gives rise to the lifting motions, and hence the rise of a few 100 meters in the mixing depth.

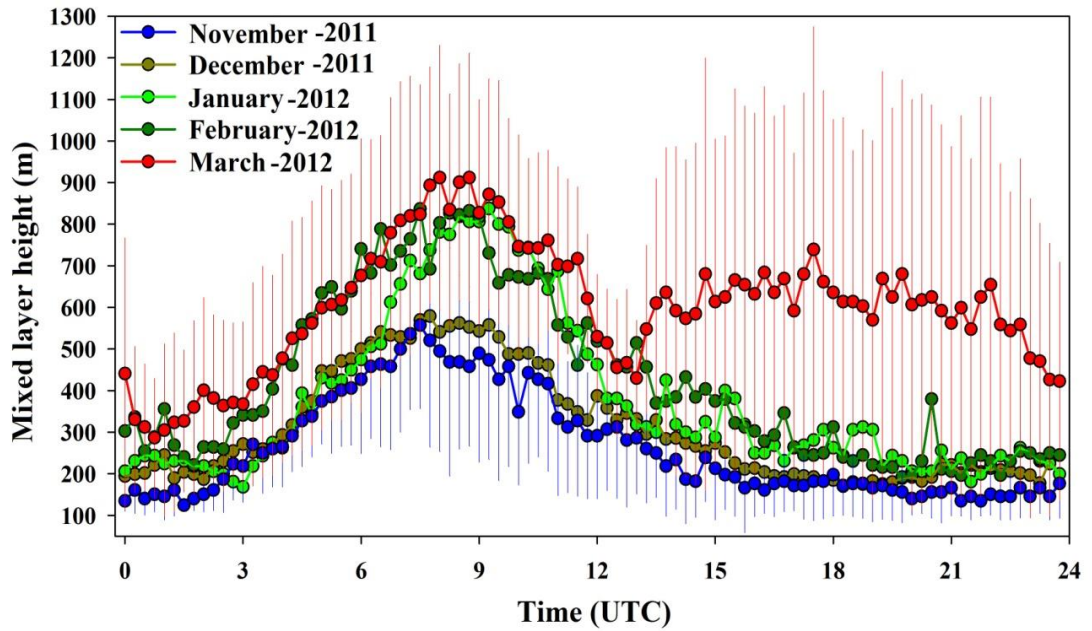


Figure 5.3: Monthly averaged mixed layer height determined from 15 minute averaged SNR profiles, measured with RWP. For the sake of clarity, variability is only shown for November and March months.

Table 5.1: RWP dataset used for studying the mixed layer height evolution.

Month	Total no. of days	Clears sky days
November-2011	16	12
December-2011	31	26
January-2012	31	10
February-2012	29	13
March-2012	31	17

5.1 (c) Impact of mountainous topography

The impact of mountain topography on LBL dynamics can be clearly identified by comparing the diurnal variability of the ML height in December and March. Figure 5.4 shows the diurnal variability in wind speed during December 2011 and March 2012 measured by a collocated AWS at the site.

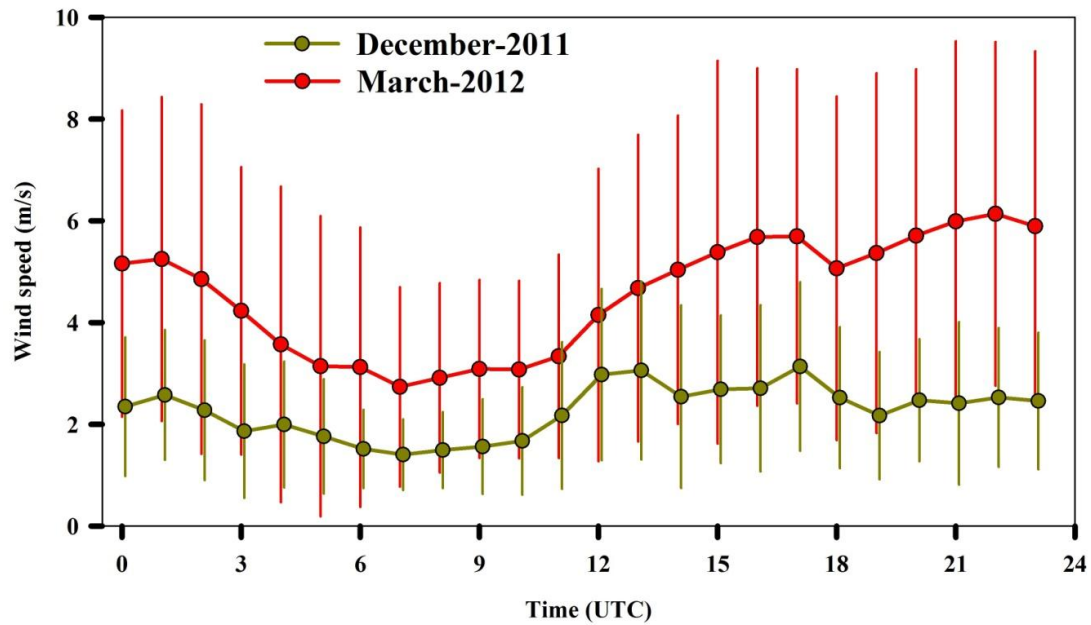


Figure 5.4: The monthly average diurnal variation in surface wind speed over the site during the clear sky days, selected for estimation of the mixed layer height as depicted in Fig. 3.

In December, when the winds are calm ($< 2 - 3$ m/s), the LBL growth starts around 0300 UTC. From then onwards, the ML height increases gradually and approaches a maximum of about 700 m in the afternoon, which appears to be in phase with the intensity of sunshine. ML height drops after 1000 UTC, and in the evening from 1300 UTC onward stays unchanged during nighttime (1500 to 0300 UTC). However, in March when the wind speeds are more than doubled, reaching values as high as 6 ± 3 m/s, the LBL settling in nighttime hours is hindered since such high winds cause significant wind shear, thereby generating turbulent eddies and increasing the vertical mixing of surface-layer air [Solanki *et al.*, 2016], leading to a second growth and decay phase in LBL depth from 1300 to 2330 UTC. This second growth phase can also be understood as the deepening of surface layer, transforming into residual layer [Henne *et al.*, 2014]. A decrease in wind speed is not observed from 2300 to 0300 UTC when the LBL decreases in depth, this could be attributed to the cooling of the surface beyond a certain extent, leading to the formation of a thin

stable nocturnal boundary layer decoupled from the residual layer above. High wind speeds near the surface are one of the characteristics of such stable layers.

5.2 Model Simulations

5.2 (a) Weather Research and Forecasting (WRF) model

This study uses the version 3.5.1 of the Weather Research and Forecasting (WRF) model to simulate the temporal variations of boundary layer height at Nainital during the study period. Meteorological fields from NCEP Final Analysis (FNL) data available at the spatial resolution of 1 degree and temporal resolution of 6 hours has been used to provide the initial conditions and the lateral boundary conditions in the model. Simulations were performed for two different spatial resolutions. The simulations from the coarser domain (15 km x 15 km) were used to provide the initial and boundary conditions for the higher resolution domain (5 km x 5 km). Both model domains and the topography of this region are shown in Figure 5.5. The errors in the simulated meteorology in the coarser domain were limited by nudging of the temperature, water vapor and horizontal winds with a nudging coefficient of 6×10^{-4} per second at all the vertical levels [Kumar *et al.*, 2012; Ojha *et al.*, 2016].

The cloud microphysics was represented by the Thompson microphysics scheme [Thompson *et al.*, 2008]. The longwave radiation has been calculated using the Rapid Radiative Transfer Model (RRTM) [Mlawer *et al.*, 1997] and shortwave radiation is calculated using the Goddard shortwave scheme [Chou and Suarez, 1994]. The surface layer has been parameterized using the Monin-Obukhov scheme [Janjic, 1996]. The Noah Land Surface Model, which utilizes the Unified NCEP/NCAR/AFWA scheme with soil temperature and moisture in four layers, has been used to parameterize the land surface processes [Chen and Dudhiya, 2001]. The planetary boundary layer dynamics were parameterized using the Eta operational Mellor-Yamada-Janjic (MYJ) scheme, which is based on a one dimensional prognostic Turbulent Kinetic Energy (TKE) scheme with local vertical mixing [Janjic, 2002]. The cumulus parameterization was based on the new Grell (G3)

scheme for the coarser domain, while it has been turned off for the nested domain. Detailed discussions on simulations using the WRF model, the chosen physics options and meteorological nudging, including evaluations over the Indian region, can be found in recent studies [Kumar *et al.*, 2012a; Kumar *et al.*, 2012b; Sarangi *et al.*, 2014; Ojha *et al.*, 2016]. Hourly model output from the nested 5 km x 5 km simulation has been used in the analysis.

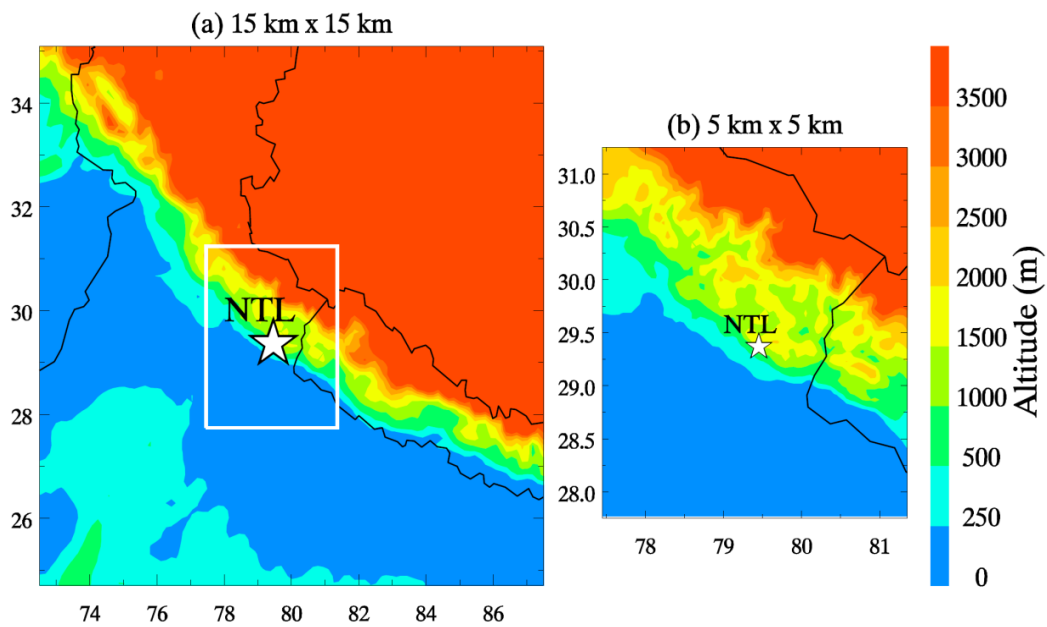


Figure 5.5: The WRF simulation domains used in the study are shown. The coarser domain (15km x 15 km) simulations are used to drive the simulation over the nested domain shown as white box in (a) and separately in (b). The geographical topography of the region and the location of measurement site Nainital (NTL) are also shown.

5.2 (b) MiXed Layer model (MXL/MESSy)

The implications of biases in the WRF simulated boundary layer dynamics, as compared to RWP measurements, on air quality simulations have been investigated by conducting sensitivity simulations with the MiXed Layer/ Modular Earth Submodel System model (MXL/MESSy, version 1.0; *Janssen and Pozzer, [2015]*). Although the BL dynamics are represented in a different way in MXL/MESSy than in WRF, we can use the former to obtain an insight into the effects of an overestimation of BL height on modeled chemical species concentrations. MXL/MESSy has been developed recently as a column model in the MESSy framework [*Joeckel et al., 2010*]. Within MXL/MESSy, the MXL submodel accounts for the dynamics of the convective boundary layer during daytime, by explicitly calculating BL-free troposphere exchange of scalars and chemical species through entrainment. Through the coupling of MXL with other MESSy submodels for processes that are relevant for atmospheric chemistry, MXL/MESSy can be used to evaluate the influence of BL dynamics on atmospheric chemistry. The mixed layer theory states that under convective conditions, strong turbulent flow causes perfect mixing of quantities over the entire depth of the ABL [*Vilà-Guerau de Arellano et al., 2015*]. Therefore, scalars and reactants in the convective boundary layer are characterized by a well-mixed vertical profile over the whole depth of the ABL. In MXL, the transition between the well-mixed BL and the free troposphere is marked by an infinitesimally thin inversion layer. In this study, chemical transformations are represented by the Mainz Isoprene Mechanism 2 (MIM2; *Taraborrelli et al., [2009]*). Black Carbon (BC) is treated as a passive tracer, which is appropriate at the short timescale (6 hours) of our simulations.

5.3 Comparison with model simulations

In this section, we utilize the ML height observations from the RWP to evaluate the simulation from a regional model (WRF) that has been used in previous studies for simulating the meteorology and regional air quality over Indian region (e.g. Kumar et

al., 2012; Sarangi et al., 2014; Ojha et al., 2016). We focus on the capability of the model, with a setup similar to the one used in aforementioned studies, in capturing the diurnal and day-to-day variability in mixing depth. Errors in simulating the mixing depth variations could lead to considerable uncertainties in the dispersion and mixing of the air pollutants over this region. For comparison, the model output has been obtained for the same selected clear-sunny days as the RWP measurements. Since WRF output is instantaneous hourly data, instantaneous hourly data has also been used from the RWP for comparison.

Figure 5.6 (a) shows the comparison of daytime (0500-1000 UTC) average boundary layer height from RWP measurements and WRF simulations from November 2011 to March 2012. The day-to-day variations in the daytime boundary layer height, as observed from the RWP, are captured by the model during late-autumn and throughout winter; however, the model shows significantly higher boundary layers towards the start of the spring (March). Figure 5.6 (b) shows a correlation analysis between model simulations and observations of daytime boundary layer height. Overall the model and observations are in reasonable agreement during the study period ($r^2 = 0.5$). The monthly statistics of the model observation comparison are given in the Table 5.2. The mean bias is the average difference (WRF - RWP) for the selected days of each month, and similarly the percentage bias is the percentage difference (WRF - RWP) normalized with respect to the mean RWP measurements.

Table 5.2: Daytime (0500 -1000 UTC) monthly mean and percentage bias between RWP measurements and WRF simulations.

Month	Observational mean (m)	Model mean (m)	Mean bias (m)	Percent bias (%)
November 2011	440±197	381±90	-59	-13.4
December 2011	500±245	415±112	-85	-17
January 2012	624±289	577±149	-47	-7.5
February 2012	686±268	890±439	+204	+29.7
March 2012	766±317	1350±664	+584	+76.2

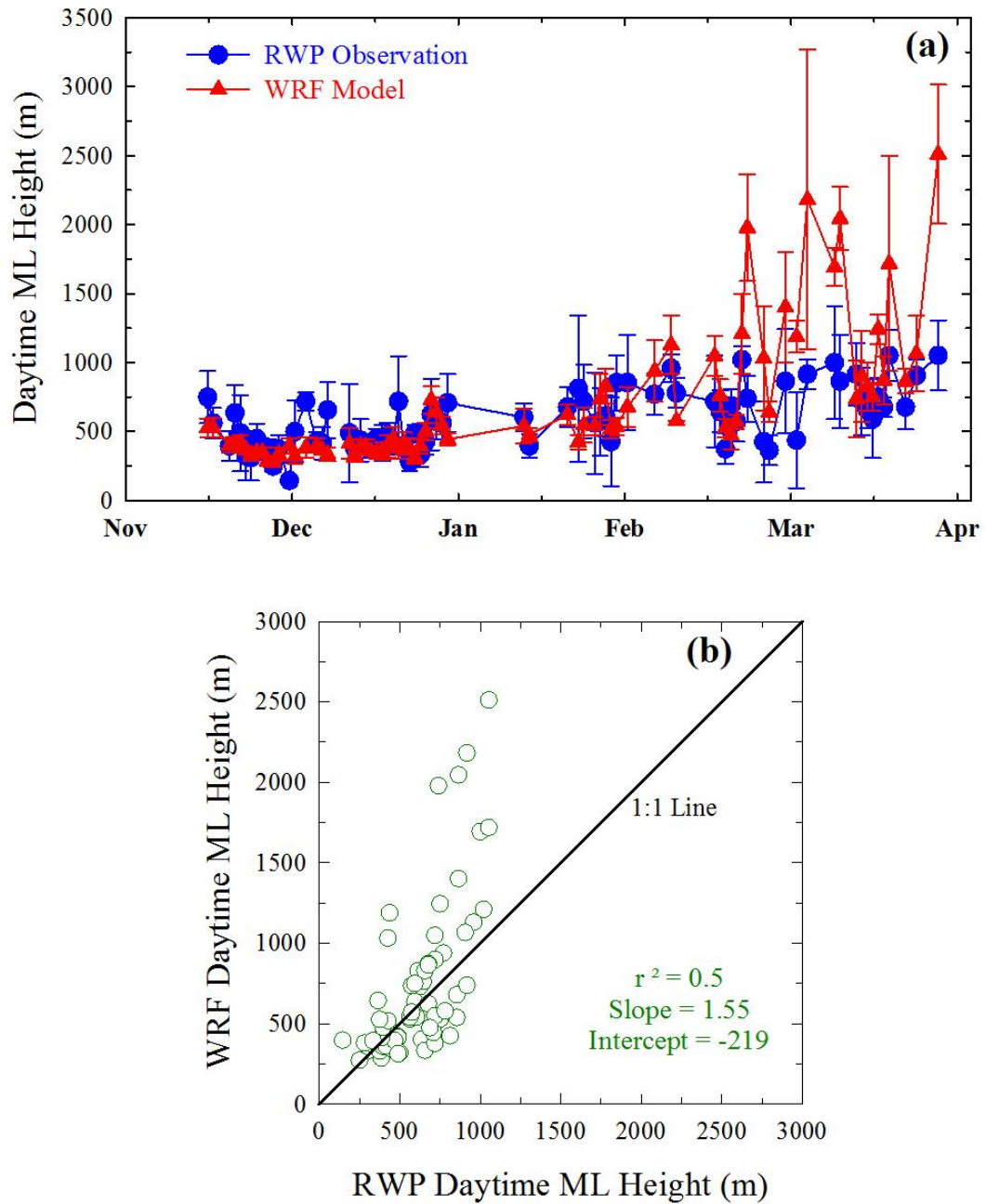


Figure 5.6: (a) A comparison of daytime (0500-1000 UTC) average boundary layer height from RWP measurements and WRF simulations at Nainital during the study period. Error bars represent 1-sigma standard deviation during daytime. (b) Correlation analysis between observational and model daytime boundary layer height. A 1:1 line is also shown.

On average, the noontime boundary layer height is slightly underestimated from November to January, by 47 to 85 m (7-17%). The variability (1-sigma standard deviation) in the modeled boundary layer height is also lower (90-149 m) than in the observations (197-289 m) during this period. However, during the transition from winter to spring (February), the variability and biases are observed to change. The model overestimates the boundary layer height by 204 m (30 %) and shows higher variability (439 m) than the observations (268 m), in contrast to the months of Nov-Jan. Model is seen to overestimate the daytime mean boundary layer height significantly (Table 5.2) during March (by 76.2 %), and the variability in the modeled boundary layer height is also seen to be more than that in the observations (317 m).

The mean diurnal variations in boundary layer height are compared between model and observations for all the months of the study period (Figure 5.7). The model simulated diurnal variations are in agreement with the measurements, as average daytime as well as nighttime values are generally within 1-sigma variation of each other. An appreciable disagreement between model and measurements is only seen towards the evening hours (1000 to 1200 UTC), when the boundary layer height shows a gradual decrease in the RWP measurements, whereas the model simulations exhibit a rapid decrease in the boundary layer height. In contrast to the period from November to February, the boundary layer height is overestimated throughout the day in March, with noontime mixing layer depth about two times higher than in the observations (Table 5.2). The overestimation of the noontime mixing layer depth by the model could be associated with the parameterization of boundary layer and land surface processes, uncertainties and/ or errors in simulating other meteorological variables, in addition to the effects of unresolved geographical topography. The effects of these uncertainties could become more prominent during the spring and/ or pre-monsoon due to intense solar radiation causing stronger boundary layer mixing, as compared to winter and autumn (Ojha et al., 2012; Sarangi et al., 2014). We suggest that a mixing layer depth about two times higher than in the measurements could lead to significant dilution or lead to additional entrainment when used in air

quality models. In the next subsection, we explore the possible implication of model biases in March above this site on air quality simulations using a 1-D mixed layer model.

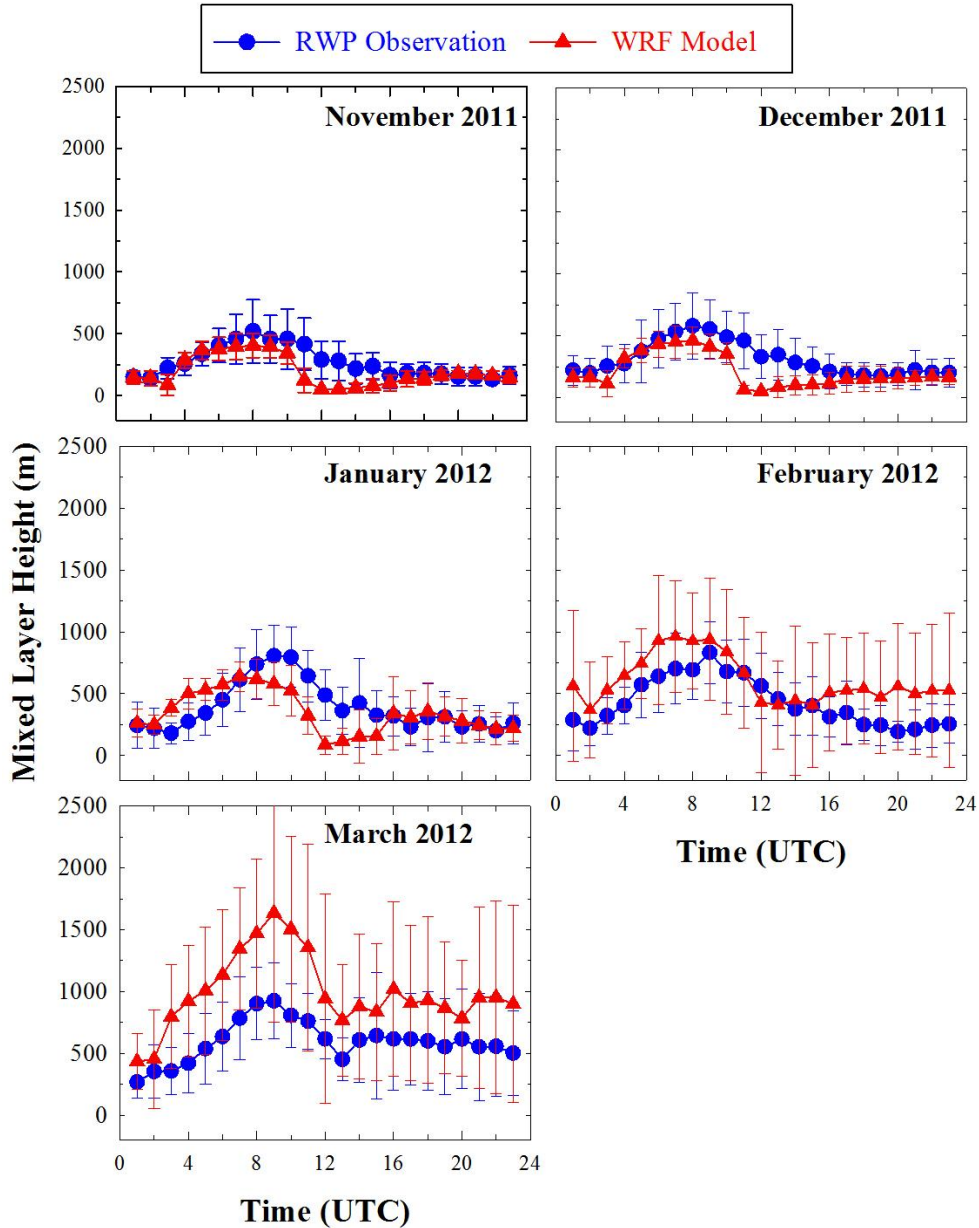


Figure 5.7: Comparison of the monthly averaged diurnal variations in the boundary layer height determined from RWP measurements and WRF simulations at Nainital during the study period.

5.4 Effects of boundary layer height overestimation on air quality simulations

In this section, we use MXL/MESSy, described in Section 5.2 (b) to investigate the influences of uncertainties in boundary layer height simulated by regional models on air quality simulations. For this purpose, we combined the effects of the boundary layer overestimation during March with the available information on vertical gradients and emissions at Nainital to assess the impact on two chemical tracers: Ozone (O₃) and Black Carbon (BC).

First, we set up MXL/MESSy to reproduce the observations of boundary layer height, potential temperature, specific humidity and wind speed for the representative day of March 15, 2012. Heat fluxes were prescribed to the model using typical values for March, based on our observations at this site using sonic anemometer measurements [Solanki *et al.*, 2016]. Initial and boundary layer conditions are given in Table 5.3. A set of simulations was performed (Figure 5.8) to identify the simulation that reproduces the observations best, which show a rapid boundary layer growth in the morning and the simultaneous increase of potential temperature and specific moisture. In addition to the surface fluxes of sensible and latent heat, which are the main drivers of boundary layer growth, large-scale subsidence and advection of cool and moist air were required to reproduce the observations. The assumption of large-scale subsidence in MXL/MESSy is consistent with the vertical downward wind speed of a few cm/s in the WRF simulations over the region.

Figure 5.8 shows the results from 4 simulations. The simulation which is closest to the observations (CTRL) includes both large-scale subsidence and advection of cool and moist air. The simulation without any subsidence leads to an overestimation (by ~ 250 m) of the maximum boundary layer height. The third simulation, in which there is no advection, overestimates LBL height and temperature and underestimates specific moisture. The final simulation, without advection and subsidence, yields an overestimation of the LBL height by 400 m.

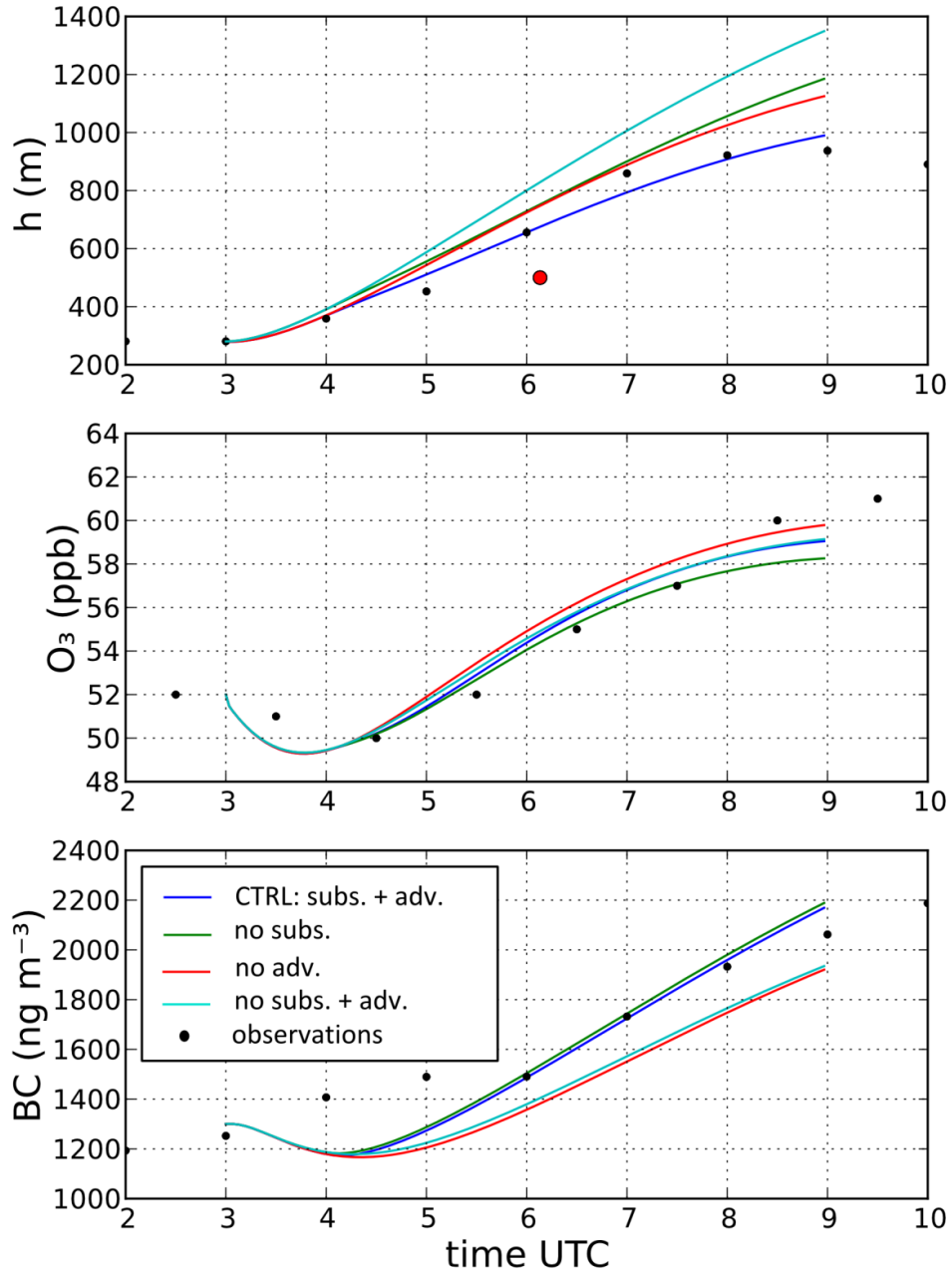


Figure 5.8: Diurnal variations in MXL/MESSy simulated (a) boundary layer height, (b) surface ozone, and (c) Black Carbon (BC) on 15th March 2012 for four different simulations. The CTRL simulation includes both subsidence and advection of cool and moist air. In the no subs. simulation subsidence is turned off, in the no adv. simulation advection is turned off, and in the no subs. + adv. simulation both subsidence and advection are turned off. In each panel, the black dots show observations made at the surface. In addition, the red dot in the upper panel shows the boundary layer height from a radiosonde measurement.

Table 5.3: The initial and boundary conditions in the atmospheric boundary layer (ABL) and free troposphere (FT) as used in MXL/MESSy. All initial conditions are imposed at 03:00 UTC. t is the time elapsed since the start of the simulation (s) and t_d the length of the simulation (s). The subscripts s and e indicate values at the surface and the entrainment zone, respectively.

Property		Value
Initial ABL height	h (m)	280
Subsidence rate	ω (s^{-1})	2×10^{-5}
Surface sensible heat flux	$w'\theta'_s$ ($K m s^{-1}$)	$0.24\sin(\pi t/t_d)$
Entrainment/surface heat flux ratio	$\beta = w'\theta'_e / w'\theta'_s$ (dimensionless)	0.2
Initial ABL potential temperature	$\langle\theta\rangle$ (K)	303.8
Initial FT potential temperature	$\langle\theta\rangle_{FT}$ (K)	304.0
Potential temperature lapse rate FT	γ_θ ($K m^{-1}$)	0.0065
Surface latent heat flux	$w'q'_s$ ($g kg^{-1} m s^{-1}$)	$0.11\sin(\pi t/t_d)$
Initial ABL specific humidity	$\langle q \rangle$ ($g kg^{-1}$)	2.0
Initial FT specific humidity	q_{FT} ($g kg^{-1}$)	1.9
Specific humidity lapse rate FT	q ($g kg^{-1} m^{-1}$)	-0.0010

The ozone gradient between the boundary layer and free troposphere is assumed to be 5 ppbv, as reported for the spring (MAM) season over this site based on ozonesonde observations [Ojha *et al.*, 2014]. Further, ozone-poor air is transported upwards from the valley during daytime [Ojha *et al.*, 2012; Sarangi *et al.*, 2014]. MXL/MESSy consists of two boxes and cannot explicitly account for upslope flows. Therefore, we mimic its effect by assuming a constant ozone loss at the bottom of the lowest box. The effect of variations in the boundary layer height on O_3 concentrations is found to be relatively small for the different simulations. The ozone mixing ratios differ by less than 2 ppb when the maximum boundary layer height is ~ 1350 m, as compared to the more realistic ~ 1000 m. This is due to the relatively small gradient in ozone mixing ratios across the LBL-free troposphere interface, which makes sure that entrainment of air from the free troposphere only dilutes the LBL ozone concentrations by a small fraction.

Unfortunately vertical profiles of black carbon are not available over Nainital site, and therefore measurements at another high altitude site Hanle (78.96°E, 32.78°N; ~ 4.5 km above sea level) in the Himalayan region were used to estimate the vertical gradient of BC. Average BC concentrations are reported to be 110 ng/m³ at Hanle as compared to 1340 ng/m³ for our site (2 km above sea level) during spring [Dumka *et al.*, 2010; Babu *et al.*, 2011]. The measurements show that BC concentrations increase during the day, which is attributed to the upward mixing of air masses from the nearby valley in the polluted Indo-Gangetic plain region (e. g. Dumka *et al.*, [2010]). This leads to a net increase in BC concentration during daytime, although entrainment of BC-poor free tropospheric air is also active. Emissions of BC were initially set at their values in the nearby valley, which were in the order of 10⁻¹² kg m⁻² s⁻¹, based on HTAP inventory [Janssens-Maenhout *et al.*, 2015]. The emissions were then tuned to obtain the best comparison with the observations and we found that a sinusoidal emission profile with a maximum of 5.5 x 10⁻¹² kg m⁻² s⁻¹ gave the best results.

Modeled BC concentrations are more sensitive to the variations in boundary layer height than those of ozone, because of a larger vertical concentration gradient. BC concentrations are simulated to be lower by ~300 ng/m³ in the case when the boundary layer height is ~ 350 m higher, due to missing effects of subsidence and advection. Note that with advection, we only mean advection of cool and moist air, and not advection of BC. The cool and moist air leads to a decrease of the BL temperature and an increase of the humidity. Consequently, the potential temperature and specific humidity gradient between the BL and the free troposphere increase, and therefore entrainment decreases [Janssen *et al.*, 2013]. For the same BC emissions, this means that more BC is trapped in a shallower BL and that it is diluted less with BC-poor air from the free troposphere. Subsidence acts to oppress the BL growth, but enhances entrainment [Janssen *et al.*, 2013]. Therefore, the BC concentration is diluted a little less in the simulation without subsidence.

Besides subsidence and advection, the conditions in the free troposphere can affect the BL dynamics as well. Therefore, the effect of boundary layer variations on BC at Nainital are further explored by conducting simulations for different gradients of potential temperature from boundary layer to free troposphere and for different lapse rates of the potential temperature in the free troposphere (Figure 5.9). Initial mixing ratio and surface emission fluxes are given in Table 5.4. We find that when the initial potential temperature gradient ($\Delta\theta_0$) is increased from 0.2 to 2.0 K, the BL growth is suppressed in the first hours of the simulation. Consequently, the BC emissions are concentrated in a shallower BL and therefore overestimated compared to the observations by 350 ng/m^3 (maximum). However, during the course of the day, the initial temperature barrier is overcome and the effect on the simulated BC concentration is reduced to 200 ng/m^3 at 09:00 UTC. Finally, the potential temperature lapse rate (γ_θ) determines the growth rate of the BL: if it is small, the potential temperature difference between BL and free troposphere grows less with increasing BL height than when it is large. When γ_θ is set to 0.002 K/m instead of 0.0065 K/m , as in the control experiment, the BL growth is much stronger and the BL height reaches 1650 m at 09:00 UTC, which is an overestimation of about 700 m , and comparable to the overestimation by WRF. Consequently, BC concentrations are diluted much more and are underestimated by up to 700 ng/m^3 . For a γ_θ of 0.009 K/m , the BL height is underestimated by about 150 m at maximum. The resulting error in the BC concentration compared to the control experiment is 300 ng/m^3 .

Table 5.4: Initial mixing ratio in ABL and FT, and surface emission fluxes of the reactants for MXL/MESSy runs. Species in the reaction mechanism that are not included in this table have an initial concentration of zero and no surface emissions.

For O_2 and N_2 we have imposed the values 2×10^8 and 8×10^8 ppb, respectively.

Initial mixing ratio (ppb)	O_3	NO	NO_2	BC (ng m^{-3})	CH_4	CO	CO_2
ABL	52	1.0	0.5	1300	1724	150	1300
FT	57	1.0	0.5	110	1724	150	110
Surface emission flux	-0.55 ppbm/s			$5.5 \times 10^{-3} \text{ ng m}^{-2} \text{ h}^{-1}$			

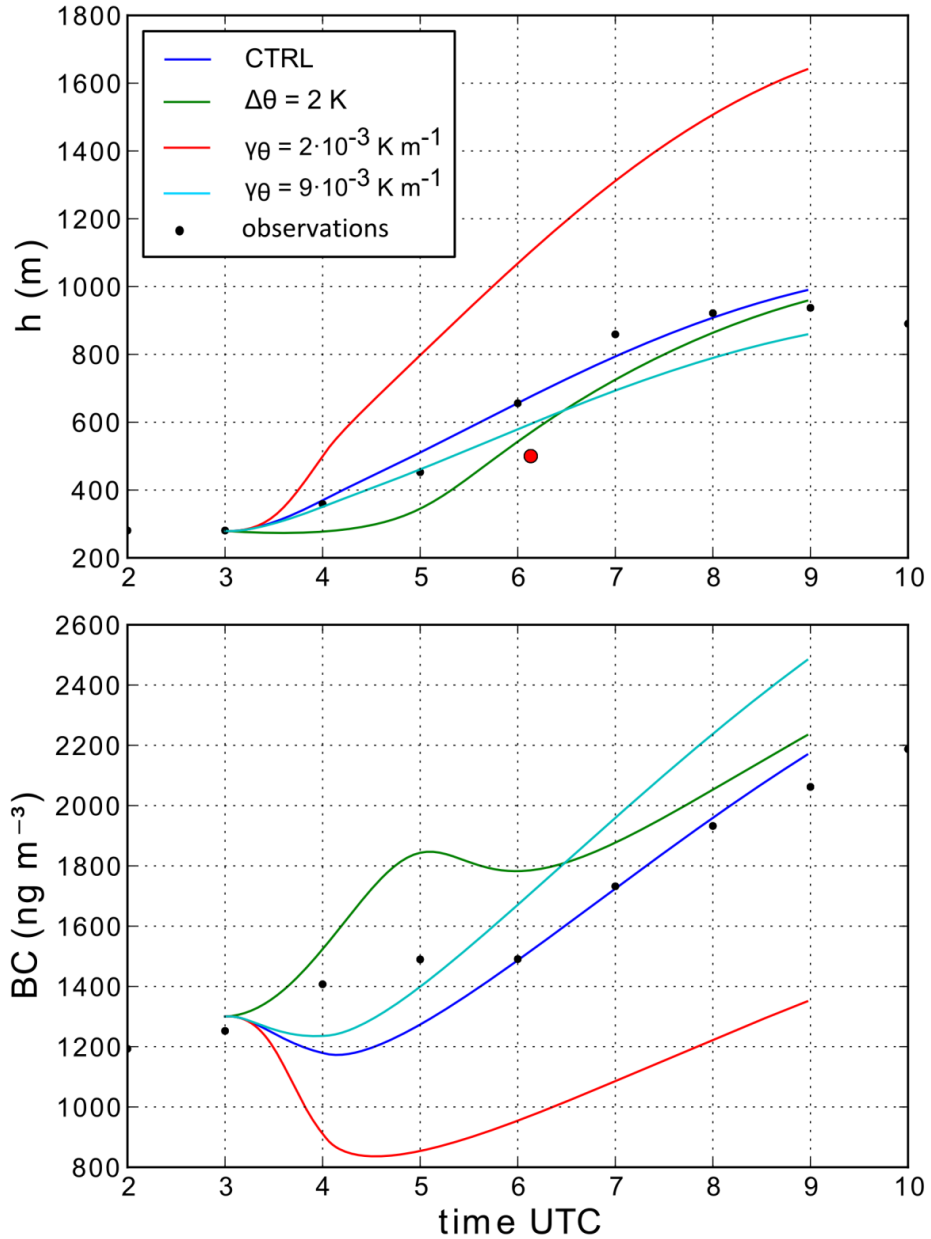


Figure 5.9: Sensitivity simulations of MXL simulated black carbon variations with different boundary layer dynamics. The blue line shows the control experiment (CTRL), the green line a simulation with the initial potential temperature jump ($\Delta\theta_0$) set to 2 K, the red line a simulation with a free tropospheric potential temperature lapse rate (γ_θ) set to 0.002 K/m and the turquoise line a simulation with γ_θ set to 0.009 K/m. In each panel, the black dots show observations made at the surface. In the top panel, the red dot shows the boundary layer height from a radiosonde measurement.

Our analysis suggests that an overestimation of boundary layer height has a minor effect on ozone concentrations (of less than 2 ppb), but a significant effect on BC concentrations (of ~300 up to 700 ng/m³). The effect of an overestimation of BL height on the concentration of a species is highly dependent on the vertical gradients of the species above our site. Ozone has almost equal concentrations in the BL and free troposphere above Nainital, but black carbon has sharp gradients above 2 km. We suggest that effects of boundary layer dynamics could be much higher in the nearby Gangetic basin, where the gradients will be much steeper due to strong surface sources and intense local photochemistry. More simultaneous measurements of boundary layer dynamics and trace species are highly desirable in the northern Indian region to understand the extent up to which boundary layer dynamics influences the air quality.

5.5 Summary and Conclusions

We presented the continuous measurements of ML height over a mountain peak in the central Himalayas from November 2011 to March 2012, obtained through state of the art instrumentation employed as a part of the GVAX intensive field campaign. RWP measurements of SNR are utilized for the first time over the central Himalayas to estimate mixing and boundary layer height and covered the mixing depth variations during late-autumn, complete winter and early spring. The criterion of SNR > 6 dB for identifying ML depth was found to be adequate, and yielded a reasonable comparison boundary layer height derived from the inversion in potential temperature profiles obtained from radiosonde launches. The results show that the LBL over the site undergoes clear diurnal variations in all months from November to February, attaining peak heights between 0700 to 0800 UTC and remaining stable during the night, having minimum height (1800 to 0100 UTC). However, in the month of March the LBL continues to decrease in depth till 1330 UTC (falling up to 500 m) and afterwards rises again and remains stable at 650 m from 1400 to 2200 UTC. The strikingly larger depth of the LBL can be attributed to the strong winds

over the site during the night, which results in strong orographic lifting over the site. The study re-establishes the fact that RWP gives the better temporal estimation of ML heights compared to balloon borne and other such measurements. As RWP provides the volume scattering from the turbulent scales to which radar is sensitive and receives backscatter power over a larger aperture that provides insight into the LBL dynamics through continuous measurements with fine vertical resolution.

The observations are further utilized to evaluate high resolution simulations from a regional model (WRF). WRF-simulated day-to-day variations in the noontime boundary layer height were in reasonable agreement with the RWP observations ($r^2 = 0.5$). Additionally, the monthly average diurnal variations in boundary layer height from model and observations are generally within the 1-standard deviation variability. The mean biases in the daytime boundary layer height are estimated to be -7 to +30 % from November to February, but a large overestimation of ~76 % was seen towards the early spring (March). Our study fills a gap by providing a continuous observational dataset on the boundary layer dynamics over a geographically complex and environmentally important region of the central Himalayas. We found that while the regional model simulates the boundary layer evolution well during the post-monsoon season and winter, it shows large biases towards spring. This highlights the need to extend boundary layer observations to entire seasons of spring and summer.

Sensitivity simulations using MXL/MESSy were conducted to assess the impact of the uncertainty in ML height on air quality simulations, thereby providing insight in the influence of subsidence and advection processes on boundary layer dynamics over the site. We analyzed effects on two chemical tracers: ozone and black carbon. We find a relatively small effect (~2 ppb) of overestimated boundary layer height during March on surface ozone concentrations at Nainital. In contrast, significant dilution was found in case of black carbon (by 300-700 ng/m³), due to the overestimation of boundary layer height.

It should be noted that spring is a period of strong winds near the surface, maximum solar radiation and the highest pollution loading over this region, which is followed by torrential rains of the monsoon season. Since regional photochemistry and convective mixing are intensified during spring over the Gangetic basin, we suggest that year long measurements with instrumentation such as RWP are highly desirable to understand the influence of boundary layer dynamics on the mixing of pollution.

Chapter # 6

Summary, conclusions and future scope

This final chapter summarizes the results presented in Chapter 3, 4 and 5; providing conclusive remarks on what has been achieved from them, along with a perspective on the relation amongst them and the significance of this study in totality. The objective of this thesis has been to understand the association between aerosol distribution and meteorology over mountainous terrain, this chapter brings out the understanding which has been developed on the problem. The work carried out in this thesis is summarized and concluded here; along with the brief scope for future work in the direction of this thesis.

6.1 Aerosol distribution

The Himalayas remain largely unexplored in terms of information on aerosol vertical distribution, this thesis presented for the first time intensive measurement of aerosol vertical distribution over a regional representative site in the central Himalayas, for the entire seasonal cycle (March 2012 to May 2013), along with one case study on long range transport as well. The LiDAR ratio, which proves to be of vital importance in retrieval of aerosol vertical profiles, is generally assumed to be constant, but for the measurements presented in this thesis an intricate methodology was incorporated for determining a distinct LiDAR ratio for each day of observation. The observation revealed the day to day variability in aerosol distribution and distinct seasonal variations, primarily up to 5 km AMSL over the site. The seasonal mean extinction coefficient for the spring and winter season is found to be 124 ± 138 and $7 \pm 8 \text{ Mm sr}^{-1}$ for the spring and winter season respectively. The higher aerosol loading over the site

during spring season is primarily due to intense solar heating and convection, which leads to in planetary boundary layer height (over the adjoining IGP region) reaching the altitude of the site and even higher, thus leading to stronger aerosol loading up to an altitude of 3 km AMSL; above which long-range transport is the major contributor to aerosol loading. During the autumn season the aerosol loading is drastically reduced (extinction coefficient of $14 \pm 19 \text{ Mm sr}^{-1}$) as a result of heavy monsoon rains, the most efficient removal mechanism of aerosols. Shallow boundary layer and cold flows from the high Himalayas, lead to the confinement of aerosols over the foothills and the IGP in the winter season, making the atmosphere above the site free from influence of any local sources of aerosols in the adjoining plains.

Ground based measurements provide time evolution of measurements over a fixed location, however, satellite measurements have an advantage of providing a spatial coverage on quantity of interest, in this thesis a combined study has been made with ground and space borne measurements, providing a rather comprehensive understanding of the aerosol vertical distribution over the Himalayan region. In this context, validation of CALIPSO satellite measurement with ground-based LiDAR measurements of aerosol vertical distribution has been made, thus estimating bias in satellite measurements over the Himalayan region for the first time. The study comprised of 37 cases for comparison, with temporal mismatch of less than 18 hours and spatial mismatch of up to 220 km. The bias for the spring, autumn and winter season comes out to be +18%, +22% and +32% respectively. Strong discrepancies between the aerosol vertical distributions obtained with ground based and satellite measurements for altitude below 3 km AMSL were attributed to the boundary layer dynamics, inhomogeneity in aerosol distribution over mountainous topography and probably to lesser extent due to spatial mismatch of measurements. The estimated biases will enable extensive use of CALIPSO satellite aerosol profile retrievals over the Himalayas.

In the spring season, stronger aerosol loading in the vertical column and formation of elevated aerosol layers is generally observed over the site. A major contribution to higher aerosol loading during spring season comes from long range transport of aerosol

from dry regions located to the west and northwest of the site. A case study presented in this thesis provides details on the elevated aerosol layer which was observed over the site during 22 to 24 March 2012. Through MISR satellite measurements and back-air trajectory analysis the source of the elevated aerosol layer was found to be located over dry arid regions of Saudi Arabia and North Africa.

6.2 Mountain meteorology

The mountains envisage a wide range of meteorological phenomenon, highly specific to location, slope angle and orientation. The measurements of three wind components and temperature taken at two levels above ground over the site are of profound significance. The importance of these measurements can be ascertained by two facts, understanding of surface layer characteristics over ridges and mountain-tops is least explored, however most of the observatories in mountainous terrain are situated on mountain peaks in order to make regional representative measurements. The surface layer characteristics explored in this thesis for the winter and spring season, revealed the details of the highly contrasting feature; these results proved to be of profound importance in understanding the spatio-temporal variations of trace species and aerosols made over the site.

The analysis of aerosol vertical distribution measurements demonstrated significant variations in aerosol distribution from 0 to 1 km above ground surface of ridge and extreme contrast in aerosol loading between spring and winter season, which lead to detailed understanding of surface layer characteristics in these two antithetic seasons. Through the fast response (25 Hz) sonic anemometer measurements detailed analysis of surface layer characteristics over the site during spring (March – May 2013) and winter (November – January 2014) season has been made. In the spring season regional wind are very strong (10 m/s) suppressing the mountain wind system (however a small change of 30 degrees in wind direction in observed in peak noontime hours), whereas under low (2 m/s) synoptic wind conditions of winter season a complete reversal of

wind direction is observed which indicates the dominance of mountain wind system. A consistent diurnal pattern of maxima in the mixing ratio in the afternoon hours is observed for both the seasons, with this rise in water vapour content often resulting in formation of boundary layer clouds over the site. This phenomenon is attributed to the topography of the site (convergence of moist air above the ridge) and the advection of moist air from the heavily forested region on the western slope. Planar fit method has been applied for converting the actual measurements (vertical with respect to gravity) into terrain following coordinate system (vertical with respect to underlying ground surface) before estimation of turbulence parameters. Diurnal variations of turbulent kinetic energy, fluxes of heat and momentum have also been investigated. Strong wind shear during nighttime emerged as a consistent feature of the site. These findings are encouraging and prompting towards more detailed campaign measurements on ABL dynamics over the region in near future.

For the first time measurements of the turbulent kinetic energy(e), fluxes of heat and momentum has been made for this regional representative site in the central Himalayas. The understanding of the parameters is useful for understanding the interaction of the lowest part of atmosphere with the Earth's surface. During the winter season the peak values of sensible heat flux (H) was found to be $116 \pm 80 \text{ W m}^{-2}$. For the month of May 2013 the peak value of H comes out to be $353 \pm 147 \text{ W m}^{-2}$, larger than those observed for some of the tropical region. The mean magnitude of H increases by three times from winter to spring season, with a seasonal mean of 17 and 50 W m^{-2} respectively. However, the peak noon values of incoming shortwave radiation are in the range of $700 - 800 \text{ W m}^{-2}$ for the winter season and vary in between $1000 - 1100 \text{ W m}^{-2}$ for the spring season. Thus, a three-fold increase in H can be attributed to a lesser extent to increase in incoming solar radiation, with a major contribution from orographic influences under strong synoptic conditions of the spring season. The magnitude of e is 0.62 and $1.46 \text{ m}^2 \text{ s}^{-2}$ for the winter and spring season respectively. However the magnitude of momentum flux is almost similar for both the season (approximately 0.09 Nm^{-2}).

Variability in vertical winds over a mountain-top site is of prime importance in understanding temporal variation of aerosol and trace gases measurements. In this thesis for the first time diurnal variation in vertical component of wind speed for the spring and winter season have been studied. Upward (upslope) vertical wind are observed from 0900 IST onwards, attaining maximum magnitude of 0.2 to 0.3 m s⁻¹ in noontime (1300 IST) and the reversal to downward (down slope) vertical wind sets in from 1600 IST in winters and 1800 IST in spring season. The mean magnitude of upslope and down slope flows is weaker during winter season and being half of the magnitudes observed during spring season.

Variations of the standard deviations of vertical wind normalized with friction velocity (σ_w/u_*) and temperature normalized with scaling temperature (σ_θ/T_*) as a function of stability parameter (z/L) over a mountainous topography confirmed the applicability of Monin-Obukhov similarity theory (MOST) for the site, however for the spring season the intensity of turbulence is very weak and thus the variations are found to be outside the limit of the applicability of MOST as suggested by *Foken and Wichura* [1996]. For the spring season, the near neutral condition value of σ_w/u_* is found to be comparable to those reported by *Moraes et al.* [2005] and *Panofsky and Dutton* [1984], whereas for the winter season this value comes out to be 0.2. These findings further authenticate the analysis of surface layer characteristics over the site, since if artefacts due to terrain were present, the measured values of the integral characteristics of the scalars would have been substantially different (as suggested by observations reported in the literature). This study provides rare experimental evidence (first of its kind over the Himalayan terrain) to show that the parameterization of surface layer turbulence characteristics over complex terrain is similar to those over flat homogeneous terrain, at least for the limited wind conditions.

6.3 Local boundary layer evolution

Evolution of planetary boundary layer over the course of a day over homogeneous terrain is a well established phenomenon [Stull, 1988]. In contrast, the understanding of boundary layer evolution over complex mountainous topography is poor, still an evolving field with exciting observations leading to more detailed understanding of the interaction between earth's surface and atmosphere above. In this thesis, a special case of boundary layer evolution of a mountainous ridge in the central Himalayas was presented, using the measurements made with a Radar Wind Profiler (RWP) which is considered to be one of the best tools for understanding the state of atmosphere close to the ground surface. The diurnal evolution of boundary layer over mountainous terrain is intricately associated with the topography of the site, slope angle, land cover, strength and orientation of large-scale prevailing flow; hence the term "local" is essential to characterize the boundary layer variations. This thesis presented quality measurements of local boundary layer (LBL) evolution over the site for the highly contrasting winter and spring season (November 2011 to March 2012).

The standard criterion of prominent peak in the SNR profile for mixed layer (ML) height estimation was found to be inadequate, leading to a new criterion of ML classification. According to the criterion the region of $SNR > 6$ dB was characterized as ML, with the criterion being pre-checked for compatibility with radiosonde profile estimated ML from noontime-to evening hours.

The monthly mean variations in ML height were estimated, which showed similar diurnal variation in daytime for the observation period. The peak height is attained at 0900 UTC (noontime), being less than 500 m in November and December, about 650 m in January and February, and more than 750 m for March. One of the interesting findings of this study on LBL diurnal variations was the evidence of orographic influence on mixed layer height during nighttime in the spring season. The strong wind flow leads to second evolutionary phase of LBL with altitude comparable to the daytime mixed layer height. The measurements reinforce the high wind shear measurements in the surface layer which lead to strong mixing over the site, which

might as well be characteristics of wind flow over mountain ridges under strong synoptic wind flow conditions.

The ML height derived from RWP observations is further utilized to evaluate high resolution (5 km x 5 km) WRF simulations of ML height. The monthly average variations of ML (from model) were found to be in agreement (within 1 standard deviation variability) with RWP measurements, except for the month of March when the model simulations largely overestimate ML height. The mean bias in daytime ML height estimation is found to be - 7 to + 30% from November to February, and + 76 % for March. The variations in the mean bias highlight the need for extending the analysis for the entire seasonal cycle over the site through such yearlong measurements in future.

Additionally, MXL/ MESSy model was employed to assess the implications of the uncertainty in ML height estimations on the air quality simulations of ozone and black carbon over Nainital. This analysis revealed the various processes involved in the boundary layer dynamics over the site, along with the relative significance of various control factors. Due to overestimation of ML height the impact on surface ozone concentration was found to be milder magnitude (~ 2 ppb), whereas the impact on black carbon turns out to be quite significant with a dilution of 300 – 700 ng m⁻³. These findings further elevate the need of intense simultaneous measurements of air pollutants and boundary layer parameters over the site, especially for the entire spring season.

6.4 Achievements and Future scope

In this thesis, first time quality analysis of aerosol vertical distribution, surface layer characteristics and evolution of local boundary layer were presented, primarily based on measurements taken over a regional representative site in the central Himalayas. Moreover an understanding of the association between air pollutants and meteorology over complex mountainous topography has been developed, with highlights being strong variations in aerosol vertical distribution, contrasting surface layer

micrometeorological conditions and the understanding of local boundary layer evolution. More detailed work in the direction of this thesis would be certainly significant and desirable; the inception for some of the future studies is as follows:

- ❖ In this thesis, seasonality of aerosol vertical distribution over the region has been analyzed in detail. In future, this analysis can be incorporated in the understanding of radiative impact of aerosol along the vertical column over the Himalayas, for the purpose ground based and satellite measurements of aerosol vertical distribution can be incorporated. Through ground based measurements temporal variation can be understood, whereas with satellite measurements spatial coverage over the Himalayas can be attempted, which will be of paramount importance in quantifying the implications of pollution on the climate and hydrological cycle of the Himalayas.
- ❖ The aerosol vertical distribution, dispersion and radiative effects on atmosphere are associated with surface layer characteristics and LBL dynamics. In this thesis, the association between air pollutants and meteorology over the site has been studied and it has been concluded that the heavy aerosol loading in vertical column is strongly influenced by the turbulent characteristics of the surface layer over the site and on a larger scale by the LBL dynamics which is under strong orographic influences during nighttime. These findings need more intensive studies through dedicated campaigns in future during spring and winter season, to further improve the understanding of air-pollution meteorology over the complex mountainous topography of the Himalayas.
- ❖ Surface energy budget plays a major role in boundary layer evolution, with a need for the understanding of various terms involved in making the net surface heat flux. In this thesis, evolution of sensible heat flux over the site in two contrasting seasons has been studied. In future, establishing measurements of radiative fluxes (shortwave / longwave), soil heat flux, and atmospheric fluxes (sensible and latent heat flux) will be of prime significance towards understanding of surface energy budget over the

site, which will ultimately be essential for the improvement of modeling studies over the region.

- ❖ During this thesis, an interesting aspect of orographic influences on LBL height during spring season were discovered and in future detailed understanding of orographic influences on the wind flow over the site through vertical velocity measurements of RWP and surface layer turbulence characteristics will provide better understanding of the interaction between atmosphere and the mountainous surface. Such an understanding can be of prime importance in understanding variations in aerosol and trace gases measurements over the site.
- ❖ WRF model simulations of boundary layer height and their comparison with RWP measurements, revealed interesting results providing insight into the various atmospheric processes controlling LBL variations over the site. The bias in model simulations was rather smaller for the winter season, however for the spring season a large over estimations of LBL height elevates the need for extended observations for the entire spring and pre-monsoon season. In future, with the current understanding of ABL dynamics over the central Himalayas, the modeling studies can be initiated in context with high resolution modeling of boundary layer dynamics over the complex mountainous terrain of the central Himalayas. With observational evidences identification of better PBL schemes for modeling studies can be made, which can thus improve our understanding of the boundary layer dynamics over the central Himalayas.

Blank page

References

- Adler, B., and N. Kalthoff (2014), Multi-scale transport processes observed in the boundary layer over a mountainous island. *Bound. Layer Meteorol.*, 153, 515–537. doi: 10.1007/s10546-014-9957-8.
- Anderson, T. L., R. J. Charlson, D. M. Winker, J. A. Ogren, and K. Holm´en (2003), Mesoscale Variations of Tropospheric Aerosol. *J. Atmos. Sci.*, 60, 119–136.
- Angevine, W., A. White, and S. Avery (1994), Boundary-layer depth and entrainment zone characterization with a boundary-layer profiler. *Bound. Layer Meteorol.*, 68, 375–385.
- Ansmann, A., (2006), Ground-truth aerosol lidar observations: can the Klett solutions obtained from ground and space be equal for the same aerosol case? *Applied Optics*, 45, 3367–3371.
- Arya, S. P., (2001), Introduction to Micro-meteorology. 2nd Ed, *Academic Press*, 420 pp.
- Aubinet, M., T. Vesala, and D. Papale (eds) (2012), Eddy Covariance: A Practical Guide to Measurement and Data Analysis. *Springer*, Dordrecht, 438 pp.
- Babu, S. S., et al. (2011), High altitude (~4520 m amsl) measurements of black carbon aerosols over western trans-Himalayas: Seasonal heterogeneity and source apportionment. *J. Geophys. Res.*, 116, D24201, doi: 10.1029/2011JD016722.
- Badarinath, K. V. S., Shailesh Kumar Kharol, and Anu Rani Sharma (2009), Long-range transport from agriculture crop residue burning in Indo-Gangetic Plains—A study using LIDAR, ground measurements and satellite data. *J. Atmos. Solar-Terr. Phys.*, 71, 112–120.
- Barr, S., and M. M. Orgill (1989), Influence of external meteorology on nocturnal valley drainage winds. *J. Appl. Meteorol.*, 28:497-517.

- Basha, G., and M. V. Ratnam (2009), Identification of atmospheric boundary layer height over a tropical station using high-resolution radiosonde refractivity profiles: comparison with GPS radio occultation measurements. *J. Geophys. Res.*, 114: D16101, doi: 10.1029/2008JD011692.
- Bhavani Kumar, Y., (2006), Portable lidar system for atmospheric boundary layer measurements. *Journal of Optical Engineering*, 45(7): 076201.
- Bianco, L., I. V. Djalalova, C. W. King, and J. M. Wilczak (2011), Diurnal evolution and annual variability of boundary-layer height and its correlation with other meteorological variables in California's Central Valley. *Bound. Layer Meteorol.*, 140: 491-511,doi 10.1007/s10546-011-9622-4.
- Bonasoni, P., P. Cristofanelli, A. Marinoni, E. Vuillermoz, and B. Adhikary (2012), Atmospheric pollution in the Hindu Kush–Himalaya region: evidence and implications for the regional climate. *Mt. Res. Dev.*, 32, 468–479.
- Cattrall, C., J. Reagan, K. Thome, and O. Dubovik (2005), Variability of aerosol and spectral lidar and backscatter and extinction ratios of key aerosol types derived from selected Aerosol Robotic Network locations. *J. Geophys. Res.*, 110, D10S11, doi:10.1029/2004JD005124.
- Charlson, R. J., S. E. Schwartz, J. M. Hales, R. D. Cess, J. A. Coakley, Jr., J. E. Hansen, and D. J. Hoffmann (1992), Climate forcing by anthropogenic aerosols. *Science (USA)*, vol. 255, Issue 5043, pp 423-430.
- Chen, F., and J. Dudhia (2001), Coupling and advanced land surface hydrology model with the Penn State-NCAR MM5 modeling system, Part I: Model implementation and sensitivity. *Mon. Weather Rev.*, 129, 569–585.
- Chen, X., J. A. Anel, Z. Su, L. de la Torre, H. Kelder, J. van Peet, and Y. Ma (2013), The deep atmospheric boundary layer and its significance to the stratosphere and troposphere exchange over the Tibetan plateau. *PLoS ONE*, 8(2): e56909, doi:10.1371/journal.pone.0056909.

- Chou, M. D., and M. J. Suarez (1994), An efficient thermal infrared radiation parameterization for use in general circulation models. *NASA Tech. Memo.*, 104606, 85 pp.
- Coulter, R. L., (1979), A comparison of three methods for measuring mixing-layer height. *J. Appl. Meteorol.* 8, 1495–1499.
- Coulter, R. L., and D. H. Holdridge (1998), A procedure for the automatic estimation of mixed layer height. *Proc. Eighth Atmospheric Radiation Measurement (ARM) Program Science Team Meeting*, Tucson, AZ, Department of Energy Office of Energy Research, 177–180.
- De Wekker, S. F. J., D. G. Steyn, and S. Nyeki (2004), A comparison of aerosol-layer and convective boundary-layer structure over a mountain range during STAAARTE'97. *Bound. Layer Meteorol.*, 113, 249–271. doi: 10.1023/B:BOUN.0000039371.41823.37.
- De Wekker, S. F. J., and M. Kossmann (2015), Convective Boundary Layer Heights Over Mountainous Terrain—A Review of Concepts. *Front. Earth Sci.*, 3:77. doi: 10.3389/feart.2015.00077.
- Draxler, R. R., and G. D. Rolph (2003), HYSPLIT (Hybrid Single-Particle Lagrangian Integrated Trajectory) model, Air Resour. Lab., NOAA, Silver Spring, Md. (Available at <http://www.arl.noaa.gov/ready/hysplit4.html>).
- Dumka, U. C., K. Krishna Moorthy, Rajesh Kumar, P. Hegde, Ram Sagar, P. Pant, Narendra Singh, and S. Suresh Babu (2010), Characteristics of aerosol black carbon mass concentration over a high altitude location in the Central Himalayas from multi-year measurements, *Atmospheric Research*, Volume 96, Issue 4, June 2010, pp 510-521.
- Ekhart, E., (1948), De la structure thermique de l'atmosphère dans la montagne [On the thermal structure of the mountain atmosphere]. *La Meteorologie* 4, 3–26. [English translation: Whiteman, C.D., and Dreiseitl, E. (1984). *Alpine Meteorology: Translations of Classic Contributions by A.Wagner, E. Ekhart and F. Defant.*

- PNL-5141/ASCOT-84-3. Pacific Northwest Laboratory, Richland, Washington, 121 pp, Available online at: http://www.osti.gov/bridge/product.biblio.jsp?osti_id=6665518].
- Fernald F. G., B. Herman, and J. Regan (1972), Determination of aerosol height distributions by lidar. *J. Appl. Meteorol.*, (USA), 11, pp 482-489.
- Fernald, F. G., (1984), Analysis of Atmospheric Lidar Observations: Some Comments. *Applied Optics*, 23, 652-653.
- Foken, T., and B. Wichura (1996), Tools for Quality Assessment of Surface-Based Flux Measurements. *Agric. For. Meteorol.*, 78, 83-105.
- Friehe, C. A., (1987), Review of atmospheric boundary layer research, 1983–1986. *Rev. Geophys.*, 25(3), 387–392, doi:10.1029/RG025i003p00387.
- Gadhavi, H., and A. Jayaraman (2006), Airborne lidar study of the vertical distribution of aerosols over Hyderabad, an urban site in central India, and its implication for radiative forcing calculations. *Ann. Geophys. (Germany)*, 24, pp 2461-2470.
- Gage, K. S., (1990), Radar observations of the free atmosphere: Structure and dynamics. *Radar in Meteorology*, edited by Atlas, D. Amer. Meteor. Soc., Boston, pp. 534–565.
- Garratt, J. R., (1993), Sensitivity of climate simulations to land-surface and atmospheric boundary-layer treatments—A review. *J. Clim.*, 6(3), 419–448, doi: 10.1175/1520-0442(1993)006<0419:SOCSTL>2.0.CO;2.
- Garratt, J. R., and P. A. Taylor (1996), Boundary-Layer Meteorology 25th Anniversary Volume, 1970–1995: Invited Reviews and Selected Contributions to Recognise Ted Munn’s Contribution as Editor over the Past 25 Years, Springer Netherlands, 417 pp., doi: 10.1007/978-94-017-0944-6.
- Gautam, R., N. C. Hsu, M. Kafatos, and S. C. Tsay (2007), Influences of winter haze on fog/low cloud over the Indo-Gangetic plains. *J. Geophys. Res.*, 112, D05207, doi: 10.1029/2005JD007036.

- Geissbuhler, P., R. Siegwolf, and W. Eugster (2000), Eddy Covariance Measurements on Mountain Slopes: the Advantage of Surface-Normal Sensor Orientation over a Vertical Set-Up. *Bound. Layer Meteorol.*, 96: 371–392.
- Gossard, E. E., R. B. Chadwick, W. D. Neff, and K. P. Moran (1982), Use of Ground-Based Doppler Radars to Measure Gradients, Fluxes and Structure Parameters in Elevated Layers. *J. Appl. Meteor.*, 21, 211–226.
- Green, J. L., K. S. Gage, and T. E. VanZandt (1979), Atmospheric measurements by VHF pulsed Doppler radar. *IEEE Trans. Geosci. Electron.*, GE-17, 262–280.
- Guleria, R. P., J. C. Kuniyal, P. Singh Rawat, H. K. Thakur, M. Sharma, N. L. Sharma, M. Singh, K. Chand, P. Sharma, A. K. Thakur, P. P. Dhyani, and P. K. Bhuyan (2012), Aerosol optical properties in dynamic atmosphere in the northwestern part of the Indian Himalaya: A comparative study from ground and satellite based observations. *Atmos. Res.* 101, 726-738.
- Gustavsson, T., M. Karlsson, J. Bogren, and S. Sindqvist (1998), Development of temperature patterns during clear nights. *J. Appl. Meteor.*, 37: 559–571.
- He, Q. S., C. C. Li, J. T. Mao, A. K. H. Lau, and P. R. Li (2006), A study on the aerosol extinction-to-backscatter ratio with combination of micro-pulse LIDAR and MODIS over Hong Kong. *Atmos. Chem. Phys.*, 6, 3243–3256.
- Hegde, P., P. Pant, and Y. Bhavani Kumar (2009), An integrated analysis of lidar observations in association with optical properties of aerosol from a high altitude location in central Himalayas. *Atmos. Sci. Lett.*, 10: 48–57. doi: 10.1002/asl.209.
- Helgason, W., and J. W. Pomeroy (2012), Characteristics of the near-surface boundary layer within a mountain valley during winter. *J. Appl. Meteor. Climatol.*, 51: 583–597, doi:10.1175/JAMC-D-11-058.1.
- Henne, S., M. Furger, S. Nyeki, M. Steinbacher, B. Neininger, S. F. J. de Wekker, J. Dommen, N. Spichtinger, A. Stohl, and A. S. H. Prévôt (2004), Quantification of

topographic venting of boundary layer air to the free troposphere. *Atmos. Chem. Phys.*, 4, 497-509, doi:10.5194/acp-4-497-2004.

Hennemuth, B., and A. Lammert (2006), Determination of the atmospheric boundary layer height from radiosonde and lidar backscatter. *Bound. Layer Meteorol.*, 120, 181–200. doi: 10.1007/s10546-005-9035-3.

Hooper, W. P., and E. Eloranta (1986), Lidar measurements of wind in the planetary boundary layer: the method, accuracy and results from joint measurements with radiosonde and kytoon. *J. Clim. Appl. Meteor.*, 25, 990–1001.

Hughes, M., A. Hall, and R. G. Fovell (2007), Dynamical controls on the diurnal cycle of temperature in complex topography. *Clim. Dyn.*, 29(2–3): 277– 292, doi: 10.1007/s00382-007-0239-8.

IPCC, 2001: Climate Change (2001), The Science of Climate Change, Technical Summary of the Working Group I Report. *Cambridge Univ. Press*, New York.

IPCC, 2007: Climate change (2007), The physical science basis, Contribution of Working Group I to the Fourth Assessment Report of the Intergovernmental Panel on Climate Change, S. Solomon, D. Qin, M. Manning, Z. Chen, M. Marquis, K. B. Averyt, M. Tignor, and H. L. Miller: Eds (Cambridge University Press, Cambridge, UK), 996p.

IPCC, 2013: Summary for Policymakers. In: Climate Change (2013), The Physical Science Basis. Contribution of Working Group I to the Fifth Assessment Report of the Intergovernmental Panel on Climate Change [Stocker, T. F., D. Qin, G. K. Plattner, M. Tignor, S. K. Allen, J. Boschung, A. Nauels, Y. Xia, V. Bex, and P. M. Midgley (eds.)]. *Cambridge University Press*, Cambridge, United Kingdom and New York, NY, USA.

Janjic, Z. I., (1996), The surface layer in the NCEP Eta Model. Eleventh Conference on Numerical Weather Prediction, Norfolk, VA, 19–23 August. *Amer. Meteor. Soc.*, Boston, Boston, MA, p. 354–355.

- Janjic, Z. I., (2002), Nonsingular Implementation of the Mellor-Yamada Level 2.5 Scheme in the NCEP Meso model. *NCEP Office Note*, 437, 61 pp.
- Janssen, R. H. H., J. Vilà-Guerau de Arellano, J. L. Jimenez, L. N. Ganzeveld, N. H. Robinson, J. D. Allan, H. Coe, and T. A. M. Pugh (2013), Influence of boundary layer dynamics and isoprene chemistry on the organic aerosol budget in a tropical forest. *J. Geophys. Res. Atmos.*, 118, 9351-9366.
- Janssen, R. H. H., and A. Pozzer (2015), Description and implementation of a MiXed Layer model (MXL, v1.0) for the dynamics of the atmospheric boundary layer in the Modular Earth Submodel System (MESSy). *Geosci. Model Dev.*, 8, 453-471, doi: 10.5194/gmd-8-453-2015.
- Janssens-Maenhout, G., M. Crippa, D. Guizzardi, F. Dentener, M. Muntean, G. Pouliot, T. Keating, Q. Zhang, J. Kurokawa, R. Wankmüller, H. Denier van der Gon, J. J. P. Kuenen, Z. Klimont, G. Frost, S. Darras, B. Koffi, and M. Li (2015), HTAP_v2: a mosaic of regional and global emission grid maps for 2008 and 2010 to study hemispheric transport of air pollution. *Atmos. Chem. Phys.*, 15, 11411-11432, doi: 10.5194/acp-15-11411-2015.
- Jöckel, P., A. Kerckweg, A. Pozzer, R. Sander, H. Tost, H. Riede, A. Baumgaertner, S. Gromov, and B. Kern (2010), Development cycle 2 of the Modular Earth Submodel System (MESSy2). *Geosci. Model Dev.*, 3, 717-752.
- Kaimal, J. C., E. Gaynor, H. A. Zimmerman, and G. A. Zimmerman (1990), Minimizing flow distortion errors in a sonic anemometer. *Boundary-Layer Meteorol*, 53:103–115.
- Kaimal, J. C., and J. J. Finnigan (1994), Atmospheric boundary layer flows: Their structure and measurement. *Oxford University Press*, New York, 289 pp.
- Kalapureddy, M. C. R, K. Kishore Kumar, V. Sivakumar, A.K. Ghosh, A. R. Jain, and K. Krishna Reddy (2007), Diurnal and seasonal variability of TKE dissipation rate in

- the ABL over a tropical station using UHF wind profiler. *J. Atmos. Solar-Terr. Phys.*, 69: 419–430.
- Katul, G.G., C. I. Hsieh, and J. Sigmon (1997), Energy-Inertial Scale Interactions for Velocity and Temperature in the Unstable Atmospheric Surface Layer. *Boundary-Layer Meteorol.*, 82: 49–80.
- Katurji, M., A. Sturman, and P. Zawar- Reza (2011), An investigation into ridge-top turbulence characteristics during neutral and weakly stable conditions: velocity spectra and isotropy. *Boundary-Layer Meteorol.*, 139:143–160.
- Kaufman, Y. J., D. Tanre, H. R. Gordon, T. Nakajima, J. Lenoble, R. Frouin, H. Grassl, B. M. Hermann, M. D. King, and P. M. Teillet (1997), Passive remote sensing of tropospheric aerosol and atmospheric correction for the aerosol effect. *J. Geophys. Res.*, 102, 16,815–16,830, doi: 10.1029/97JD01496.
- Ketterer, C., P. Zieger, N. Bukowiecki, M. Collaud Coen, O. Maier, D. Ruffieux, and E. Weingartner (2014), Investigation of the planetary boundary layer in the Swiss Alps using remote sensing and in-situ measurements. *Bound.-Lay. Meteorol.*, 151, 317-334, doi:10.1007/s10546-013-9897-8.
- Kim, D., and V. Ramanathan (2008), Solar radiation budget and radiative forcing due to aerosols and clouds. *J. Geophys. Res.*, (USA), 113, D02203, doi: 10.1029/2007JD008434.
- Kim, S.-W., S. C. Yoon, J. Kim, and S. Y. Kim (2007), Seasonal and monthly variations of columnar aerosol optical properties over East Asia determined from multi-year MODIS, lidar and AERONET Sun/sky radiometer measurements. *Atmos. Environ.*, 41, 1634-1651.
- Kleissl, J., R. E. Honrath, M. P. Dziobak, D. Tanner, M. Val Martin, R. C. Owen, and D. Helmig (2007), Understanding of upslope flows at the Pico mountaintop observatory: A case study of orographic flows on a small, volcanic island. *J. Geophys. Res.*, 112: D10S35.

- Klett, J. D., (1985), Lidar inversion with variable backscatter/extinction ratios. *Applied Optics*, 24, 1638–1643.
- Komppula, M., T. Mielonen, A. Arola, K. Korhonen, H. Lihavainen, A.-P. Hyvarinen, H. Baars, R. Engelmann, D. Althausen, A. Ansmann, D. Müller, T. S. Panwar, R. K. Hooda, V. P. Sharma, V.-M. Kerminen, K.E.J. Lehtinen, and Y. Viisanen (2012), One year of Raman-lidar measurements in GualPahari EUCAARI site close to New Delhi in India: seasonal characteristics of the aerosol vertical structure. *Atmos. Chem. Phys.* 12, 4513–4524.
- Kossmann, M., R. Vöglin, U. Corsmeier, B. Vogel, F. Fiedler, H. J. Binder, N. Kalthoff, and F. Beyrich (1998), Aspects of the convective boundary layer structure over complex terrain. *Atmospheric Environment*, 32, 1323-1348, [http://dx.doi.org/10.1016/S1352-2310\(97\)00271-9](http://dx.doi.org/10.1016/S1352-2310(97)00271-9).
- Kossmann, M., U. Corsmeier, S. F. J. De Wekker, F. Fiedler, R. Vöglin, N. Kalthoff, H. Güsten, and B. Neininger (1999), Observations of handover processes between the atmospheric boundary layer and the free troposphere over mountainous terrain. *Contrib. Atmos. Phys.* 72, 329–350.
- Kotamarthi, V. R., (2010), Ganges Valley Aerosol Experiment: Science and Operations Plan. *DOE/SC-ARM-10-019*, available at <http://www.arm.gov/publications/programdocs/doe-sc-arm-10-019.pdf?id=25>.
- Kotamarthi, V. R., and S. K. Satheesh (2011), Ganges Valley Aerosol Experiment. Air & Waste Management Association, Em, *The magazine for environmental managers*.
- Kovalev, V., and W. Eichinger (2004), Elastic Lidar: Theory, Practice and Analysis Methods. *Wiley and Sons*, 615 pp.
- Krishnan, P., and P. K. Kunhikrishnan (2002), Some Characteristics of Atmospheric Surface Layer over a Tropical Inland Region during Southwest Monsoon Period. *Atmos. Res.*, 62: 111–124.

- Kumar, R., M. Naja, S. Venkataramani, and O. Wild (2010), Variations in surface ozone at Nainital, a high altitude site in the Central Himalayas. *J. Geophys. Res.*, 115, D16302, doi: 10.1029/2009JD013715.
- Kumar, R., M. Naja, G. G. Pfister, M. C. Barth, and G. P. Brasseur (2012), Simulations over South Asia using the Weather Research and Forecasting model with Chemistry (WRF-Chem): set-up and meteorological evaluation. *Geosci. Model Dev.*, 5, 321-343, doi: 10.5194/gmd-5-321-2012.
- Lang, M. N., A. Gohm, and J. S. Wagner (2015), The impact of embedded valleys on daytime pollution transport over a mountain range. *Atmos. Chem. Phys.*, 15, 11981-11998 doi:10.5194/acp-15-11981-2015.
- Lau, K. M., M. K. Kim, and K. M. Kim (2006), Asian summer monsoon anomalies induced by aerosol direct forcing: The role of the Tibetan Plateau. *Climate Dynamics (Germany)*, 26, pp 855-864.
- Leon, J.-F., Y. Derimian, I. Chiapello, D. Tanre, T. Podvin, B. Chatenet, A. Diallo, and C. Deroo (2009), Aerosol vertical distribution and optical properties over M'Bour (16.96°W; 14.39° N), Senegal from 2006 to 2008. *Atmos. Chem. Phys.*, 9, 9249–9261.
- Lewandowski, P. A., W. E. Eichinger¹, H. Holder, J. Prueger, J. Wang, and L. I. Kleinman (2010), Vertical distribution of aerosol in the vicinity of Mexico City during MILAGRO-2006 Campaign. *Atmos. Chem. Phys.*, 10, 1017–1030.
- Li, J. G., and B. W. Atkinson (1999), Transition regimes in valley airflows. *Boundary-Layer Meteorol.*, 91: 385-411.
- Liu, J., Y. Zheng, Z. Li, C. Flynn, and M. Cribb (2012), Seasonal variations of aerosol optical properties, vertical distribution and associated radiative effects in the Yangtze Delta region of China. *J. Geophys. Res.*, 117, D00K38, doi: 10.1029/2011JD016490.

- Liu, Z., R. Kuehn, M. Vaughan, D. Winker, A. Omar, K. Powell, C. Trepte, Y. Hu, and C. Hostetler (2010), The CALIPSO cloud and aerosol discrimination: Version 3 algorithm and test results. *Proceedings of the 25th International Laser Radar Conference, 5-9 July 2010, St. Petersburg, Russia*, 155-158.
- Mahrt, L., and R. Heald (1983), Nocturnal surface temperature distribution as remotely sensed from low-flying aircraft. *Agric. Meteor.*, 28: 99–107.
- Mahrt, L., D. Vickers, R. Nakamura, J. Sun, S. Burns, D. Lenschow, and M. Soler (2001), Shallow drainage and gully flows. *Boundary-Layer Meteorol.*, 101:243–260.
- Mahrt, V., (2006), Variation of surface air temperature in complex terrain. *J. Appl. Meteorol. Climatol.*, 45:1481-1493.
- Mamouri, R. E., V. Amiridis, A. Papayannis, E. Giannakaki, G. Tsaknakis, and D. S. Balis (2009), Validation of CALIPSO space-borne-derived aerosol vertical structures using a ground-based lidar in Athens, Greece. *Atmos. Meas. Tech. Discuss.*, 2, 561-587, doi:10.5194/amtd-2-561-2009.
- Manoharan, V. S., V. R. Kotamarthi, Y. Feng, and M. P. Cadeddu (2014), Increased absorption by coarse aerosol particles over the Gangetic–Himalayan region. *Atmos. Chem. Phys.*, 14, 1159-1165, doi: 10.5194/acp-14-1159-2014.
- Martins, C. A., O. L. L. Moraes, O. C. Acevedo, and G. A. Degrazia (2009), Turbulence intensity parameters over a very complex terrain. *Boundary-Layer Meteorol.*, 133: 35–45.
- Meenu, S., K. Rajeev, K. Parameswaran, and C. S. Raju (2007), Characteristics of Double ITCZ over the Tropical Indian Ocean. *J. Geophys. Res.*, 112: D11106, doi:10.1029/2006JD007950.
- Meenu, S., K. Rajeev, K. Parameswaran, and A. K. M. Nair (2010), Regional distribution of deep clouds and cloud top altitudes over the Indian subcontinent and the surrounding oceans. *J. Geophys. Res.*, 115: D05205, doi:10.1029/2009JD011802.

- Meybeck, M., P. Green, and C. J. Vörösmarty (2001), A new typology for mountains and other relief classes: an application to global continental water resources and population distribution. *Mt. Res. Dev.*, 21, 34–45. doi: 10.1659/0276-4741(2001)021[0034:antfma]2.0.co;2.
- Mishra, A. K., and T. Shibata (2012), Climatological aspects of seasonal variation of aerosol vertical distribution over central Indo-Gangetic belt (IGB) inferred by the space-borne lidar CALIOP. *Atmospheric Environment*, 46, 365-375, 2012.
- Misra, A., S. Tripathi, D. Kaul, and E. Welton (2012), Study of MPLNET derived aerosol climatology over Kanpur, India, and validation of CALIPSO Level 2 Version 3 Backscatter and Extinction products. *J. Atmos. Oceanic Technol.* doi:10.1175/JTECH-D-11-00162.1.
- Mlawer, E. J., S. J. Taubman, P. D. Brown, M. J. Iacono, and S. A. Clough (1997), Radiative transfer for inhomogeneous atmospheres: RRTM, a validated correlated-k model for the longwave. *J. Geophys. Res. Atmos.*, 102, 16 663–16 682, doi: 10.1029/97JD00237, <http://dx.doi.org/10.1029/97JD00237>.
- Moraes, O. L. L., O. C. Acevedo, G. A. Degrazia, D. Anfossi, R. da Silva, and V. Anabor (2005), Surface layer turbulence parameters over a complex terrain. *Atmos. Environ.*, 39: 3103-3112.
- Nadeau, D. F., E. R. Pardyjak, C. W. Higgins, H. Huwald, and M. B. Parlange (2013), Flow during the evening transition over steep alpine slopes. *Q. J. R. Meteorol. Soc.*, 139(672), 607–624.
- Niranjan, K., B. L. Madhavan, and V. Sreekanth (2007), Micro pulse lidar observation of high altitude aerosol layers at Visakhapatnam located on the east coast of India. *Geophys. Res. Lett.*, (USA), 34, L03815, doi: 10.1029/2006GL028199.
- Nyeki, S., K. Eleftheriadis, U. Baltensperger, I. Colbeck, M. Fiebig, A. Fix, et al., (2002), Airborne lidar and in-situ aerosol observations of an elevated layer, leeward of the

- European Alps and Apennines. *Geophys. Res. Lett.*, 29, 1852, doi: 10.1029/2002GL014897
- Ojha, N., M. Naja, K. P. Singh, T. Sarangi, R. Kumar, S. Lal, M. G. Lawrence, T. M. Butler, and H. C. Chandola (2012), Variabilities in ozone at a semi-urban site in the Indo-Gangetic Plain region: Association with the meteorology and regional processes. *J. Geophys. Res.*, 117, D20301, doi: 10.1029/2012JD017716.
- Ojha, N., M. Naja, T. Sarangi, R. Kumar, P. Bhardwaj, S. Lal, S. Venkataramani, R. Sagar, A. Kumar, and H. C. Chandola (2014), On the Processes Influencing the Vertical distribution of ozone over the central Himalayas: Analysis of Yearlong ozonesonde observations. *Atmos. Environ.*, Volume 88, May 2014, Pages 201–211, doi: 10.1016/j.atmosenv.2014.01.031.
- Ojha, N., A. Pozzer, A. Rauthe-Schöch, A. K. Baker, J. Yoon, C. A. M. Brenninkmeijer, and J. Lelieveld (2016), Ozone and carbon monoxide over India during the summer monsoon: regional emissions and transport. *Atmos. Chem. Phys.*, 16, 3013 – 3032, doi: 10.5194/acp-16-3013-2016.
- Ottersten, H., (1969), Atmospheric Structure and Radar Backscattering in Clear Air'. *Radio Sci.*, 4, 1179-1193.
- Pahlow, M., M. B. Parlange, and F. Porté-Agel (2001), On Monin–Obukhov Similarity in the Stable Atmospheric Boundary Layer. *Boundary-Layer Meteorol.*, 99: 225–248.
- Panday, A. K., and R. G. Prinn (2009), Diurnal cycle of air pollution in the Kathmandu Valley, Nepal: Observations. *J. Geophys. Res.*, 114: D09305, doi: 10.1029/2008JD009777.
- Panofsky, H. A., and J. A. Dutton (1984), Atmospheric Turbulence. *Wiley*, New York, 397pp.
- Pant, P., P. Hegde, U. C. Dumka, A. Saha, M. K. Srivastava, and R. Sagar (2006), Aerosol characteristics at a high latitude location during ISRO-GBP land campaign-II.

Curr. Sci. 91: 1053-1061.

Papadopoulos, K. H., and C. G. Helmis (1999), Evening and morning transition of katabatic flows. *Boundary-Layer Meteorol.*, 92: 195-227.

Pappalardo, G., et al. (2010), EARLINET correlative measurements for CALIPSO: First intercomparison results. *J. Geophys. Res.*, 115, D00H19, doi:10.1029/2009JD012147.

Pelon, J., M. Mallet, A. Mariscal, P. Goloub, D. Tanré, D. BouKaram, C. Flamant, J. Haywood, B. Pospichal, and S. Victori (2008), Microlidar observations of biomass burning aerosol over Djougou (Benin) during African Monsoon Multidisciplinary Analysis Special Observation Period 0: Dust and Biomass-Burning Experiment. *J. Geophys. Res.*, 113, D00C18, doi:10.1029/2008JD009976.

Raghavan, S., (2003), Radar Meteorology. *Atmospheric and oceanic Science Library*, Kluwer Academic Publishers.

Reddy, K. K., T. Kozu, Y. Ohno, K. Nakamura, A. Higuchi, K. Madhu Chandra Reddy, V. K. Anandan, P. Srinivasulu, A. R. Jain, P. B. Rao, R. Ranga Rao, G. Viswanathan, and D. Narayana Rao (2002), Planetary boundary layer and precipitation studies using lower atmospheric wind profiler over tropical India. *Radio Sci.*, 37(4), 14-1 to 14-21, doi: 10.1029/2000RS002538.

Reddy, K. K., T. Kozu, and D. N. Rao (2006), Wind profiler radar for understanding the tropical convective boundary layer during different seasons. *Indian Journal of Radio and Space Physics*, Vol. 35, 105-115.

Reddy, K. K., M. Naja, N. Ojha, P. Mahesh, and S. Lal (2012), Influences of the boundary layer evolution on surface ozone variations at a tropical rural site in India. *J. Earth Syst. Sci.*, 121 (4), 911–922.

- Ramana, M. V., V. Ramanathan, I. A. Podgorny, B. B. Pradhan, and B. Shrestha (2004), The direct observation of large aerosol radiative forcing in the Himalayan region. *Geophys. Res. Lett.*, 31, L05111, doi:10.1029/2003GL018824.
- Ramanathan, V., P. J. Crutzen, J. Lelieveld, et al. (2001b), Indian Ocean experiment: An integrated analysis of the climate forcing and effects of the great Indo-Asian haze. *J. Geophys. Res.*, 106(D22), 28371–28398.
- Ramanathan, V., and M. V. Ramana (2005), Persistent, widespread, and strongly absorbing haze over the Himalayan foothills and the Indo-Gangetic plains. *Pure Appl. Geophys.*, 162: 1609–1626.
- Richiardone, R., E. Giampiccolo, S. Ferrarese, and M. Manfrin (2008), Detection of flow distortions and systematic errors in sonic anemometry using the planar fit method. *Boundary-Layer Meteorol.*, 128: 277–302.
- Rotach, M. W., and D. Zardi (2007), On the boundary-layer structure over highly complex terrain: key findings from MAP. *Q. J. R. Meteorol. Soc.*, 133: 937–948, doi: 10.1002/qj.71.
- Rotach, M. W., A. Gohm, M. N. Lang, D. Leukauf, I. Stiperski, and J. S. Wagner (2015), On the vertical exchange of heat, mass and momentum over complex, mountainous terrain. *Front. Earth Sci.*, 3:76. doi: 10.3389/feart.2015.00076.
- Royer, P., J. C. Raut, G. Ajello, S. Berthier, and P. Chazette (2010), Synergy between CALIOP and MODIS Instruments for Aerosol Monitoring: Application to the Po Valley. *Atmospheric Measurement Techniques*, 3: 893–907.
- Sagar, R., B. Kumar, U. C. Dumka, K. K. Moorthy, and P. Pant (2004), Characteristics of aerosol spectral optical depths over Manora Peak: A high-altitude station in the central Himalayas. *J. Geophys. Res.*, 109, D06207, doi: 10.1029/2003JD003954.
- Sagar, R., U. C. Dumka, Manish Naja, Narendra Singh, and D. V. Phanikumar (2015), ARIES, Nainital: a strategically important location for climate change studies in

- the Central Gangetic Himalayan region. *Current science*, Vol.. 109, No. 4, 25 August 2015, pp 703-715.
- Sarangi, T., M. Naja, N. Ojha, R. Kumar, S. Lal, S. Venkataramani, A. Kumar, R. Sagar, and H. C. Chandola (2014), First simultaneous measurements of ozone, CO and NO_y at a high altitude regional representative site in the central Himalayas. *J. Geophys. Res.*, 119, doi: 10.1002/2013JD020631.
- Simpson, M., S. Raman, J. K. Lundquist, and M. Leach (2007) A study of the variation of urban mixed layer heights. *Atmos. Environ.*, 41, 6923-6930.
- Singh, N., R. R. Joshi, H. Y. Chun, G. B. Pant, S. H. Damle, and R. D. Vashishtha (2008), Seasonal, annual and inter-annual features of turbulence parameters over the tropical station Pune (18° 32' N, 73° 51' E) observed with UHF wind profiler. *Ann. Geophys.*, 26, 3677–3692.
- Singh, N., R. Solanki, N. Ojha, R. H. H. Janssen, A. Pozzer, and S. K. Dhaka (2016), Boundary layer evolution over the central Himalayas from radio wind profiler and model simulations. *Atmos. Chem. Phys.*, 16, 10559-10572, doi:10.5194/acp-16-10559-2016.
- Sinha, P. R., R. K. Manchanda, D. G. Kaskaoutis, Y. B. Kumar, and S. Sreenivasan (2013), Seasonal variation of surface and vertical profile of aerosol properties over a tropical urban station Hyderabad, India. *J. Geophys. Res. – Atmos.*, 118, 749–768, doi: 10.1029/2012JD018039.
- Solanki Raman, Narendra Singh, P. Pant, U. C. Dumka, Y. Bhavani Kumar, A. K. Srivastava, Sanjay Bist, and H. C. Chandola (2013), Detection of long range transport of aerosols with elevated layers over high altitude station in the central Himalayas: A case study on 22 and 24 March 2012 at ARIES, Nainital. *Indian Journal of Radio & Space Physics*, Vol. 42, Oct 2013, pp 332-339.

- Solanki, R., and N. Singh (2014), LiDAR observations of the vertical distribution of aerosols in free troposphere: Comparison with CALIPSO level-2 data over the central Himalayas. *Atmos. Environ.*, 99: 227–238.
- Solanki, R., N. Singh, N. V. P. Kiran Kumar, K. Rajeev, and S. K. Dhaka (2016), Time variability of surface-layer characteristics over a mountain ridge in the central Himalayas during the spring season. *Boundary-Layer Meteorol.*, Volume 158, Issue 3, pp 453-471, doi: 10.1007/s10546-015-0098-5.
- Srivastava, A. K., S. Singh, S. Tiwari, V. P. Kanawade, and D. S. Bisht (2012b), Variation between near-surface and columnar aerosol characteristics during winters and summers at a station in the Indo-Gangatic Basin. *Journal of Atmospheric and Solar-Terrestrial Physics*, 77, 57–66. doi:10.1016/j.jastp.2011.11.009.
- Srivastava, A. K., P. Pant, P. Hegde, S. Singh, U. C. Dumka, M. Naja, N. Singh, and Y. Bhavani kumar (2011a), Influence of south Asian dust storm on aerosol radiative forcing at a high-altitude station in central Himalayas. *International Journal of Remote Sensing*, 32 (22), 7827–7845.
- Srivastava S. K., M. K. Srivastava, A. Saha, S. Tiwari, S. Singh, U. C. Dumka, B. P. Singh, and N. P. Singh (2011), Aerosol optical properties over Delhi and Manora peak during a rare dust event in early April 2005. *International Journal of Remote Sensing*, 32 (23), 7939–7954.
- Stewart, J. Q., C. D. Whiteman, W. J. Steenburgh, and X. Bian (2002), A climatological study of thermally driven wind systems of the U.S. intermountain West. *Bull. Amer. Meteor. Soc.*, 83: 699–708.
- Stull, R. B., (1988), An Introduction to Boundary Layer Meteorology. *Kluwer Academic Publishers*, Dordrecht, The Netherlands, 670 pp.
- Sun, F., Y. Ma, M. Li, W. Ma, H. Tian, and S. Metzger (2007), Boundary layer effects above a Himalayan valley near Mount Everest. *Geophys. Res. Lett.*, 34: L08808,

doi:10.1029/2007GL029484.

- Sunilkumar, S. V., K. Parameswaran, and B. V. Krishna Murthy (2003), Lidar observations of cirrus cloud near the tropical tropopause: General features. *Atmos. Res. (Netherlands)*, 66, pp 203-227.
- Taraborrelli, D., M. G. Lawrence, T. M. Butler, R. Sander, and J. Lelieveld (2009), Mainz Isoprene Mechanism 2 (MIM2): an isoprene oxidation mechanism for regional and global atmospheric modelling. *Atmos. Chem. Phys.*, 9, 2751-2777.
- Tatarskii, V. I., (1971), The Effects of the Turbulent Atmosphere on Wave Propagation. Translated from Russian, Isr. Program for Sci. Transl., Jerusalem, 472 pp. (Available as TT-68-50464/XAB, Natl. Tech. Inf. Serv., Springfield, Va.).
- Taylor, G. I., (1938), The Spectrum of Turbulence. *Proc. Roy. Soc.*, London, A164, 476–490.
- Tesche, M., U. Wandinger, A. Ansmann, D. Althausen, D. Müller, and A. H. Omar (2013), Ground-based validation of CALIPSO observations of dust and smoke in the Cape Verde region. *J. Geophys. Res. – Atmos.*, 118, 2889–2902, doi: 10.1002/jgrd.50248.
- Thompson, G., P. R. Field, R. M. Rasmussen, and W. D. Hall (2008), Explicit forecasts of winter precipitation using an improved bulk microphysics scheme. part ii: implementation of a new snow parameterization. *Mon. Wea. Rev.*, 136, 5095–5115, doi:10.1175/2008MWR2387.1, <http://journals.ametsoc.org/doi/abs/10.1175/2008MWR2387.1>.
- Tiwari, P. C., and B. Joshi (1997), Wildlife in the Himalayan Foothills: Conservation and Management. *Indus Publishing Company*, New Delhi.
- Trini Castelli, S., S. Falabino, L. Mortarini, E. Ferrero, R. Richiardone, and D. Anfossi (2014), Experimental investigation of the surface layer parameters in low wind conditions in a suburban area. *Q. J. R. Meteorol. Soc.*, 140, 2023–2036.

- Twomey, S., (1977), The Influence of pollution on the short-wave albedo of clouds. *Journal of the atmospheric sciences*, 34, 1149–1152.
- Vickers, D., and L. Mahrt (2006b), A solution for flux contamination by mesoscale motions with very weak turbulence. *Boundary-Layer Meteorol.*, 118: 431–447.
- Vilà-Guerau de Arellano, J., C. van Heerwaarden, B. van Stratum, and K. van den Dries (2015) Atmospheric boundary layer: Integrating chemistry and land interactions. *Cambridge University Press*.
- Wakimoto, R. M., and J. L. Mc Elroy (1986), Lidar observations of elevated pollution layers over Los Angeles. *J. Clim. Appl. Meteorol.* 25, 1583–1599.
- Wallace, J. M., and P. V. Hobbs (1977), Atmospheric Science, An Introductory Survey, *Academic Press*, New York, 467 pp.
- White, A. B., C. W. Fairall, and D. W. Thompson (1991a), Radar Observations of Humidity Variability In and Above the Marine Atmospheric Boundary Layer. *J. Atmos. Ocean. Technol.*, 8, 639-558.
- White, A. B., C. W. Fairall, and D. E. Wolfe (1991b), Use of 915 MHz Wind Profiler Data to Describe Diurnal Variability of the Mixed Layer. In Preprints, 7th Joint Conference on Applications of Air Pollution Meteorology with AWMA, New Orleans, Jan. 14-18, 1991, *Amer. Meteorol. Soc.*, pp. J161-J166.
- Whiteman, C. D., (1990), Observations of thermally developed wind systems in mountainous terrain. In: W. Blumen (Editor), Atmospheric Processes over Complex Terrain. Meteorological Monographs, 23(45), *American Meteorological Society*, Boston, USA, Chapter 2, pp. 5-42.
- Whiteman, C. D., (2000), Mountain meteorology fundamentals and applications. *Oxford University Press*, New York, 355pp.
- Wilczak, J. M., S. P. Oncley, and S. A. Stage (2001), Sonic anemometer tilt correction algorithms. *Boundary-Layer Meteorol.*, 99: 127-150.

- Winker, David M., Mark A. Vaughan, Ali Omar, Yongxiang Hu, Kathleen A. Powell, Zhaoyan Liu, William H. Hunt, and Stuart A. Young (2009), Overview of the CALIPSO Mission and CALIOP Data Processing Algorithms. *Journal of Atmospheric and Oceanic Technology*, 26, 2310–2323.
- Wyngaard, J. C., O. R. Cote', and Y. Izumi (1971), Local free convection, similarity, and the budgets of shear stress and heat flux. *Journal of Atmospheric Science*, 28: 1171–1182.
- Xie, B., J. C. H. Fung, A. Chan, and A. Lau (2012), Evaluation of nonlocal and local planetary boundary layer schemes in the WRF model. *J. Geophys. Res.*, 117, D12103, doi: 10.1029/2011JD017080.
- Xie, F., D. L. Wu, C. O. Ao, A. J. Mannucci, and E. R. Kursinski (2012), Advances and limitations of atmospheric boundary layer observations with GPS occultation over southeast Pacific Ocean. *Atmos. Chem. Phys.*, 12, 903–918, doi: 10.5194/acp-12-903-2012.
- Ye, D. Z., and G. X. Wu (1998), The role of the heat source of the Tibetan Plateau in the general circulation. *Meteorol. Atmos. Phys.*, 67, 181–198.
- Yuan, R., M. Kang, S. Park, J. Hong, D. Lee, and J. Kim (2007), The effect of coordinate rotation on the eddy covariance flux estimation in a hilly Koflux forest site. *Korean. J. Agric. For. Meteorol.*, 9:100–108.
- Yuan R, M. Kang, S. B. Park, J. Hong, D. Lee, and J. Kim (2011), Expansion of the planar-fit method to estimate flux over complex terrain. *Meteorol. Atmos. Phys.*, 110: 123–133, doi: 10.1007/s00703-010-0113-9.
- Yusup, Y. B., W. R. Wan Daud, A. B. Zaharim, and M. Z. Meor Talib (2008), Structure of the atmospheric surface layer over an industrialized equatorial area. *Atmos. Res.*, 90: 70–77.

Zhong, S., and C. D. Whiteman (2008), Downslope flows on a low-angle slope and their interactions with valley inversions. II. Numerical modeling. *J. Appl. Meteor. Climatol.*, 47, 2039-2057.

Blank page